HELSINGIN YLIOPISTO
HELSINGFORS UNIVERSITET
UNIVERSITY OF HELSINKI

Master`s thesis
Geosciences & Geography
Solid Earth Geophysics

SEISMIC AMPLITUDE VS. OFFSET AND ATTRIBUTE ANALYSES FOR MINE PLANNING AT THE HANNUKAINEN FE-CU-AU MINE SITE

Keith Galvin

05.11.2020

Supervisors:

Emilia Koivisto (University of Helsinki)
Jouko Pakarinen (Hannukainen Mining Oy)

HELSINGIN YLIOPISTO
MATEMAATTIS-LUONNONTIETEELLINEN TIEDEKUNTA

PL 64 (Gustaf Hällströmin katu 2)
00014 Helsingin yliopisto

Tiedekunta/Osasto Fakultet/Sektion – Faculty Science	Laitos/Institution– Department Geosciences & Geography	
Tekijä/Författare – Author Keith Galvin		
Työn nimi / Arbetets titel – Title Seismic amplitude vs. offset and attribute analyses for mine planning at the Hannukainen Fe-Cu-Au mine site		
Oppiaine /Läroämne – Subject Solid Earth Geophysics		
Työn laji/Arbetets art – Level Master's	Aika/Datum – Month and year	Sivumäärä/ Sidoantal – Number of pages

Tiivistelmä/Referat – Abstract

A seismic reflection survey was carried out at the Hannukainen-Rautuvaara Iron (Fe), Copper (Cu), and Gold (Au) deposits as part of the HIRE (High Resolution Reflection Seismics for Ore Exploration, 2007-2010) project. The main discovery from this survey was a regional structure showing three reflective layers dipping to the southwest. The top of this package of reflectors is currently planned to be mined at Hannukainen. The deeper parts of this package may have potential continuation of the economically viable deposits seen at shallow depths.

In this work, a target-specific, amplitude-preserving workflow for profiles E1 and V5 of the Hannukainen-Rautuvaara HIRE seismic data will be formulated and applied. Then seismic amplitude vs. offset (AVO) and attribute analyses will be used to analyse the reflective layers and identify potential areas of interest for further study. This is a burgeoning area of seismic research, AVO analysis is typically used in hydrocarbon exploration and has only been sparsely used in hard rock settings for mineral exploration. Attribute analysis is more common in hard rock environments, but still underutilised. The seismic reflection data were re-processed focusing on retaining the high-frequency content of the seismic signal, this is key for further analysis.

The results of the AVO analysis consist of determining the AVO class of the responses seen across the CMPs of two selected AVO horizons. AVO product and Poisson's ratio change across the horizons were calculated, and an area of interest was identified from the correlation of these parameters. Attribute analysis was done using the seismic attributes envelope, first derivative envelope, Hilbert Transform, relative impedance, phase, weighted instantaneous frequency and dip. The amplitude attributes (envelope, first derivative envelope, Hilbert Transform, relative impedance) were useful in determining the areas of the reflector package that showed the strongest amplitudes and selecting horizons on the uppermost reflector for AVO analysis. Phase and weighted instantaneous frequency helped determine the continuity of the reflector package which revealed a clear four-layer signature, differing form the earlier three-layer interpretation. The dip attribute showed vertical anomalies, some of which correlated with mapped faulting in the area. Detailed interpretation of the geophysical results requires better borehole coverage, and petrophysical work, to tie in the seismic data results to the alteration and mineralisation. With open pit mine planning ongoing in the study area, the identification of deep-seated mineral deposits will have direct impact on the planning of the mine and the future of exploration in Hannukainen-Rautuvaara.

Avainsanat – Nyckelord – Keywords
Seismic reflection, Amplitude vs. offset, Seismic attribute, Mineral exploration, Mine planning, Hannukainen Mine

Säilytyspaikka – Förvaringställe – Where deposited
HELDA - Digital repository for University of Helsinki

Muita tietoja – Övriga uppgifter – Additional information
6 tables and 43 figures

Table of Contents

1 Introduction

The interpretation of seismic reflection data utilising seismic amplitude vs. offset (AVO) and attribute analyses is widely used within the hydrocarbon industry (Ecker et al., 1998; Fatti et al., 1994; Rutherford & Williams, 1989), but still is not fully established in onshore mineral exploration. The use of seismic methods in hard rock environments is much more challenging than in marine sedimentary basins. This is due to more complex structures and the inherently poor signal-to-noise ratio. These complications in the data acquisition phase make the data processing more laborious. The goal of this study is to utilise AVO and attribute analyses to resolve the detailed seismic signature of the Hannukainen-Rautuvaara Iron (Fe), Copper (Cu) and Gold (Au) deposits and associated alteration. The works also involves the construction of a target-specific, amplitude-preserving processing workflow for the seismic reflection data from the study site in order to prepare the data for the analyses. The analyses are largely dependent on maintaining the integrity of the data by preserving its amplitude, frequency and phase content. Preserving relative amplitudes is vital, but challenging, in hard rock seismic reflection studies due to the low signal-to-noise ratio. If not properly handled the degradation of amplitude content may cause misleading interpretations (Eaton & Wu, 1996).

The Hannukainen mine is located approximately 100 km south west of Levi, in the Kolari Region of Northern Finland. There is a long history of mining in the area going back as far as the late 17th century when the Juvakaisenmaa iron deposit provided ore for the Köngäs ironworks in Pajala. The Rautuvaara iron deposit was developed by Rautaruukki Oyj who commenced open pit mining in Rautuvaara in 1975, and in Hannukainen in 1978, continuing until 1988. The Fe-Cu-Au deposit at Laurinoja in the Hannukainen area was operated by Outokumpu Oy from 1989 to 1990. In 2005, Northland Mines Oy became active in this area and operated until bankruptcy in 2014. Hannukainen Mining Oy, a subsidiary of Tapojärvi Oy, took over operations in 2015. Hannukainen Mining Oy is currently in the permitting stage of mine development for the area. The area is a challenging environment for mining due to many nature and cultural factors, such as a sea trout river, reindeer herding, a ski resort and tourist centre, and the village of Hannukainen itself and vacation homes being in the surrounding region. The construction of the mine is planned to happen between 2021 and 2023 at a cost of €200 to 300 million. Mining is planned to start operations in 2023, with a goal of mining 6.5 million tons of ore per year. Open pit mining at Hannukainen will commence first, and later

two kilometres to the north at Kuervitikko. With maximum annual production capacity, the working life of the mine is estimated at 20 years, possibly extended if new reserves are discovered.

Initial analysis and interpretation of the Hannukainen-Rautuvaara reflection seismic survey data has been reported by Kukkonen et al. (2009), who interpreted the study area as being characterised by an upper 5 km of strong, high-amplitude reflectors that can be correlated to a lateral extent of up to 20 km. A three-layer system ranging from 200 m to about 1 km in thickness. This large-scale structure is interpreted as thrusting from southwest to northeast, related to the Kolari Shear Zone and folding. The uppermost reflectors of the three-layer package imaged in the Hannukainen area were correlated with known deposits and interpreted to result from the presence of iron stone, skarn and amphibolite within the monzonite, diorite and metasediments. In Rautuvaara, reflectors are correlated with amphibolite and skarn layers, with structures dipping steeper than seen in Hannukainen. More reflectors exist beneath the known deposits in the study area, giving some indication of possible deeper mineralisations.

In the oil industry seismic methods have long been used to delineate hydrocarbon containing sedimentary layers (Michum Jr., 1977; Shipley et al., 1979; Tucholke et al., 1977). In recent years, the mining industry has begun to see seismic reflection methods as a viable and economic option for exploration, in part due to the trend of deeper targets being explored. Other reasons to use seismic reflection methods are the high resolution and quality of images attainable, as well as greater penetration depth in comparison to potential field and electromagnetic methods. Malehmir et al. (2012a) give a comprehensive synopsis on the use of seismic reflection data in mineral exploration, pointing out that the amount of studies in this research area number only in the tens in Canada (Malehmir & Bellefleur, 2009; White et al., 2000; Milkereit et al., 1997), Europe (Juhlin et al., 2002; Korja & Heikkinen, 2005; Malehmir et al., 2009, 2012b), Australia (Drummond et al., 2000; Goleby et al., 2004; Urosevic et al., 2012), and South Africa (Trickett, 2005; Manzi et al., 2012a). Since the review by Malehmir et al. (2012a), quite a lot of seismic work has been completed (Bellefleur et al., 2015; Hloušek et al., 2015; Koivisto et al., 2015). However, the technique is still not widely published on in the mineral industry. One of the reasons for this is that it is often used for unpublished research and development. Additionally, Malehmir et al. (2012a) make the point that the cost of the seismic reflection method is a major hindrance to its use in mineral exploration and that costs will need to come down in the future for it to be fully considered viable for such use. On average a 2D seismic reflection study costs

in the region of €10,000 per kilometre. 1 km of borehole costs approximately €100,000 so this hindrance may be overstated, and the lack of knowledge should be considered the main sticking point.

The effect of offset on seismic wave amplitude has been long known when it comes to pore fluids (Domenico, 1976; Geertsma & Smit, 1961; Gregory, 1976). Thus, the potential for AVO analysis to determine oil and gas layers within sedimentary formations is well established. The basic operation of the analysis is to compare amplitudes from the same reflection point at different source-receiver offsets. One such example of the use of AVO analysis for hydrocarbon exploration is described in Li et al. (2003), who applied AVO analysis to carbonate reservoirs in the Western Canada Carbonate Sedimentary Basin. This study shows how AVO analysis can be used to reduce the risk involved in carbonate reservoir exploration. Furthermore, Foster et al. (2010) looked at the interpretation of AVO anomalies and found that the AVO response differentiable between hydrocarbon-bearing sands and brine sands and shales, with the extent of the hydrocarbon content also being determined from the AVO data.

Specific studies using AVO analysis in hard rock environments have not been widely published on. This leaves a gap in knowledge as to how effective AVO analysis can be on a global scale and for different deposit types. In one such study, Harrison & Urosevic (2012) used AVO analysis to target gold deposits in the St. Ives gold camp of Western Australia. They found that seismic reflection surveys in combination with rigorous processing steps and heavy quality control can be used to not only detect first-order structures, but also for more refined lithological analyses. The anomalies identified in the AVO analysis were thought to be caused by Poisson's ratio changes within a shear zone with respect to the rock due to differences in mineral composition but could also be from structural variations such as fracturing and alterations. Long offset seismic reflection data (~1km) was found to be beneficial in the analyses of rock type for hard rock environments.

The ability to extract as much information as possible out of seismic data is important from a cost-benefit perspective is seismic surveying. Seismic attributes can be gained from both 2D and 3D data. The advantage of 3D is that you can create an attribute volume in 3D space and take slices at certain intervals. Compared to AVO analysis, attribute analyses have been better adapted to hard rock environments. In Manzi et al. (2012a, 2012b, 2013), the author utilises a wide range of seismic attributes to help identify mining targets and improve their geological

and stratigraphic interpretation. Stuart et al. (2000) had real success in enhancing veins of gold alteration by using various attributes such as instantaneous frequency, instantaneous phase, paraphase, seismic envelope, reflection strength, and average energy. A real advantage of seismic attributes is the vast amount of attributes available, these can be calculated for a elected seismic section relatively easily and the most interesting signal gained can then be chosen.

1.1 Thesis aims

In this work, the aim is to test the applicability seismic reflection data for mineral exploration by further analysing the Hannukainen-Rautuvaara HIRE project dataset. The goal is to produce a target-specific, amplitude-preserving processing workflow that allows to analyse the detailed seismic signature of the mineral deposit. Seismic analysis techniques not normally used for mineral exploration will be tested, namely AVO and attribute analyses. No such study has been completed on the Hannukainen-type deposits, and generally with Finland's wealth of mineral deposits and mining operations these unconventional analysis methods could hold great value. With these techniques it is hoped that a well resolved seismic signature can be identified in the results. Another element of this study is the re-processing of older 'legacy' data, a cost-effective approach to gain new information on a target. It is of great benefit to a prospective mining operation to exhaust available data using newer processing techniques as they become proven and available. This can offset the cost of planning new surveys and increase the value of existing data.

2 Geological Background

The study area is located within the Central Lapland Greenstone Belt (CLGB) in Northern Finland (Figure 1), which was formed by a succession of rifting events of the Archean craton. Multiple thrust, shear and fault zones are the main structural features in the study area, these form the Kolari Shear Zone (KSZ) that is seen in the inset of Figure 1 as a red dashed line that runs down Western Finland and into Sweden, and the Äkäsjoki Shear Zone (ÄSZ). The ÄSZ is a major NE-SW running fault that is located south of the Hannukainen area (Figure 1).

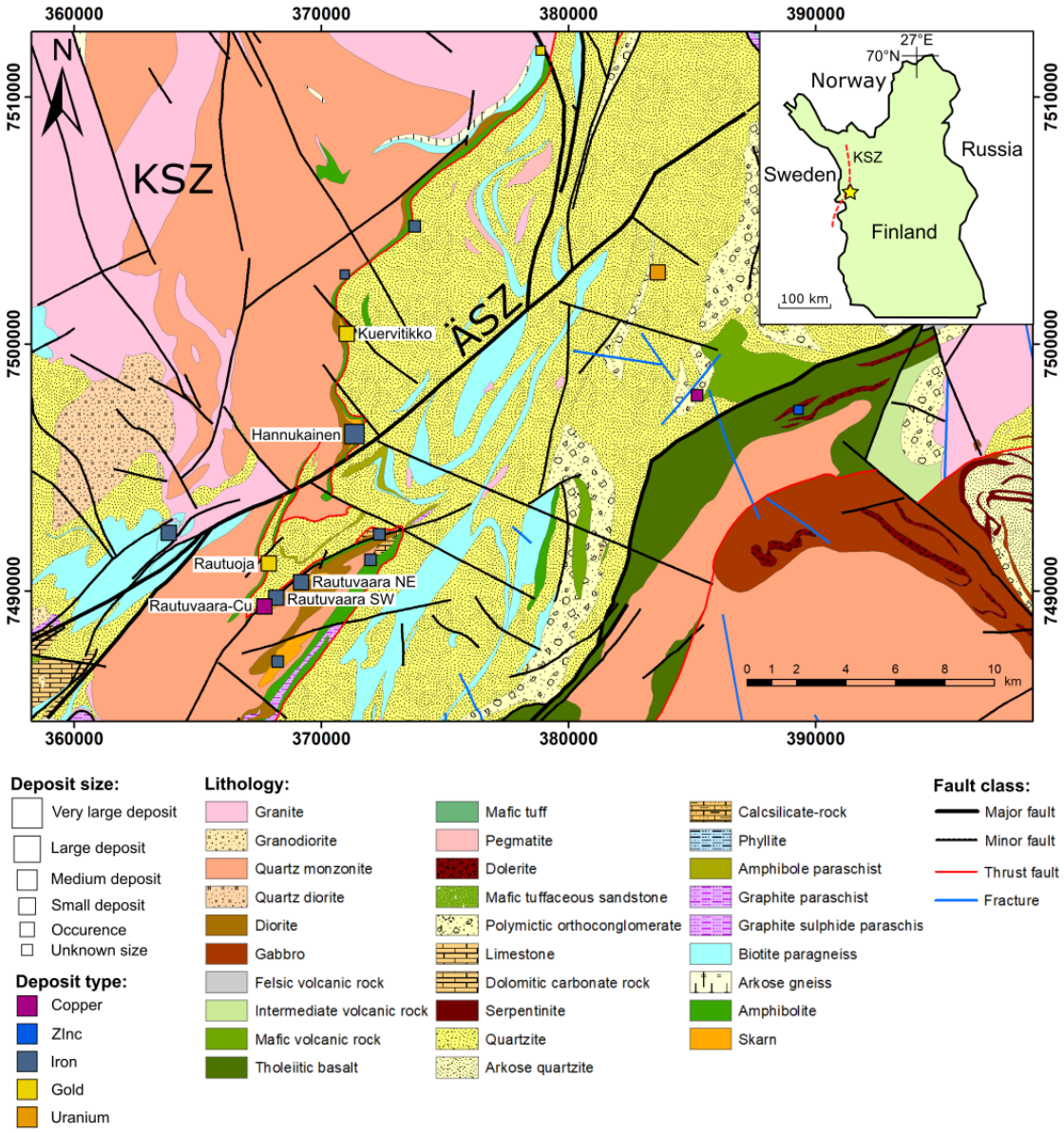

Figure 1 - Geological map of the survey area, with geological units, faults, and deposits. The survey area is marked as a yellow star in the insert. Coordinates are in the EUREF-FIN ETRS-TM35FIN system. Lithology and structure data: Bedrock of Finland 1:200 000 © Geological Survey of Finland 2016.

The sedimentary and volcanic evolution of the CLGB has spanned hundreds of millions of years across an area spanning from the Salla-Kuusamo area at the eastern border of Finland over Central Finland to the Finnish-Norwegian border (Hanski et al., 2001). Radiometric age estimates of the lower parts of the supracrustal sequences deposited on the Archean basement vary, the oldest being from Kröner et al. (1981), who dated zircon fractions from the Tojottamanselkä Basement Dome near Rookkijärvi at 3.1 Ga. The youngest age estimate is from Meriläinen (1976) dated at 2.6 Ga. The Archean basement is overlain by a Paleoproterozoic supracrustal sequence, aged at 2.45 Ga to less than 1.88 Ga, ending with the

intrusion of post-orogenic granites circa 1.8 Ga. The supracrustal rocks seen in the Kolari region consist of four of the seven lithostratigraphic groups (Figure 2) seen in the CLGB; the Onkamo Group (tholeiites and komatiites), Sodankylä Group (quartzites, mica schists and gneisses, and conglomerates), Savukoski Group (Fe–tholeiites, tuffites, dolomitic marbles and black schists), and Lainio Group (quartzites, siltstones, conglomerates and minor volcanic rocks) (Hiltunen, 1982). The dominant intrusives in the area are diorites, tonalites and monzonites.

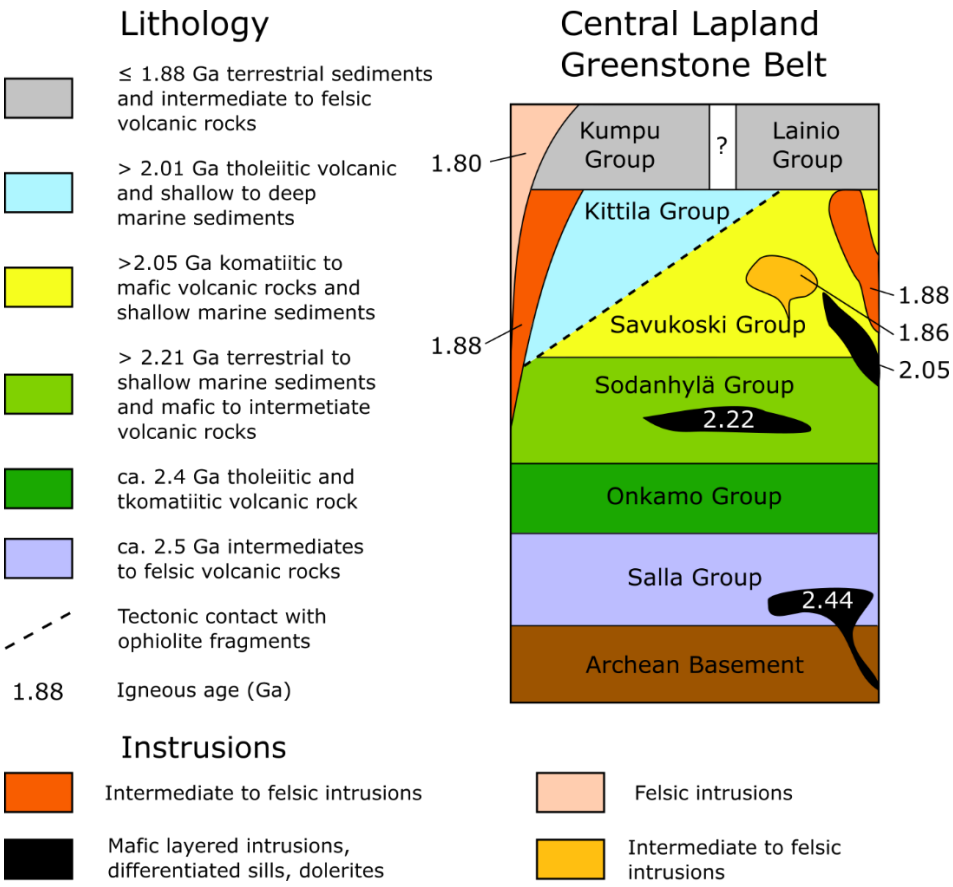

Figure 2 - Stratigraphic sequence of the Central Lapland Greenstone Belt (recreated from Niiranen et al., 2007).

The Kolari Shear Zone is a major N-S oriented oblique shear zone spanning a width of between 50-100 km, running close to the Swedish border in Northern Finland. The structures encountered within the shear zone are gently dipping and feature a strong SSW trending quartz and sillimanite mineral lineation on the foliation plane (Väisänen, 2002). This complex system of shearing accommodated both thrusting to the NNE and at a later stage reverse movement to the east, therefore it can be classified as a transpressional system.

Väisänen (2002) described the stages of deformation experienced in the region; The first deformation stage D1 is the oldest tectono-metamorphic feature in the CLGB, microscopically observable bedding parallel foliation, S1. This feature is most prominent in mica-rich sedimentary rocks within F2 fold hinges, that lie perpendicular to the S2 axial plane. They are also seen as inclusion trails within andalusite, garnet and staurolite porphryoblasts. In the second deformation stage D2, the most common feature in the majority of rocks is the S2 foliation which is mostly subparallel to bedding. Minerals typical of the foliation are protolith and metamorphic grade dependant; chlorite and muscovite in lower grade rocks, with the chlorite being replaced by biotite in higher grade rocks. The orientation of the foliation is mainly gently dipping to flat-lying with recumbent or reclining folding. Peak metamorphic conditions in the CLGB were most likely reached during deformation stage D2 (Lehtonen et al., 1998). A number of thrust, shear and fault zones comprise the structural makeup of the Kolari region, these form the Kolari Shear system, which itself is part of the larger Baltic-Bothnian Mega-shear (Väisänen, 2002). Thrusting events in the region during the D3 stage led to the reactivation of the D2 stage thrust and fault zones, leading to refolding of the D2 structures and the appearance of strong L3 lineation in the surrounding region of these thrust zones (Hiltunen, 1982; Väisänen, 2002). Due to the west to east directed thrusting that gave rise to the D3 structures, well developed, west to southwest plunging L3 lineation is seen in the areas surrounding the thrust zones, along with F3 folds whose axes plunge parallel to the lineation (Niiranen et al., 2007).

The main deposit types seen in the Kolari region are iron deposits and Iron Oxide-Copper-Gold (IOCG) deposits. The IOGC deposits are encountered in Hannukainen and Rautuvaara. These are defined as a group of diverse Cu-Au deposits to which several economically important deposits across the world belong, the concept of this classification was first brought forth by Hitzman et al. (1992). The deposits seen in the Hannukainen-Rautuvaara area are associated with the Kolari Shear zone and contain grades of Cu and Au that are typical of IOCG deposits. In 2001, the Geological Survey of Finland (GTK) created a project “Iron oxide-copper-gold in northern Finland” to study the occurrences of such IOCG deposits in Finland, and to create a suite of genetic models and tools for exploration in the Fennoscandian Shield. There are multiple occurrences of this ore type located in the Kolari region of the CLGB, they are hosted by clinopyroxene-dominated skarns that overlay the Archean Savukoski Croup supracrustal rocks and the 1.86 Ga Haparanda Suite intrusions (Niiranen, 2005). Similar deposit types are also seen in the northern Norrbotten area of Northern Sweden, where several economic and

non-economic Fe-oxide and Cu (-Au) deposits are located (Hitzman et al., 1992) including the significant apatite-iron deposits of Kiruna and Malmberget and the Aitik Cu-Au ores (Edfelt et al., 2005).

The Kolari deposits coincides with the thermal event related to the intrusion of voluminous S-type potassic granitoids found throughout northern Finland and Sweden (Hanski et al., 2001). The deposits are all located in the vicinity of the shear and faults zones that form the Kolari Shear Zone. Niiranen et al. (2007) describe the distinct metal associations found in the Kolari deposits, specifically Fe-Cu-Au ± Ag, Bi, Ba, Co, Mo, Sb, Se, Te, Th, U, LREE. Gold and copper concentrations are seen to be 0.1 - 4.5 wt.% and 0.1-6.6 g/t, respectively. Niiranen et al. (2007) found that two generations of sulphides exist in the Kolari region. The textural features within the magnetite-disseminated and Cu-Au mineralised albitites suggest that the magnetite and sulphides existed at the same time. Furthermore, no systematic distinction can be made in the chemical composition between the Cu-Au mineralised ironstone and barren ironstone units barring sulphur concentrations and related elements, this suggests the precipitation of the magnetite and the sulphides also happened at the same time. This is an important point when considering the source of seismic reflectivity. The formation of the ironstones and the Cu-Au mineralisation is thought to have occurred at the same time as the D3 stage thrusting event due to the S3 foliation of the ironstones and the orientation of the ironstone lenses parallel to the L3 lineation at the Laurinoja deposit in Hannukainen, along with U-Pb age data (Hiltunen et al., 1982). The later generation of sulphides are related to the crosscutting of the S3 foliation by brittle fractures, therefore they are post-D3 stage deformation. It is not known here if the sulphides are originating for a more distant source or just remobilised varieties of the pre-existing ones, however due to the low number of late fractures in the Kolari deposit they do not contribute much to the Cu-Au-budget (Niiranen et al., 2007).

The Hannukainen deposits are made up of the Kuervaara, Laurinoja, Vuopio and Lauka ore bodies (Figure 3). As seen in Figure 3, the HIRE survey profiles E1, V2, and V5 are all partially located in this area. The crossing point of profiles E1 and V5 is located on top of the Laurinoja deposit. Profile V5 runs through both Laurinoja and Vuopio, so at shallow depths these deposits may be visible in the seismic reflection profiles of this study. The Hannukainen ore bodies have a total inferred amount of iron ore of ca. 68 Mt as estimated by Hiltunen (1982). The Laurinoja ore body was estimated to contain ca. 33 Mt of iron ore with Fe content varying between 36

and 53 wt.%, making it the largest ore body in Hannukainen. Cu and Au content in Laurinoja were poorly constrained, but the whole ironstone lens was estimated to be 0.36 wt.% Cu and 0.15 ppm Au, unevenly distributed within the ironstone. Puustinen (2003) reported that of the 4.6 Mt of ore mined from Laurinoja, the grades were 43 wt.% Fe, 0.88 wt.% Cu and 1 ppm Au.

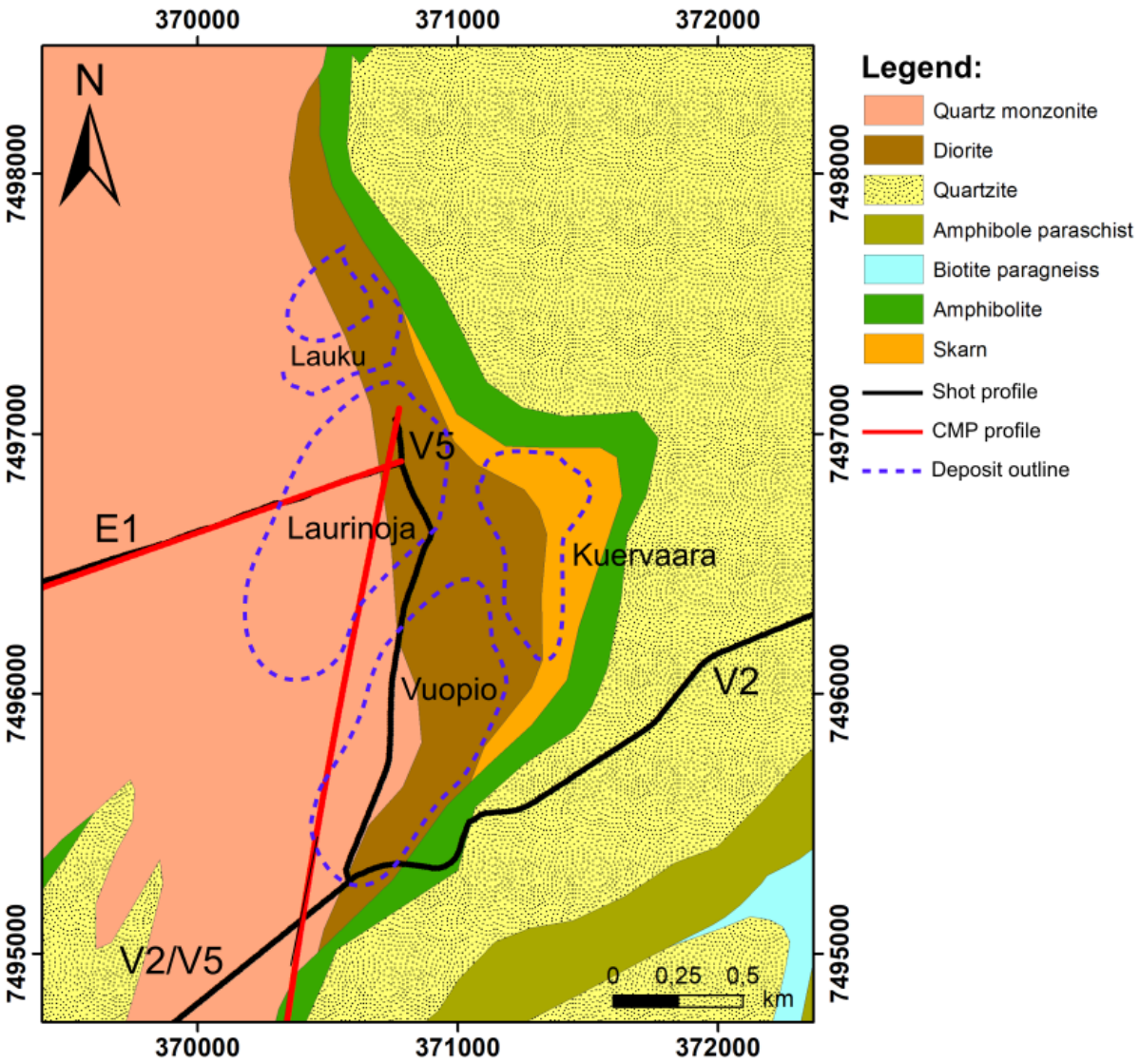

Figure 3 - Geological map of the Hannukainen mine site, four named deposits are known in the area, Laurinoja, Vuopio, Keurvaara and Lauku. HIRE survey profiles E1, V2 and V5 are all partially located in this region. Deposit locations estimated from Niiranen et al. (2007). Coordinates are in the EUREF-FIN ETRS-TM35FIN system. Lithology data: Bedrock of Finland 1:200 000 © Geological Survey of Finland 2016.

Laurinoja and Kuervaara have been open pit mined in the past. Laurinoja is located in the easternmost thrust zone of the Kolari Shear System, next to the Äkäsjoki fault. In the Hannukainen region the older structural features cannot be recognised as the developments of

strong foliation and lineation occurred during the D3 stage of deformation such that the D1 and D2 stage features have been overprinted. Altered wall rocks and silicate-banded ironstones show the best examples of S3 foliation and L3 lineation in the area. S3 lineation is found to be less developed in the sulphide-bearing ironstones, which appear unfoliated. S3 foliation is dipping at 30° west at Laurinoja, with the L3 lineation plunging to the southwest, along with the elongated lens-shaped ironstone units (Niiranen et al., 2007).

*Table 1 - Description of deposits at Laurinoja (Hannukainen) and Cu-Rautuvaara. Table from Niiranen et al. (2007), with data taken from Kinnunen (1980), Hiltunen (1982) and Puustinen (2003). *Production 1978-1990. ** Inferred.*

Deposit	**Laurinoja (Hannukainen)**	**Cu-Rautuvaara**
Size and grade	4.56 Mt* at 43% Fe, 1 ppm Au, 0.88% Cu 33 Mt** at 36-53% Fe, <0.1 - 11.0 % Cu, <0.1 - 6.6ppm Au, <0.1 - 17.7 ppm Ag, 20 - 1000 ppm Co	N4 Mt** weakly to moderately Cu–Au mineralised rock, <0.1–1.5% Cu, <0.1–2.6 ppm Au, <0.5–1.2 ppm Ag
Wall rocks	Monzonite, diorite, mafic metavolcanics rock	Monzonite, diorite, mafic metavolcanics rock
Main host rocks	Iron stone, clinopyroxene-amphibole skarn	Albitite
Opaques	Magnetite, pyrite, pyrrhotite, chalcopyrite ± molybdenite, native gold, tellurides	Molybdenite, poyrrhotite, clinopyroxene ± pyrite, uraninite
Gangue	Clinopyroxene, hornblende–actinolite, albite, biotite, ± scapolite, quartz, ccalcite, K-feldspar, garnet, epidote	Albite, anthophylllite, biotite, ± clino-pyroxene, quartz, titanite
Metal association	Fe, Cu, Au, S ± Ag, Bi, Ba, Co, Mo, Sb, Te, LREE	Fe, Cu, Au, S ± Ag, Ba, Bi, Mo, Se, Te, Th, U, LREE

Niiranen et al. (2007) describe the Laurinoja deposit as very similar in host rock and alteration as the Kuervitikko deposit to the north of Hannukainen (Figure 1). The physical make-up of the Laurinoja deposit consists of massive to silicate-banded magnetite-rich lenses hosted by

skarns. The skarn host rocks were formed near the intermediary zone between the Savukoski Group and the latter monzonite-diorite intrusions as described by Hiltunen (1982). Niiranen et al. (2007) describe the mineralogy of the deposit; the footwall consists of variably altered mafic metavolcanics rocks, quartzite quartz-feldspar schist and mica gneiss. The hanging wall consists of monzonite and variably altered diorite. The skarn host rocks are mainly clinopyroxene and amphibole dominated rocks. Occurring locally in the sequence are clinopyroxene-bearing scapolite skarns, thin (<0.5 m) garnet rich horizons, and albitite rocks with varying amounts of biotite, amphibole, K-feldspar and quartz. Also found in Laurinoja are pegmatitic granite dykes up to several metres in thickness. In places medium-grained granite dykes crosscut and brecciate the ore and wall rocks. Magnetite is the oxide mineral found most commonly at Laurinoja, with pyrite, pyrrhotite and chalcopyrite being the most common sulphides. Silicate gangue, chalcopyrite and magnetite have all had native gold detected within them. The gangue of the ironstone is comprised of clinopyroxene, amphibole, albite, scapolite, biotite, calcite and quartz. The sulphides found in Laurinoja are mainly disseminated, though sulphide veins in the iron stone, while skarn and altered wall rocks are found locally. Narrow (>30 cm) lenses and veins of pyrrhotite and chalcopyrite are found in the ironstones, along with fracture infill of chalcopyrite and pyrite.

The Cu-Rautuvaara deposit is located 7 km SW of Hannukainen (Figure 1), Niiranen et al. (2007) describe it as partly similar to the Hannukainen deposits, but the host rocks are monzonite and albitite instead of skarn and iron stones. Even with this difference the structure and general features are so strikingly similar that the formation of the deposit would have been the result of the same kind of geological processes as formed Laurinoja and Kuervitikko to the north (Niiranen et al., 2007). This deposit is located in the northwest limb of a major southwest opening syncline next to the same thrust zone as Laurinoja. The S3 foliation and L3 lineation are well developed, but not as pronounced as that seen in Laurinoja. The main structure trend in is a southeast direction, dipping steeply. Most of the ore of the Cu-Rautuvaara deposit is hosted by magnetite-disseminated, biotite- and/or anthophyllite-bearing albitite. These form a lens that is ~45 m thick. The ironstone lenses and clinopyroxene-amphibole skarn encountered are similar to those in Laurinoja, but smaller in size. The hanging wall consists of diorite and monzonite, while the footwall consists of altered mafic metavolcanics rock. Dominant sulphides in this area are chalcopyrite and pyrrhotite, with local occurrences of pyrite. The dominant oxide mineral is magnetite, with small local occurrences of uraninite within the

clinopyroxene-amphibole skarn. The gangue minerals are albite, anthophyllite, biotite and quartz (Niiranen et al., 2007).

Metasomatic alteration related to the ironstones and Cu-Au mineralisation are in the form of different combinations of albitite, amphiboles, biotite, clinopyroxenes (diopside–hedenbergite), K-feldspar, magnetite, scapolite, calcite, and sulphides (pyrite–pyrrhotite–chalcopyrite) alteration (Niiranen et al. 2007). Zoning can be distinguished around the Laurinoja deposit in Hannukainen but is not clearly seen at Cu-Rautuvaara. This is suggested to be due to the lack of suitable structures to promote fluid flow in this area (Niiranen et al., 2007). Where zoning is best seen in Laurinoja, the halo of alteration can be split into distal and proximal zones in the hanging and footwalls. This is something that could potentially be identified in the seismic reflection data. Assemblages of alteration here vary due to the primary rock type, but for the distal zones, albite ± scapolite, biotite, and K-feldspar are the dominant alterations minerals; and for the proximal zones clinopyroxenes, amphiboles and magnetite ± calcite are the dominant alterations. Clinopyroxene is encountered at the intermediate zone between distal to proximal, with the outer distal boundary being defined by the occurrence of albite (Niiranen et al. 2007). The amount of biotite and K-feldspar in distal zones increases towards the proximal zone, with the distal zone being dominated by these minerals right next to the proximal zone. This changing mineral composition and the general changed from distal to proximal is best seen in footwall mafic metavolcanic rocks. Clinopyroxene is the dominant alteration in the proximal zones, with calcic amphibole often occurring alongside or instead of the clinopyroxene as the main alteration mineral. Locally amounts of albite, biotite, K-feldspar, scapolite, calcite, and quartz can exceed that of the clinopyroxene in the proximal zone. These proximal zone alteration assemblages are similar to that of the ironstone, besides the abundant magnetite seen in ironstone (Niiranen et al., 2007). Magnetite is also seen outside the ironstone, in both the proximal and distal zones, where it can be seen locally up to a 15 vol.% (Niiranen et al., 2007). The Hannukainen and Cu-Rautuvaara deposits are of metasomatic replacement type rather than metamorphosed syngenetic iron formations. Niiranen et al. (2007) note that there is a major difference seen in the zoning at Laurinoja in comparison to classic skarn deposits though the calcite alteration assemblages are similar to that you would encounter in calcic-iron skarns. This atypical zoning along with the thrusting and shearing experienced in the Kolari region suggest that the ironstone represent the structural base of the shear system in a hydrothermal system, with the zoning being caused by fluid flux, fluid evolution and fluid interacting with the wall rocks in and around the areas experiencing thrusting.

At Laurinoja, the sulphides mainly occur within the ironstone and proximal zones, but Fe- and Cu-sulphides ranging from 1 to 10 vol.% are also seen locally in all altered rocks, independent of alteration assemblages (Niiranen et al., 2007). At Cu-Rautuvaara, though the zoning is poorly developed the alteration assemblages are close to what is seen at Laurinoja. Clinopyroxene skarns occur in a thin sequence in the hanging wall, with similar alteration assemblages to the proximal zones at Laurinoja. The main Cu-Au mineralisation occurs within magnetite-disseminated anthophyllite and biotite-bearing albitite. (Niiranen et al., 2007)

Geochemical analysis undertaken by Niiranen et al. (2007) suggested that the monzonite and diorite were derived from the same magma source and found the chemical composition of the monzonite was typical for that of 1900 - 1860 Ma Haparanda Suite intrusions found all over NW Finland and northern Sweden (Mellqvist et al., 2003). At Laurinoja the chemical composition of the diorite and metavolcanics rocks shows zoning that corresponds to the zoning of the alteration assemblages. TiO_2-Al_2O_3, Zr-AI_20_3, and Zr-$Ti0_2$ ratios were taken from the clinopyroxene-amphibole skarns and ironstones, and again they showed correlation that would suggest these two rock types share a common origin, with some variation in the immobile element ratios suggesting the protolith for these rocks was locally heterogenous and/or made up of several rocks (Niiranen et al., 2007). The REE patterns in the skarns and ironstones are somewhat similar to the distal altered metavolcanics rock, suggesting further that the metavolcanics were the precursor to the skarns and ironstones. Niiranen et al. (2007) found that the albitites and scapolite skarns were the most geochemically peculiar rocks in the Kolari region. These are found throughout the ore-bearing sequence, with the albitites mainly in the hanging wall and the scapolite skarns in the proximal zone, therefore it is likely that the protolith for these rocks consisted of several rock types. The REE pattern of the Cu-Au mineralised magnetite-disseminated albitite at Cu-Rautuvaara does not correlate with any other rock type in the area.

3 Petrophysical considerations

Alteration can have major effects on the petrophysical properties of crystalline rocks. Katsube & Kamineni (1983) found that in crystalline rocks located in Ontario, Canada, the alteration of these rocks caused a decrease in porosity and permeability. This being due to reduction of the

aperture of pore pathways due to the dissolution of certain minerals followed by secondary mineral deposition. As such, these petrophysical changes will have an effect on the resulting seismic reflectivity of the rocks. In Junno et al. (2020), the effect of sulphide mineralisation and alteration on the reflectivity properties of the rock types seen at the Kevitsa mine site is investigated by theoretical modelling. It was found that less than half of the core sample logs had alteration data available, so forward modelling of the effect of sulphide mineralisation and alteration on seismic P-wave velocities and densities was completed. Theoretical densities and velocities for the Kevitsa rock types were calculated using plausible modal compositions based on previous petrographic data. Different mixture models were made by increasing the amount of sulphide mineralisation or specific alteration mineral. The results of this modelling show sulphide mineralization alone is not enough to exceed the detection limit of the seismic data. However, in combination with alteration these could produce observable reflections when in contact with unaltered and unmineralised rocks. This is relevant to this study as it was found by Niiranen et al. (2007) that no systematic distinction can be made in the chemical composition between the Cu-Au mineralised ironstone and barren ironstone units barring sulphur concentrations. The depth of data that was computed by Junno et al. (2020) is not applicable for this study, but a simple look at the seismic velocities and densities of the main lithologies seen in the Hannukainen area, along with the common alteration and ore minerals can reveal in a general sense how these minerals might affect the P-wave velocities and densities of these rock types. Table 2 and Figure3 contain the P-wave velocity and density values for typical rock types and rock forming minerals in the Hannukainen area. Access to comprehensive petrophysical data from the Hannukainen area was not available, so tabled values from Schön (2015), Junno et al. (2020) and Elbra et al. (2011) have been used. What is important to note here is that point values have been used to represent the rock and mineral types, when in reality more a range of values would represent them, and also these values are not from the Hannukainen area. This analysis has its obvious limits, but this has been done in an effort to get some representation of the trends that could be seen in Hannukainen.

Table 2 - Seismic P-wave velocity and density values for typical rock types and rock forming minerals in Hannukainen. References - 1 - Schön (2015), 2 - Junno et al. (2020), 3 - Elbra et al. (2011).

Rock type	**V_P (m/s)**	**ρ (kg/m^3)**	**Reference**
Diorite	5600	2823	1
Granite	5010	2705	1
Metavolcanics	5938	2905	2
Skarn	6267	3034	3
Alteration mineral type			
Albite	5940	2630	1
Amphibole	6849	3283	2
Biotite	5350	3050	1
Calcite	6540	2712	1
Clinopyroxene	8104	3269	
K-feldspar	4680	2820	1
Main ore mineral type			
Magnetite	7271	5202	2
Pyrite	7990	4910	2
Pyrrhotite	4600	4710	2
Chalcopyrite	5120	4280	2

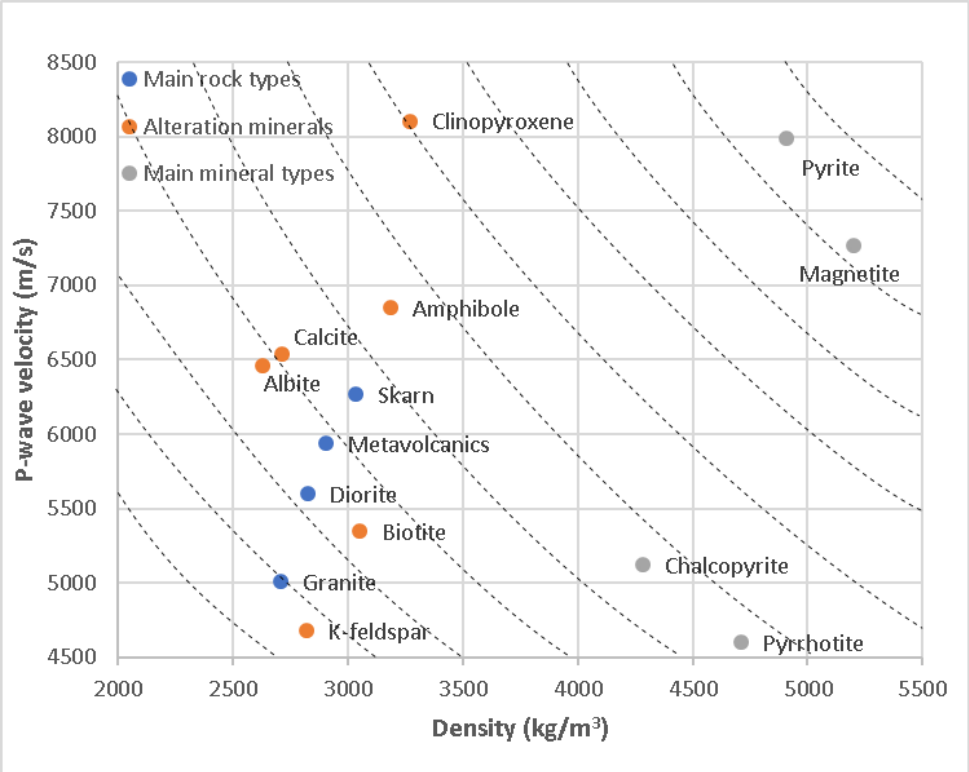

Figure 4 - Graph showing the seismic velocity and density values for the main rock types (blue dots), main mineral types (grey dots) and alteration minerals (orange dots) in Hannukainen. The dashed black isolines represents an approximate constant acoustic impedance, the difference between two isolines represents a detectable reflection due to a reflection coefficient difference of 6% (Salisbury et al. 1996).

Sufficient data on the common rock types of the area is not available, with no values for the albitite, monzonite and ironstones available. The skarns and ironstones are the main host rocks at Laurinoja for mineralisation. Taking some values from other Finnish studies is the best we can do to give an idea of the petrophysical properties of these rock types even if they will not be completely accurate. Petrophysical values have been taken for the metavolcanics from Junno et al. (2020) and skarn values from Elbra et al. (2011), a clinopyroxene-tremolite skarn, which could be similar to the clinopyroxene-amphibole skarn seen in Hannukainen, ironstone values were not found. Reflections will arise from seismic impedance contrasts above the 6% detection limit (black dashed isolines in Figure 4) (Salisbury et al. 1996). The common ore minerals are easily seen to have much higher densities than the host rock types, with magnetite and pyrite having much higher P-wave velocity also. The mineralisation of these rocks may lead to increased seismic amplitudes with sufficient mineralisation, when in contact with unmineralised rock. Mineralisation is structurally controlled, so that it would be cumulated to structures that have acted as pathways for fluid circulation, meaning that the fracturing will play a role in the resulting petrophysical properties. The alteration minerals in Figure 4 show somewhat similar densities and velocities to the unmineralised host rocks, so when the mineralised rocks get altered, this should change the densities and velocities somewhat again depending on the alteration intensity. With a high enough intensity, it could produce varying amplitude strength along a mineralised horizon. For example, the alteration of skarn by adding the alteration products of biotite and k-feldspar as seen in Figure 4 could decrease the seismic velocity and density causing a seismic impedance polarity change if the alteration intensity is large enough to produce a reflection signal between the unaltered and altered rocks. A deep dive into this data would be needed to fully conclude what kind of mineralisation and alteration would best produce strong seismic reflections. This is an area of study for this region that could be greatly expanded upon, with more data for local rock and mineral type P-wave velocity and density needed.

Further analysis was done by Junno et al. (2020), by implementing an artificial neural network analysis called Self Organising Map (SOM) analysis is performed. Borehole data at the Kevitsa Ni-Cu-PGE deposit is used to resolve the origin of reflectivity within the deposit. At Kevitsa there is extensive borehole data available for this type of study, with ~900 boreholes drilled within the resource area. The SOM analysis suggested that low seismic velocities are seen in the regular ore zones and these can be reflective when in contact with unmineralised and unaltered olivine pyroxenite. Also, it is indicated that alteration is associated with mineralised

zones, and according to the theoretical calculations, this alteration is needed to cause detectable reflectivity. As such it is suggested that the seismic reflectivity observed at Kevitsa could be resulting from alteration and possibly the presence of sulphide minerals. This is very relevant to this study and an assumption that the source of seismic reflectivity seen in the Hannukainen is a result of the alteration previously described could be plausible.

4 Theoretical Background

4.1 Seismic wave motion

Elasticity is the prerequisite for the propagation of waves through a medium. An elastic material is a material that return to its original form after being deformed by an applied load. As such, a seismic wave is a self-sustaining disturbance of a medium that transports energy through the medium without transporting the medium itself. In some cases (e.g. close to the focus of an earthquake) the material can move past its elastic limit, beyond which it will be permanently deformed. In an elastic medium, Hooke's Law states that stress (e) is linearly proportional to strain (σ), so that, for a 1D case:

$$\sigma = Ee \tag{1}$$

where *E* is Young's Modulus (E = σ/e), the ratio of extensional stress to extensional strain. Increasing stress is accompanied by increasing strain until the elastic limit of the material is reached. Hooke's Law holds for seismic waves everywhere except for very near source, as the strains involved are so small. The stress tensor describes fully the state of stress in a particular medium, consisting of a matrix of 9 terms:

$$\boldsymbol{\sigma} = \sigma_{ij} = \begin{pmatrix} \sigma_{xx} & \sigma_{xy} & \sigma_{xz} \\ \sigma_{yx} & \sigma_{yy} & \sigma_{yz} \\ \sigma_{zx} & \sigma_{zy} & \sigma_{zz} \end{pmatrix} \tag{2}$$

where σ_{xx}, σ_{yy} and σ_{zz} are the three normal stresses and the other six terms are shear stresses. The index i indicates the direction in which the stress acts, while the j index refers to the orientation of the surface on which the stress is acting (i. j = x, y, z). Linking the nine components of stress to the nine components of strain yields eighty-one terms that specify this

relationship. In the case of isotropic material, properties are independent of direction and the number of non-zero elastic constants is reduced to twelve. These can be expressed a function of only two elastic constants, typically Lame`s constants λ and μ. From these parameters other elastic constants like Young's Modulus can be calculated and used to relate stress and strain.

Seismic waves come in the form of body waves (P- and S-waves) and surface waves (Rayleigh, Love, Stonely waves). As the name suggests body waves travel through the subsurface of the Earth, whereas surface waves only travel along the surface. For seismic reflection surveys it is body waves that are the source of reflections. Surface waves, Love, Rayleigh and Stonely (in boreholes) waves, are considered noise in conventional reflection seismics. P- and S-waves differ in the particle motion that accompanies them as they pass through a medium. P-waves are the faster of the two and travel in a compressional manner, a P-wave passes through the medium with alternating compression and dilation. Particle motion occurs parallel to the direction of propagation (longitudinal). P-waves typically travel at speeds of 5-7 km/s in the Earth's crust. S-waves are slower, typically travelling at 3-4 km/s in the Earth's crust therefore arriving after P-waves. Particle motion is such that alternating transversal motion occurs as the wave passes though the medium. The Earth polarises the S-wave motion, giving rise to two types of S-wave, the more common vertical shear waves (shear vertical, SV) and horizontal shear waves (shear horizontal, SH). S-waves don't travel through water or air as shear stress cannot act in these medium, nor do they exist in the Earth's outer core.

For example, Shearer (2019) sets out the framework for P- and S- wave motion starting at Newton's 2nd Law, which describes how forces originating from the stresses can be linked to displacements that can be measured. And, when combined with Hooke's Law and an equation that links strain and displacement, Navier's equation of motion is attained, which describes displacement within an elastic body:

$$\rho \frac{\partial^2 \boldsymbol{u}}{\partial t^2} = (\lambda + \mu)\nabla(\nabla \cdot \boldsymbol{u}) + \mu \nabla^2 \boldsymbol{u} \tag{3}$$

where ρ is density, $\boldsymbol{u}$ is the displacement field, ∇ is the nabla operator, ∇^2 is the Laplacian operator λ and μ are Lame parameters. The Navier equation can be solved using Helmholtz decomposition which expresses any vector field in terms of scalar and vector potential:

$$\boldsymbol{u} = \nabla\Phi + \nabla \times \boldsymbol{\psi} \tag{4}$$

where $\boldsymbol{u}$ is the displacement vector field, Φ is scalar potential and ψ is vector potential. Here it can be said that:

$$Vector\ potential: \nabla \times \boldsymbol{\psi} = 0 \tag{5}$$
$$Scalar\ potential: \nabla\Phi = 0$$

The part of Equation 4 with vector potential experiences no volume change, therefore this represents the S-wave. The part of Equation 4 that with scalar potential experiences no rotation, therefore this represents the P-wave. When Equation 4 is substituted into the equation of motion it yields two wave equations, one for P-waves (Equation 6) and one for S-waves (Equation 7):

$$\nabla^2\Phi = \frac{1}{\alpha^2}\frac{\delta\Phi^2}{\delta t^2} = 0 \qquad \alpha = \sqrt{\frac{\lambda + 2\mu}{\rho}} \tag{6}$$

$$\nabla^2\boldsymbol{\psi} = \frac{1}{\beta^2}\frac{\delta\boldsymbol{\psi}^2}{\delta t^2} = 0 \qquad \beta = \sqrt{\frac{\mu}{\rho}} \tag{7}$$

where α is P-wave velocity, β is S-wave velocity, and ρ is density. This flow of equations, along with basic principles like conservation of energy, laws of physics (Snell's Law) and regularly occurring boundary conditions provide the basis for all problems in theoretical seismology.

4.2 Seismic waves at boundaries

How a wave is partitioned once it meets a boundary is expressed by Snell's Law, which describes the relationship between the angles of an incident and a refracted and reflected wave as the wave passes through a boundary between two contrasting isotropic media. Snell's Law was derived for light waves but is applicable to seismic waves also. Snell's Law states the that the ratio of the sines of the angles of incidence and refraction is equal to the ratio of phase velocities in the medium. It describes the physical change in direction a waveform will experience when passing through media with contrasting velocities and the partial conversion and reflection of P- and S- waves seen at this boundary. Snell's Law is expressed as:

$$\frac{sin\theta_1}{sin\theta_2} = \frac{v_1}{v_2} \tag{8}$$

where θ_1 is the angle of incidence, θ_2 is the angle of refraction and v_1 and v_2 are the medium velocities above and below the boundary between the media, respectively. Figure 5 illustrates this, with the incident P-wave seen to encounter the boundary between the upper and lower media. The upper medium has P- and S-wave velocities of v_{P1} and v_{S1}, respectively, and the lower medium has P- and S-wave velocities of v_{P2} and v_{S2}, respectively. When the incident P-wave hits the boundary, it partitions into reflected and refracted P- and S-waves. The reflected P-wave has a reflection angle of θ_{1P}, the reflected S-wave has a reflection angle of θ_{1S}, the refracted P-wave has a refraction angle of θ_{2P}, and the refracted S-wave has a refraction angle of θ_{2S}. Each wave is related by the ray parameter p, which is the geometric property of the ray that remains constant throughout its path, for each resulting wave it can be expressed as:

$$p = \frac{sin\theta i}{v_i} = \frac{sin\theta_{1P}}{v_{1P}} = \frac{sin\theta_{1S}}{v_{1S}} = \frac{sin\theta_{2P}}{v_{2P}} = \frac{sin\theta_{2S}}{v_{2S}} \tag{9}$$

The critical angle θ_C is the incident angle at which the refracted wave travels along the interface of the two media. Below the critical angle, the incident P-wave is reflected and refracted as seen in Figure 4, and above the critical angle and all energy is reflected generating only reflected waves.

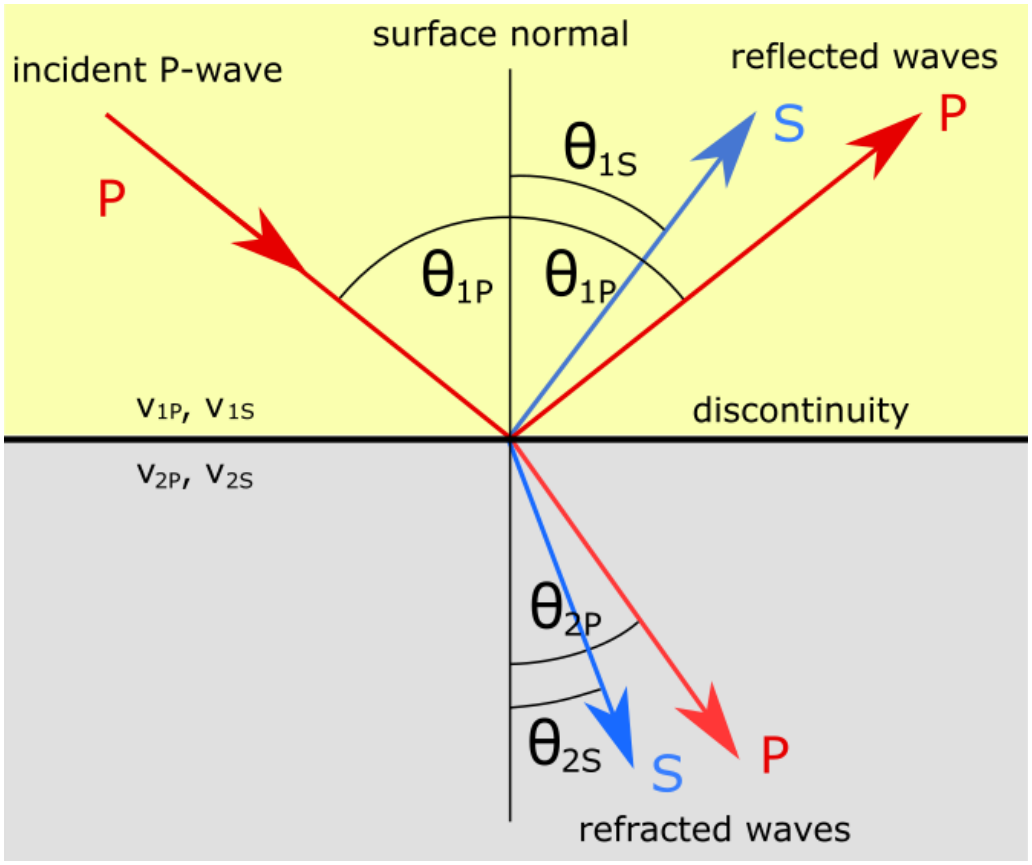

Figure 5 - Snell's Law for seismic waves with a solid-solid interface (modified from Völgyesi & Moser, 1982).

The reason both P- and S- waves are refracted and reflected once the incident P-wave hits the boundary is that boundary conditions must be met for the two contrasting media where the displacement across the interface and the normal and shear stresses must be continuous.

4.3 The seismic reflection method

The seismic reflection method is based on mapping contrasts in subsurface seismic impedance, caused by changes in the velocity of the seismic wave and the density of subsurface materials. In practice, seismic receivers (geophones) are set out strategically in a manner best suiting the terrain and areal coverage desired. The geophones are typically laid out in a straight line or in a grid formation. These can be autonomous nodes or connected to a seismic cable that runs to a control station. Geophones can be grouped at each point; this will improve the signal-to-noise ratio of the attained data at each point. A source of seismic energy is used at a regular spacing along the survey profile, these are called shot points. There are many different source types e.g. hammer and plate, explosives, and Vibroseis thumping machine. The source type is chosen based on the needs of the survey. The source creates seismic waves which interact with the

different layers of the subsurface, bouncing off, passing through or travelling along the layers i.e. reflections and refractions. The waves that return to the surface are recorded by the geophones. From this a time-domain seismogram is formed showing reflections at different 'depths' of travel time which will later be converted to depth in metres based on a velocity model.

The Common Mid-Point (CMP) Method is used to improve the signal-to-noise ratio of seismic reflection data. This is done in multichannel seismic acquisition by collecting together recording that share a point on the surface - the CMP- that is halfway between the source and receiver (Figure 6A). These recording are then processed such that they can be summed together. By doing this the seismic data is enhanced due to the redundancy of signals from the same reflection points among source-receiver pairs. In the case of a horizontal reflector, the CMP will be located vertically above the common depth point (CDP), which is where the reflections recorded with difference source-receiver pairs for the same CMP will originate from. In the case of a dipping reflector, the CMP and CDP will not be located directly vertical for each other, due to the effect the dipping nature of the reflector has on the wave paths (Figure 6B).

One CMP can be sampled by several different sources and receivers. The number of recordings with different source-receiver pairs that share the same CMP is called the fold. When source and receiver spacing are equal then the max fold will be the number of receivers, and the CMP separation will be half the distance between geophones. Figure 6C shows how the CMP method works, with a line of sources (S_1 to S_4) and a line of geophones (G_1 to G_4). One source will produce four reflections that will be recorded at each geophone. These reflections will correspond to a CMP located at the halfway point between the different source/receiver pairs. There will be differing numbers of reflections at each CMP position due to the geometry of the survey. The first CMP is the location of the single reflection R_1 which comes from the source-receiver pair S_1-G_1. The next CMP has 2 reflections from S_1-G_3 and S_2-G_4. The max fold is achieved at the CMP of reflection point R_4 which has four source-receiver pairs producing reflections (Figure 6C, highlighted in blue).

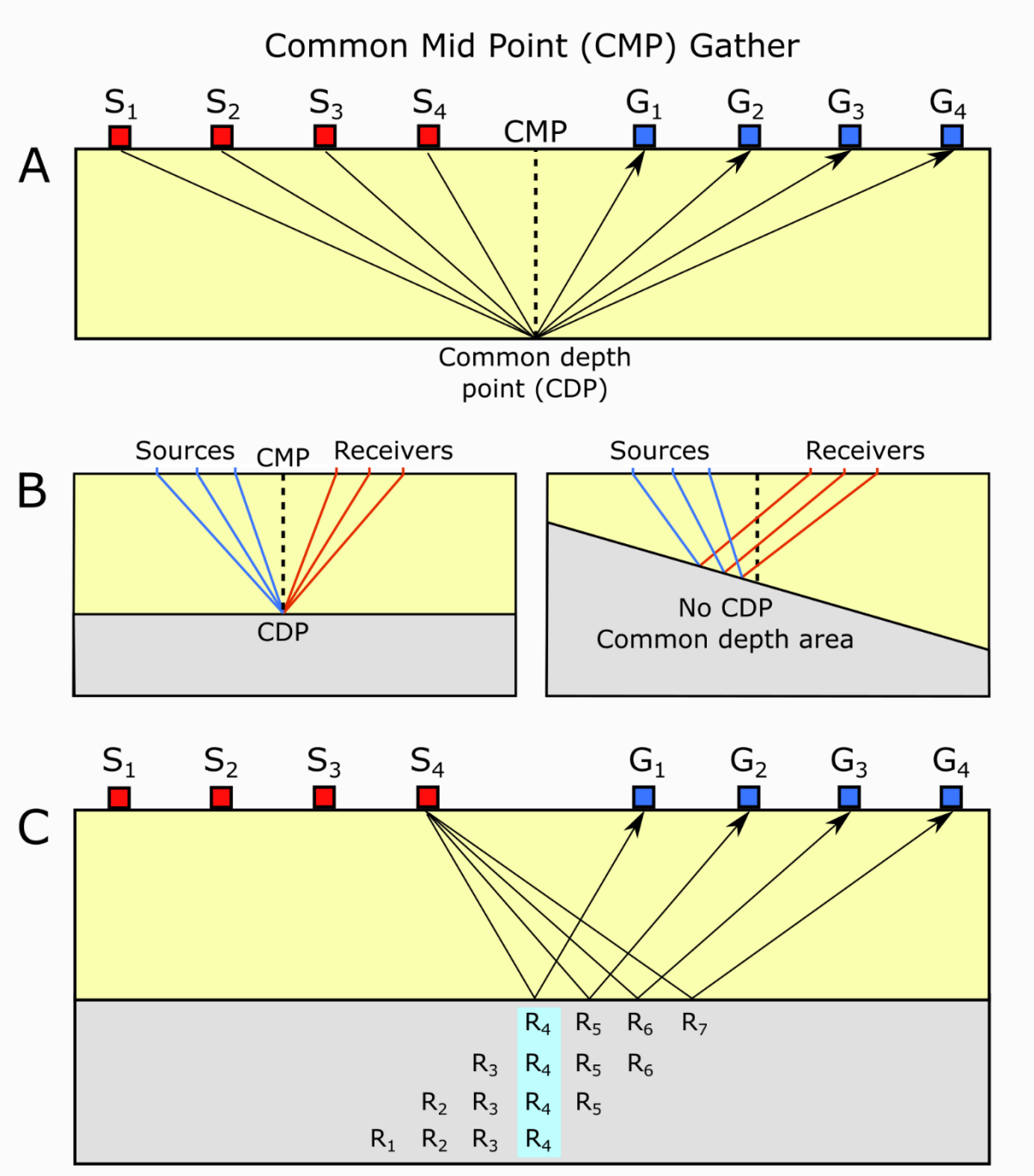

Figure 6 - A - The formation of a CMP from source-receiver pairs. B- The effect a dipping reflector has on forming a CDP in comparison to a horizontal reflector. C - Max fold is reached at the CMP which shares the most shot-receiver pairs.

The two most common types of gather typically used for land data processing can be attained from this data, shot point gather and CMP gather. A shot point gather includes recordings of all receivers from one source, whereas a CMP gather includes all the traces that have a common CMP.

4.4 Factors affecting the amplitudes of seismic waves

Various processes in the subsurface affect the amplitude of the reflections (Figure 7). Geometrical spreading is the effect on the seismic wavefront as it travels through the earth. It is the expansion of a wavefront traveling out from a point source in a spherical manner, decreasing the amplitudes as the energy is distributed across the expanding wavefront. In a constant velocity medium seismic energy decreases inversely to the square of the distance, however in a multi-velocity layer model, like Earth, the ray paths bend. Seismic velocity typically increases with depth, so the energy decay is faster. Spherical divergence will be expressed as a function of travel time due to the nature of seismic reflection recordings. By replacing distance with the product of travel time and average velocity it can be seen that attenuation is also dependant on velocity (Sheriff, 1975). Newman (1973) states that proper compensation of divergence effects is mandatory in seismic reflection processing if reflection amplitudes are to be of diagnostic value. Another process that effects seismic amplitude is absorption, where seismic waves lose energy as they travel through the subsurface as the energy is transformed into heat. The seismic wave experiences a decrease in amplitude that is approximately exponential with distance, this can be expressed as:

$$A = A_0 e^{-ax} \tag{10}$$

Where amplitude A is separated from amplitude A_0 by a distance x, and a is the absorption coefficient.

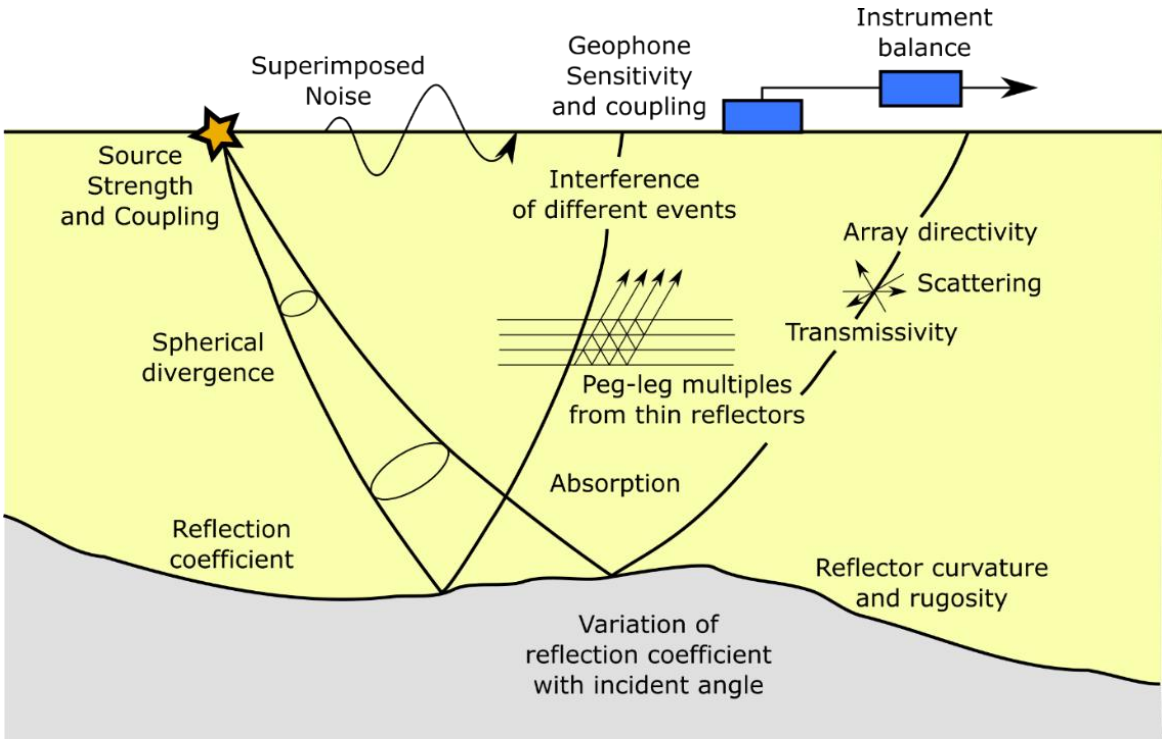

Figure 7 - Factors affecting amplitude in seismic reflection surveying (recreated after Sheriff, 1975).

Many other factors have an effect on the amplitude of the seismic waves, as seen in Figure 7. Peg leg multiples are a type of short-path multiple reflection, where a succession of reflection occur at different interfaces in the subsurface with asymmetric ray paths. Losses by transmission through interfaces and peg leg multiples are closely linked (Sheriff, 1975). Scattering can occur when the seismic wave meets inhomogeneities in the subsurface material. These geometrical factors, spherical divergence, absorption, transmissivity losses, scattering and peg leg multiples will all cause a general decrease in amplitude with time (Sheriff, 1975).

Seismic source strength and coupling refers to the size and nature of the seismic source and how well the source energy is transmitted to the subsurface. If the chosen source that is too small, then the resulting amplitudes will be weak. This is a very important thing to consider in survey design. When carrying out the survey the coupling of the source also needs to be carefully managed. For example, often an explosive source is inserted into a shallow hole to make sure as much seismic energy as possible transfers through the subsurface. The receivers must also be installed correctly to ensure the best coupling with the ground to receive as much of the returning wave energy as possible.

The reflection and transmission coefficient express how the energy is partitioned at a boundary, and as such will have major impact on the amplitudes of the seismic waves. These are expressed in the case of normal incidence as:

$$R = \frac{\rho_2 v_2 - \rho_1 v_1}{\rho_2 v_2 + \rho_1 v_1} \tag{11}$$

$$T = \frac{2\rho_2 v_2}{\rho_2 v_2 + \rho_1 v_1} \tag{12}$$

where, R is reflection coefficient, T is the transmission coefficient, ρ is density, v is seismic velocity and the indices *1* and *2* denote the first and second layers respectively. The product of density and seismic velocity is known as seismic impedance (I). A higher contrast in acoustic impedance of the layers will result in higher reflection coefficient and mean a higher amplitude in the seismic record coinciding with the reflector. The reflection coefficient varies with incident angle, and in the case on non-normal incidence will have to be solved using the Zoeppritz equations (Section 3.5).

The nature of the reflectors will also affect the amplitudes, how curved they appear and the roughness of their surface causes amplitude variation across the reflector. Curvature will affect the amplitude differently depending on whether the reflector is concave upward, or convex upward. A concave upward reflector will cause an increase in seismic amplitude due to the wave experiencing focusing, while a convex upward reflector will defocus the seismic wave causing a decrease in amplitude. Interference of different events arriving at the receiver at the same time has an effect on the amplitudes. If the waves get added together in-phase (constructively) they will cause an increase in amplitude, but if they get added together out-of-phase (destructively) they will cause a decrease in amplitude, in comparison to if they had arrived separately (Sheriff, 1975).

4.5 Amplitude vs. offset (AVO) analysis

AVO analysis examines the dependency of the amplitude of a seismic wave on the offset between the seismic source and receiver. A change in offset causes an accompanying change in the angle of incidence experienced by the seismic wave. This change will have an effect on

the amplitude of the seismic wave typically caused by changes in lithology or mineralogy and fluid content in the surrounding area of the reflector. Studying this change can reveal information about the physical properties of the subsurface material. This technique has been used to study a range of different rock characteristics such as porosity, density, seismic velocity, and an AVO effect can e.g. be an indicator of potential hydrocarbons.

In this study, the AVO analysis will be used in a hard rock setting to see if clear0 AVO effects can be observed and further linked to lithological variations, rock alteration and mineralization. The AVO response is based on the relationship between the angle of incidence of the seismic wave. In the case of normal incidence, the reflection coefficient as presented in Equation 11 is used. In the case of non-normal incidence, the Zoeppritz equations (Zoeppritz, 1919), which consider all angles of incidence, must be looked at.:

$$\begin{bmatrix} R_P(\theta_1) \\ R_S(\theta_1) \\ T_P(\theta_1) \\ T_S(\theta_1) \end{bmatrix} = \begin{bmatrix} -\sin\theta_1 & -\cos\phi_1 & \sin\theta_2 & \cos\phi_2 \\ \cos\theta_1 & -\sin\phi_1 & \cos\theta_2 & -\sin\phi_2 \\ \sin 2\theta_1 & \frac{V_{P1}}{V_{S1}}\cos 2\phi_1 & \frac{\rho_2 V_{S2}^2 V_{P1}}{\rho_1 V_{S1}^2 V_{P2}}\sin 2\theta_2 & \frac{\rho_2 V_{S2} V_{P1}}{\rho_1 V_{S1}^2}\cos 2\phi_2 \\ -\cos 2\phi_1 & \frac{V_{S1}}{V_{P1}}\sin 2\phi_1 & \frac{\rho_2 V_{P2}}{\rho_1 V_{P1}}\cos 2\phi_2 & -\frac{\rho_2 V_{S2}}{\rho_1 V_{P1}}\sin 2\phi_2 \end{bmatrix}^{-1} \begin{bmatrix} \sin\theta_1 \\ \cos\theta_1 \\ \sin 2\theta_1 \\ \cos 2\phi_1 \end{bmatrix} \quad (13)$$

where reflection coefficient R_P refers to the reflected P-wave, R_S to the reflected S-wave, T_P to the transmitted P-wave, T_S to the transmitted S-wave, θ_1 is the angle of incidence, θ_2 is the angle of the transmitted P-wave, φ_1 is the angle of the reflected S-wave, and φ_2 is the angle of the transmitted S-wave, V_P and V_S are the seismic P- and S-wave velocity respectively, and ρ_1 and ρ_2 are the densities of the respective layers. This set of equations describes the partitioning of seismic wave energy at the interface between two layers and relates the amplitude of the incident P-wave and the reflected and refracted P- and S-waves to the seismic wave's angle of incidence. This allows to study how the amplitude of the returning seismic wave is affected by a change in the angle of incidence.

However, the difficulty of applying the Zoeppritz equations due to their complexity led to approximations being formulated in the 1980's when discussion about AVO was becoming popular. Aki & Richards (1980) formulated an approximation of the Zoeppritz equations, yielding solution for the P-wave reflection coefficient (R_{PP}) as:

$$R_{PP}(\theta) \approx \frac{1}{2}(1 - 4p^2V_S^2)\left(\frac{\Delta\rho}{\rho}\right) + \frac{1}{2\cos^2\theta}\cdot\frac{\Delta V_p}{V_p} - 4V_S^2p^2\frac{\Delta V_s}{V_S} \quad (14)$$

where $\Delta\rho = \rho_2 - \rho_1$, $\Delta V_P = V_{P2} - V_{P1}$, $\Delta V_S = V_{S2} - V_{S1}$, $\rho = (\rho_2 + \rho_1)/2$, $V_P = (V_{P2} + V_{P1})/2$, $V_S = (V_{S2} + V_{S1})/2$, $\theta = (\theta_2 + \theta_1)/2$ and p is the ray parameter. This approximation was agreeable as it yielded three terms expressing P-wave velocity, density and S-wave velocity. The first order approximation by Aki & Richards (1980) was the basis for the Shuey (1985) approximation, which was motivated by rules set out by Koefoed (1955) who tirelessly computed reflection coefficient versus angle out to 30 degrees for 17 separate sets of elastic properties, describing the relationship of AVO response and Poisson's ratio change across a boundary. Poisson's ratio is defined as the ratio of the change in the width per unit width of a material, to the change in its length per unit length, resulting from strain. This led to the reformulation the Zoeppritz equation to include Poisson's ratio, giving the expression for the reflection coefficient as:

$$R(\theta) = R_0 + \left[A_0R_0 + \frac{\Delta\Upsilon}{(1-\sigma)^2}\right]\sin^2\theta + \frac{1}{2}\frac{\Delta V_P}{V_P}(\tan^2\theta - \sin^2\theta) \quad (15)$$

where, R_0 is the reflection coefficient at normal incidence, Υ is Poisson's ratio, and A_0 is given by:

$$A_0 = B_0 - 2(1 + B_0)\frac{1 - 2\Upsilon}{1 - \sigma} \qquad B_0 = \frac{\frac{\Delta V_P}{V_P}}{\left(\frac{\Delta V_P}{V_P} + \frac{\Delta\rho}{\rho}\right)} \quad (16)$$

where $\Delta\sigma = \sigma_2 - \sigma_1$, $\sigma = (\sigma_2 + \sigma_1)/2$ and A_0 gives the variation of R(θ) in the approximate range of $0 > \theta > 30°$. For the case of no Poisson's ratio contrast. The Shuey (1985) three-term solution can be broken down into the first term R_0 giving the reflection coefficient at normal incidence, the second term the reflection coefficient at intermediate angles and the third term describes the reflection coefficient of the critical angle. This change in term is seen where the S-wave velocity V_S, and the change in the S-wave velocity ΔV_S are replaced by Poisson's ratio Υ and change in Poisson's ratio $\Delta\Upsilon$ such that:

$$V_S^2 = V_P^2\frac{1 - 2\sigma}{2(1 - \sigma)} \quad (17)$$

Shuey (1985) led to AVO analysis becoming an economical option in hydrocarbon exploration. The Shuey (1985) approximation includes all relations between the elastic properties of the medium and the reflection coefficient. It can also be expressed in terms of AVO intercept and AVO gradient:

$$R(\theta) \approx R_0 + Gsin^2\theta \tag{18}$$

where R_0 gives the AVO intercept (equivalent to reflectivity at normal incidence) and G is the AVO gradient, these terms can be estimated from seismic data by least squares regression applied to constant time slices of moveout-corrected common reflection point gathers and can be used for interpretation by cross plotting these results. The AVO gradient is directly related Poisson's ratio change, which is related to fluid saturation in reservoir rocks:

$$G = R_0 A_0 + \frac{\Delta\sigma}{(1-\sigma)^2} \tag{19}$$

where $\Delta\sigma$ is the change in Poisson's ratio change across the boundary. The direct calculation of Poisson's ratio change can be calculated for a scaled sum of the AVO gradient and AVO intercept:

$$\Delta\sigma = \frac{4}{9}(G + R_0) \tag{20}$$

Sources of error when calculating the intercept and gradient were discussed by Swan (1991) as a continuation of the findings of Spratt (1987) that AVO analysis is extremely sensitive to small residual velocity errors. Swan (1991) found that amongst other sources of error the NMO stretch was the most serious, with the NMO stretch causing gradient errors.

Smith & Gidlow (1987) formulated their own approximation of the Zoeppritz equations based on Aki & Richards (1980), where they assume the critical angle is not reached due to the small variations in medium properties, and due to this remove the dependency on density such that:

$$R(\theta) \approx \frac{5}{8}\frac{\Delta V_P}{V_P} - \frac{V_S^2}{V_P^2}\left(4\frac{\Delta V_S}{V_S} + \frac{1}{2}\frac{\Delta V_P}{V_P}\right)\sin^2\theta + \frac{1}{2}\frac{\Delta V_P}{V_P}\tan^2\theta \tag{21}$$

This simplification allowed the estimation of rock properties by using a weighted stacking (geo-stack) method, using time- and offset-variant weights to the data samples before stacking.

4.5.1 AVO classification

AVO effects in gas sands were classified by Rutherford & Williams (1989), with three classes identified. AVO response was related to marine gas sands and their encasing shale surroundings. Class I (blue line, Figure 8) (termed 'dim out') gas sands with higher impedance than the encasing shale with relatively large positive values of zero-offset amplitude, further offset amplitudes approaching zero. Class II (red lines, Figure 8) (termed 'phase reversal') gas sands have nearly the same impedance as the encasing shale and are characterised by zero-offset amplitudes values near zero, though at further offsets a significant negative amplitude can be seen. Class III (orange line, Figure 8) (termed 'bright spot') sands have lower impedance than the encasing shale with negative, large magnitude zero-offset amplitude values, with a strengthening negative amplitude at further offsets. Each of these sand classes has a distinct AVO characteristic. A fourth class of AVO response (green dashed line, Figure 8) was defined by Castagna & Swan (1997), where a strong negative zero-offset amplitude shows a positive shift in amplitude, approaching zero at further offsets. These AVO response classifications have become an industry standard.

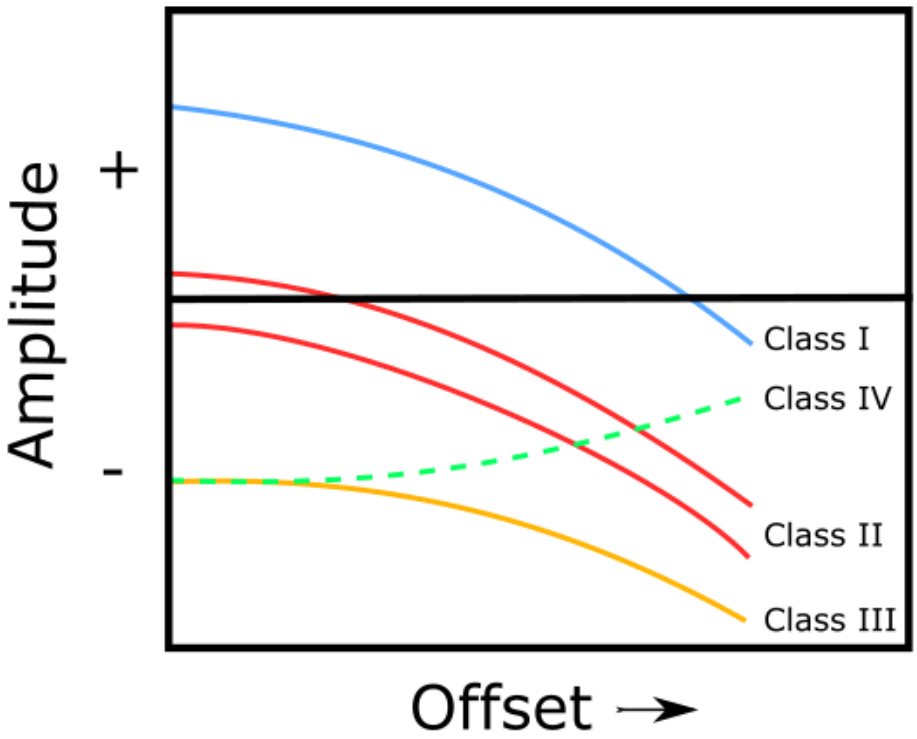

Figure 8 - AVO response classes from Rutherford & Williams (1989) and Castagna & Swan (1997).

Another way of examining AVO response data is by looking at the AVO attributes. These consist of AVO gradient, AVO intercept, and the product of the gradient and intercept known as the AVO product. The AVO gradient is the slope of the least-squares straight line fit for increasing or decreasing AVO response, and the AVO intercept is the X-axis zero intercept of the least-squares straight line fit. Cross-plots of the AVO gradient and AVO intercept can be used for classifying AVO responses (Foster et al., 1993; Castagna & Swan, 1997; Castagna et al., 1998), and for identifying hydrocarbon deposits when performed correctly (Ross & Kinman, 1995; Verm & Hilterman, 1995). Ross (2000) notes that cross-plotting the gradient against the slope can reveal anomalous responses that may be associated with a particular lithology or pore fluid of interest and also that for observed seismic data the cross-plot should be computed using an interpreted horizon rather than a constant time.

Poisson's ratio can be estimated from the AVO cross-plot by taking the slope of the background trend. Castagna & Swan(1997) and Foster et al. (1997) found that the slope of the background trend is determined by the V_P/V_S ratio. Foster et al. (1997) shows that for a V_P/V_S ratio of 2.0, the slope follows the fluid line, and as this value moves away from 2.0 the goodness-to-fit for

the fluid line decreases. Using this V_P/V_S ratio approximation Foster et al. (1997) give to solve Poisson's ratio:

$$\frac{V_P}{V_S} = 1 - 8\sigma^2 \tag{22}$$

The use of AVO cross-plotting is greatly complimented by the use of 3D seismic data along with in-situ well-log data.

4.5.2 AVO studies in hard rock environments

Published AVO analysis in hard rock environments is hard to come by. Bohlen et al. (2003) presented some theoretical consideration of the topic of AVO effect, noting that seismic scattering observed from deep massive sulfide ore deposits in borehole seismic recordings may give rise to a pronounced AVO response. In studying the influence of large inclusion composition on the scattering wavefield, it was seen that the AVO behaviours of P-P waves varied significantly with composition.

One paper available showing the technique in practice is Harrison & Urosevic (2012), who used AVO analysis to target gold deposits in the St. Ives gold camp of Western Australia, finding that seismic reflection surveys in combination with rigorous processing steps and heavy quality control can be used to not only detect first-order structures, but also for more refined lithological analyses. The authors were very strict and complete in their processing, employing a twenty one step processing workflow, in which they carefully considered each parameter with the goal of preserving as much of the amplitude, frequency and phase content as possible. 2D seismic reflection data is less advantageous than a full 3D survey, as true relative amplitude processing is unattainable in 2D seismic reflection. This is due to waveform scattering being experienced in 3D, which cannot be compensated for by 2D processes. In this case Automatic Gain Control (ACG) had to be used to deal with the high ambient noise, the effect of this process does not preserve amplitude content but was lessened by using a very long AGC window for scaling. From the seismic reflection section, the authors interpreted an anticline structure with crustal scale shear zones considered potential contributors to mesothermal gold mineralisation where deep sources of mesothermal fluid have followed the contours of the anticline upwards through the greenstone package. Harrison & Urosevic (2012) also modelled

the AVO response by extracting a statistical wavelet from the seismic data and by computing a synthetic gather using ray tracing and Zoeppritz equations. The authors identified that gold-bearing deposits may be related to an increased reflectivity in the data, and an elevated AVO effect. The anomalies identified in the AVO analysis were thought to be caused by Poisson's ratio changes within a shear zone with respect to the host rock due to differences in mineral composition but could also be from structural variations such as fracturing and alterations. Because of this the authors catalogued the AVO responses from borehole data. Long offset seismic reflection data (~1 km) was found to be beneficial for AVO modelling in hard rock environments. It is important to note that the study area was favourable for this kind of study, and that the potential of AVO analysis is highly site specific.

Considering the results of the AVO analysis suggesting change in Poisson's ratio and shear velocity, the authors performed an elastic inversion of the data. Here the authors compared the elastic impedance (EI) and acoustic impedance (AI) for near and far offset stacks. Of specific importance was the 'cross over zone' between AI and EI high gold content. This does not give a direct indication of gold mineralization but was another parameter used in conjunction with the other interpretations derived in the paper and structural data. Harrison & Urosevic (2012) stress that while 2D seismic data and AVO has much promise, high-resolution 3D seismic will be much more valuable in the future due to the ability to image complex structures and recover true relative amplitudes.

4.6 Seismic Attribute Analysis

Seismic attribute analysis used used to gain detailed geological and structural information from seismic reflection data. There are many seismic attributes which have been defined since their introduction in the 1970's (Taner & Sheriff, 1977; Chopra & Marfurt, 2005) e.g. amplitude, frequency, dip, azimuth, phase. The seismic attributes themselves are defined by Sheriff (1991) as being derived from the seismic data by mathematical manipulation of the seismic wave components.

Chopra & Marfurt (2005) present a thorough history of seismic attributes within the hydrocarbon industry, stating the first use of attribute analysis in seismic reflection studies could be attributed to Rummerfield (1954). This paper looked at the changes in the quality of

deeper reflecting horizons in relation to a shallower 'control' horizon. Narrowing down the use of seismic record to single trace studies of reflection quality to further study the physical properties of a reflecting horizon in the seismic data was a new approach in the search for oil in North America. Attributes such as dip, thickness and discontinuities could be studied on analog data. When digital data recording came to the fore, these attributes could really be utilised (Chopra & Marfurt, 2005). A major step forward in seismic attribute analysis came with the discovery and development of bright spot technology, where sections of strong isolated reflections and changes in the character of these reflections in seismic sections were investigated. When drilling of some of these events began to encounter gas zones, 'bright spots' were christened and became a major interpretation tool in hydrocarbon exploration (Hammond, 1974; White, 1977; Wood & Treitel, 1975). The analysis of amplitudes and all attribute analysis were greatly helped by Balch (1971) who was the first to display seismic data using colour, this breakthrough was a major step forward allowing much better visualisation and interpretation of seismic data. This allowed for Anstey (1973) to use colour as a means to produce seismic attributes in their geological context at the same time.

The energy crisis of the 1970's drove the development and use of seismic attributes onwards with Taner & Sheriff (1977) and Taner et al. (1979) showing that amplitude, frequency and phase could all be used in stratigraphic investigation and hydrocarbon detection. The 1980's saw the development of response (wavelet) attributes (Bodine 1984, 1986; Robertson & Fisher, 1988), and textural attributes (Love & Simaan, 1984). In the 1980's 2D attributes that used continuity and dip were developed to analyse seismic facies (Conticini, 1984; Vossler,1988), and horizon/interval attributes also began to show promise due to the continued improvements in recording and processing techniques. 3D attribute analysis was available come the mid-90's due to the price of 3D surveys falling considerably since their introduction in the 1980's, with this many new and improved attribute fields emerged such as seismic coherence (Marfurt et al, 1998, 1999; Gersztenkorn & Marfurt, 1999), spectral decomposition (Partyka et al. 1999, Peyton et al., 1998), curvature (Roberts, 2001; Hart et al., 2002; Chopra & Marfurt, 2007) and the cross-plotting of attributes to reveal common lithologies and fluid types (White, 1991; Chopra et al., 2003). The future of attribute analyses may be seen in neural networks that can be trained with a suite of stratigraphic and depositional structures to automatically detect such patterns in seismic data.

Instantaneous attributes (post-stack) are some on the most commonly used in seismic studies (White 1991; Barnes, 1991, 1992). This category of seismic attribute describes a response at each signal point. These attributes are used to concisely and quantitatively investigate the seismic waveform, leading to enhancing the detection of reflector's extent and resolution. As they describe the shape of the waveform, they are useful in aiding seismic interpretation. A complex seismic trace with a real trace component and an imaginary trace component can be expressed as:

$$g(t) = x(t) + iy(t) \tag{23}$$

where *g(t)* is the seismic trace, *x(t)* is the real trace component and *iy(t)* is the imaginary trace component. Here, *y(t)* is derived from *x(t)* using the Hilbert Transform (*H(xt)*) as defined by Taner & Sheriff (1977). This shifts the seismic trace *x(t)* by 90°, so that *y(t) = H(x(t))*. The Hilbert transform of the seismic signal used to calculate the instantaneous attributes can be used as an attribute itself.

From Equation 23, instantaneous amplitude (also known as amplitude envelope) can be calculated as:

$$A(t) = \sqrt{x^2(t) + y^2(t)} \tag{24}$$

Instantaneous amplitude is a phase independent vector that measures seismic impedance, the product of density and seismic velocity. The first derivative of the envelope can also be taken, this will indicate the presence of sharp interfaces. Also, from this calculation you can get the relative impedance, which will show the band-limited apparent acoustic impedance contrast.

Furthermore, from equations 23 and 24 the instantaneous phase, *θ(t)*, can be defined as:

$$\theta(t) = \tan^{-1}\frac{y(t)}{x(t)} \tag{25}$$

The phase is measured from -180° to +180° as described by Sheriff & Geldart (1995). This attribute will help to define the continuity of thin and weak seismic events that might otherwise be overlooked.

A complimentary attribute to instantaneous phase is paraphase, $\beta(t)$, which can be calculated from Equation 25 as:

$$\beta(t) = \cos\big(\theta(t)\big) \tag{26}$$

Paraphase contains no representation of amplitude, just the full 180° rotation of phase for each reflection event. As no amplitude information is presented with paraphase, all events are represented in a value range from 0 to 1, so this attribute can help with enhancing continuity of events. Paraphase is mainly used to investigate thin boundaries (Manzi et al., 2013). What defines paraphase is its much smoother representation compared to instantaneous phase as it avoids +/- 180° discontinuity.

Instantaneous frequency, $\omega(t)$, is the first derivative of instantaneous phase, expressed as:

$$\omega(t) = \frac{d\theta(t)}{dt} \tag{27}$$

The instantaneous frequency measures the change of instantaneous phase, how the wavelet goes from peak to trough. As it is independent of phase and amplitude, it is used to investigate lateral changes in lithological boundaries (Manzi et al., 2013). The instantaneous weighted frequency is weighted by the instantaneous amplitude (envelope). It is a smoothed instantaneous frequency attribute and is less sensitive to abrupt variations of the signal in comparison to the normal instantaneous frequency.

Geometric attributes differ from instantaneous attributes in that they reveal structural aspects of the subsurface. The dip attribute shows how much a seismic reflector deviates from horizontal and is defined as the angle between the steepest dip of the plane and the horizontal. Reflector dip was first utilised by Picou and Utzman (1962) who cross correlated dips on 2D seismic lines to estimate the dip angle at every sample and trace on the seismic section. This attribute can be used to detect areas effected by faulting and fracturing due to the increased detected dip of the fractured and faulted medium.

Mazzotti (1991) has looked at instantaneous attributes vs. offset, stating that variations with offset of amplitude, phase and frequency provides a better understanding of the reflection phenomena and yields further indications of the nature of subsurface target. By using synthetic data that tested a variety of velocity and thickness values Mazzotti et al. (1991) came up with a range of indicators that they tested against real seismic data. In the synthetic data amplitude and phase variations with offset resulted from critical angle phenomena and interferences. The frequency indicator was mainly dominated by wavelet spectrum and some interference. With real data critical angle phenomena and interference effects were detected. For gas-saturated sand layers an increasing amplitude along with a near constant phase was seen in the synthetic data, and good correlation was seen when comparing this response to real data.

4.6.1 Attribute Analysis in hard rock studies

Attribute analysis has been used in hard rock seismic exploration sine the 90's and early 00's (Cocker et al., 1997; Hatherly et al., 1998; Stuart et al., 2000) and has become increasingly popular in recent years (Hossain et al. 2015; Mejia-Herrera et al., 2015; Jingbin et al., 2015; Gibson et al., 2015; Manzi et al., 2020). Manzi et al. (2012a) utilised 30 years' worth of 3D seismic data over the Witwatersrand Gold mine to identify drilling targets. Dip and azimuth horizon-based seismic attributes were used to enhance structural interpretation, these attributes measure the magnitude and direction of the gradient vector. These attributes were successful in enhancing structural continuity and detecting the crosscutting or conjugate relationships of faults. Manzi et al. (2012b) used edge detection attributes that combined dip and azimuth variations in a hazard assessment study to delineate fluid conduits that may provide transport for inrushing groundwater or flammable gases in the Witwatersrand gold mines. The seismic attribute study aided in characterizing fault continuity and connectivity in relation to faults and dikes of varying orientation and throw that propagate between the Ventersdorp Contact Reef (VCR) and the Black Reef (BLR) formations. Manzi et al (2013) used a comprehensive range of seismic attributes to enhance the detection of the Elsburg Conglomerate (EC) reef in the South Deep gold mine in Witwatersrand. These attributes include reflection strength, average energy (square of RMS amplitude), instantaneous frequency, phase, and paraphase. Phase and paraphase proved the most valuable attributes in detecting the EC sub-crop position, which could then be factored into the current mine model to improve resource evaluation.

5 Data

5.1 Seismic data

The seismic data used in this project was collected as part of the project HIRE (High Resolution Reflection Seismics for Ore Exploration 2007-2010) by the Geological Survey of Finland (GTK), University of Helsinki and University of Oulu in cooperation with Northland Exploration Finland Oy (Kukkonen et al., 2009). A 2D seismic-reflection survey comprising of six Vibroseis lines (71.7 km) and two explosive seismic lines (8.7 km) was performed (Figure 9). This work focuses on profiles E1 and V5 due to their proximity to the Hannukainen mine site. The crossover point of profiles E1 and V5 is located by the old open pit mining sites of the Laurinoja and Kuervaara ore bodies.

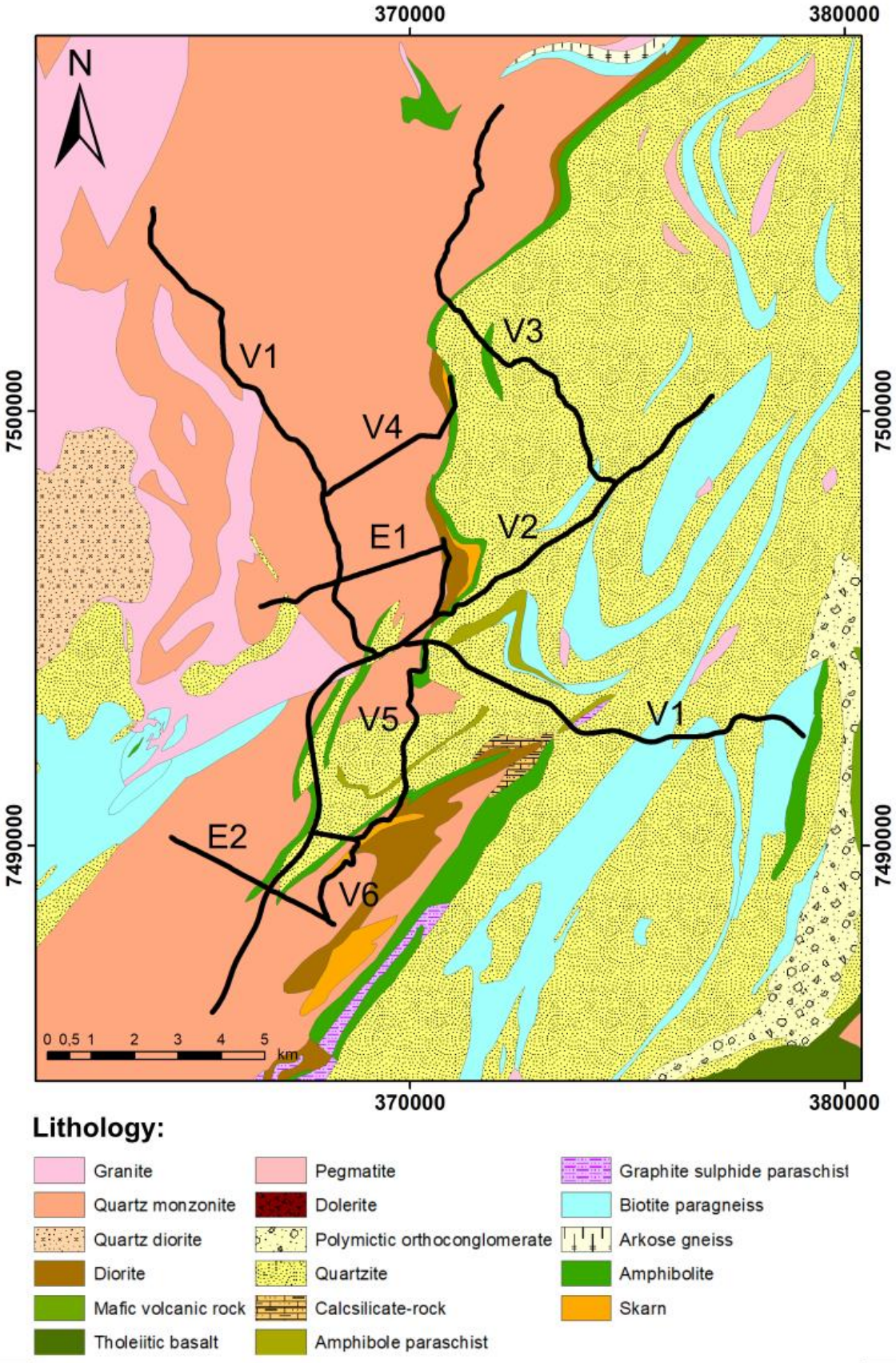

Figure 9 - Location of all HIRE project seismic profiles. Coordinates are in the EUREF-FIN ETRS-TM35FIN system. Lithology data: Bedrock of Finland 1:200 000 © Geological Survey of Finland 2016.

Profile E1 is not perfectly straight, with a small kink near the southern end. This is due to the terrain conditions at the time of acquisition. The number of active receiver channels per shot was 402, with spacing of 12.5 m. Source point spacing was 50 m with a reduced spacing of 25 m in the locale of known deposits. Dynamite was used as a detonation source, with shot size of 125 or 250 g. Shot holes of 2.5 m depth were drilled into the Quaternary soils and cased within plastic tubing. The shot holes were filled with water before shooting to maximize transmission of seismic energy into the ground. The shots and receivers were positioned with differential GPS to an accuracy of at minimum ± 2 m. Elevation was determined by levelling to an accuracy of at least ± 0.5 m. The survey parameters have been listed in Table 3.

Profile V5 is a crooked-line Vibroseis profile. There are major deviations in V5's geometry, due to cultural and topographical issues during data acquisition. The number of active receiver channels per shot was 402, with spacing of 12.5 m. Three (minimum two) 15.4 ton Geosvip vibrators were grouped together for the source. These applied a force of approximately 10 ton/vibrator. The sweep was 16 s linear upsweep with a 30-165 Hz frequency band, and a total listening time of 22 seconds. The final correlated signal length was 6 seconds, with six sweeps per source point.

Table 3 - Survey parameters for Hannukainen profiles E1 and V5.

Parameter	**E1**	**V5**
Recording	I/O-4	I/O-4
No. of active channels	402	402
Sampling interval (ms)	1	1
Recording length after correlation (s)	6	6
Preliminary gain (dB)	24÷36	24÷36
Notch filter (Hz)	Off	
Noise suppression editor (BURST and DIVERITY)	On	On
High-pass filter (Hz)	Off	30
Tape format	SEG-Y	SEG-Y
Medium type	HARD	HARD
Acquisition geometry	Symmetrical split spread	Symmetrical split spread
Stacking fold	Varying	Varying
Receiver group spacing (m)	12.5	12.5
Profile length (km)	9.900	4.450
Spacing of source locations (m)	25 or 50	50
Spread length	5012.5	5012.5
Linear geophone grouping	6 geophones on 12.5 m base	6 geophones at a point or 3 swamp geophones at a point
Linear SV-14-150 vibrator grouping	3 on 25 m base	
Sweep frequency limits (Hz)	30÷165	
Sweep period (s)	16	
Number of vibrations at a source point	6	
Shot hole number at a source point		1
Shot hole depth (m)		2.5
Charge weight (g)		125 or 250
Ground force	65%	
Control system and vibrator synchronisation control	VIB PRO	Shot PRO

Kukkonen et al. (2009) interpreted an upper 5 km of strong, high-amplitude reflectors that can be correlated to a lateral extent of up to 20 km. At profile E1 (Figure 10), as three-layer reflector system is seen ranging from 200 m to about 1 km in thickness. This large-scale structure is interpreted as thrusting from southwest to northeast, related to the Kolari Shear Zone. The reflectors imaged in the Hannukainen area were correlated with known deposits, resulting from

the presence of iron stone, skarn and amphibolite within the monzonite, diorite and metasediments.

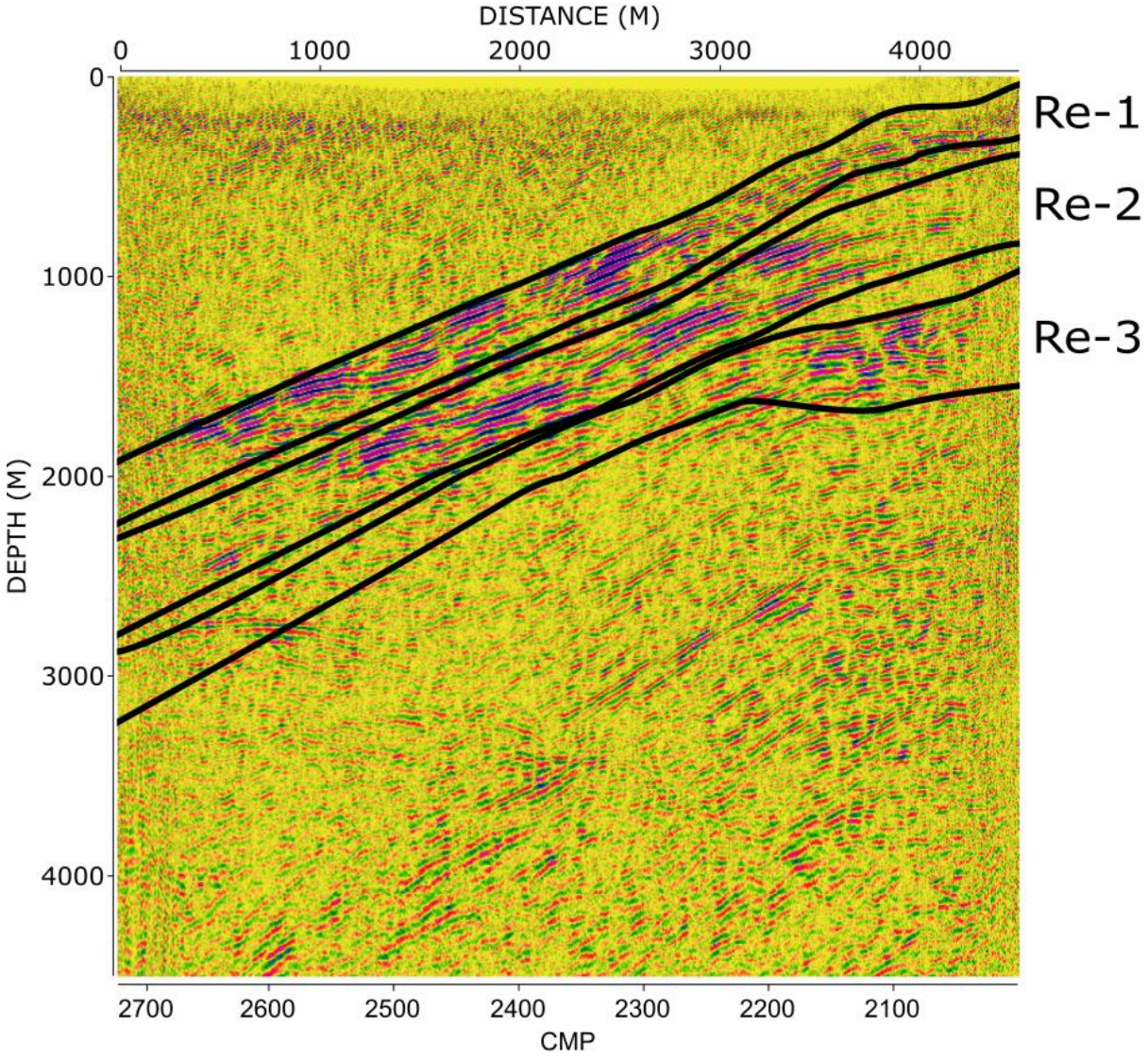

Figure 10 - E1 final section from Kukkonen et al. (2009) with the interpreted three-layer reflection package.

The uppermost layer, Re-1, in the thee-layer reflector system coincides with the Kuervaara and Laurinoja deposits in the Hannukainen area. Kukkonen et al. (2009) put forward the geological interpretation of reflectors Re-1, Re-2 and Re-3 as a system of interlayered mafic metavolcanic and metasedimentary rocks featuring local layers of altered rocks, such as skarn, ironstone and sulphides, stating that shearing should also be considered as an alternative interpretation due to the close connection of the structures with thrusting along the Kolari Shear Zone. Some correlation with geological logging from drill hole data (Hiltunen, 1980) was done, with the upper part of reflector Re-1 correlating with skarn and iron stone layers, the drill hole does not

go deep enough to reach Re-2 and Re-3, but it is noted that they show increased amplitude compared to the Re-1. Other geophysical data was also correlated with reflector Re-1. Deep EM soundings by Gyurko et al. (1983) trace the uppermost magnetite horizon to a depth of about 600 m which corresponds with the uppermost wavelets of Re-1. AMT soundings completed by Pietilä & Hattula (1982) imply at least 2 clear horizons in the Hannukainen area, though noise due to the level of technology at the time hinders the reliability of this data. Magnetic modelling also by Pietilä & Hattula (1982) is in agreeance with the AMT data, implying magnetic layers beneath Re-1. These geophysical data imply that the reflector Re-1 is only partially mineralised, with conductive and magnetic layers at about 200-250 m vertical intervals, this could indicate barren skarn layers which are not mineralised but are reflective nonetheless (Kukkonen, 2009). The deeper reflectors, Re-2 and Re-3, show similarly reflectivity but do not have the same level of mineral evidence as Re-1, though they may be of similar composition.

The interpretation of profile V5 as per Kukkonen et al (2009) shows the same three-layer package of reflectors seen in profile E1, extending to the south, in the north of the section and also another three-layer package of reflectors from the Rautuvaara area (Ra-1 to Ra-3). These reflector packages are separated by the Äkäsjoki Thrust Plane (Figure 11).

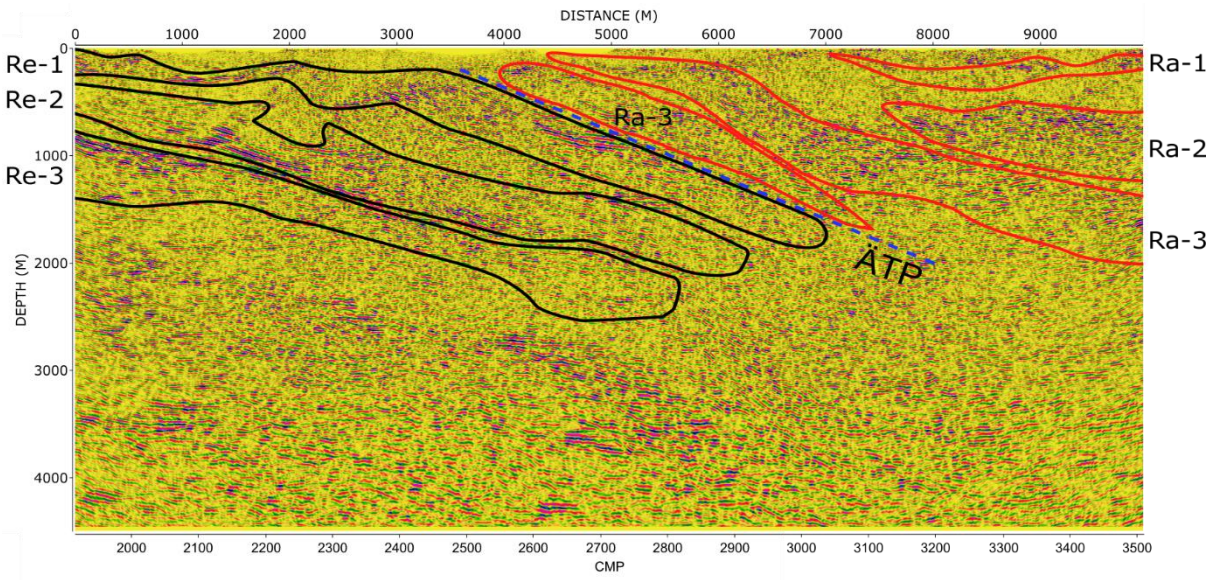

Figure 11 - V5 final section from Kukkonen et al. (2009) with the interpreted three-layer reflection package Re-1 to Re-3 (outlined in black) in the Hannukainen area, and Ra-1 to Ra-3 (outlined in red) in the Rautuvaara area. ÄTP is the Äkäsjoki Thrust Plane (blue dashed line) that is interpreted to separate the Hannukainen and Rautuvaara packages.

From the drilling data of Hiltunen (1982) the shallow reflectors of the Rautuvaara three-layer structure coincide with magnetite ore, skarn rock and amphibolite, the same as they do in profile E1. Further geological interpretation was completed by Niiranen et al. (2014) by 3D modelling he Kolari region and incorporating the HIRE project seismic profiles, in particular profile E1. A three-layer system similar to Kukkonen et al. (2009) is interpreted (A, B and C, in place of Re-1, Re-2 and Re-3), though not beyond 2000 m depth due to the uncertainty of the reflectors at this depth. This study is mainly concerned with tectonic evolution of the wider area. The reflective layers are interpreted such that the top layer (A) is said to correlate with Rautuvaara Formation mafic volcanic rocks, and the middle layer (B) is said to correlate with Sodankylä Group quartzites.

5.2 Borehole data

A large database of borehole data as made available by Hannukainen Mining Oy for the Hannukainen region, and from this database the most relevant boreholes to profiles E1 and V5 were selected (Figure 12). The depth of these boreholes is largely shallow (up to 350 m), so some deeper boreholes (up to 550 m) located up to 300 m offset from the seismic profiles were selected to provide information of the deeper structure. These boreholes are for E1; HAN07042, HAN07197, HN11GT05, HAN11005, HAN11004, HAN07030, HAN11013, CON1123, HAN07039, and for V5; HAN06013, HAN08026, HAN11008, HAN08028, HAN11009, HAN12001 (Figure 12). The depths the of these boreholes range from most shallow borehole HAN06013, which is 191 m deep, to the deepest borehole HAN07039, which is 551 m deep.

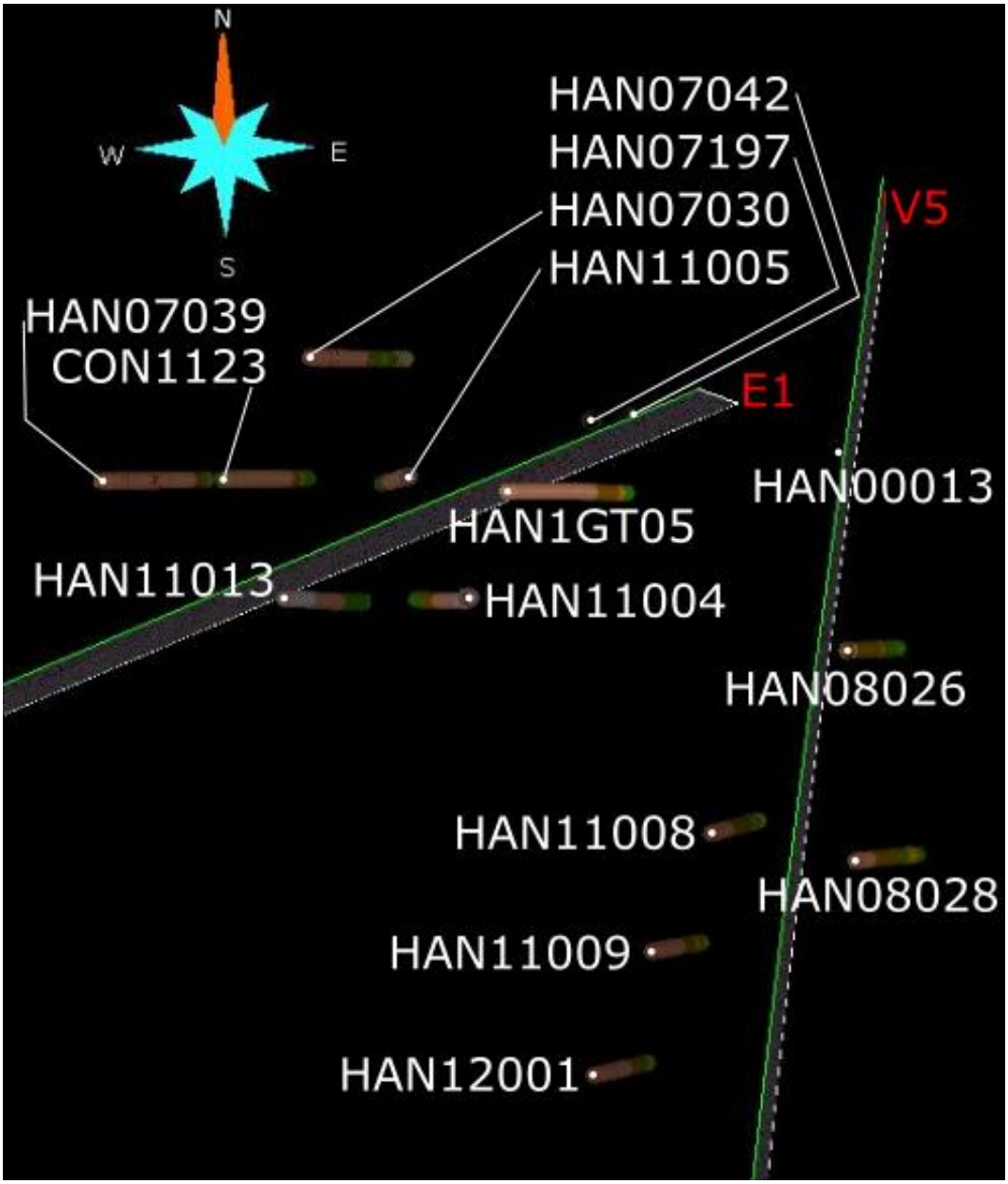

Figure 12 - 3D view of seismic profiles E1 and V5 with selected boreholes from the area. The top of each borehole is marked with a white dot

Borehole data that is available from these selected boreholes includes the major and minor lithological units, mineralisation minerals, alteration type and intensity, and RQD, the degree of fracturing within the rock. In this study these properties and their relationship with the seismic data will be analysed, but the depth extent and sparsity of the boreholes does not allow to for detailed interpretations.

6 Data Processing & Results

Explosive profile E1 and Vibroseis profile V5 were processed using GLOBE Claritas software,. The processing flow was designed for the uppermost 1500 ms of the seismic data. This ‘depth’ in two-way travel time corresponds to approximately 4500 m with an average seismic velocity of 6000 m/s. Examples of the processing steps will be shown mostly for profile E1 which is the main focus of this study. Profile V5 is used as a supplementary profile to show the continuation of the reflectors. Another reason for profile E1 being the main focus is that the quality of the seismic data is much better than that of profile V5 due because E1 is an explosive profile and has more linear survey geometry. The first arrivals of the profile E1 explosive data are much clearer that of the profile V5 Vibroseis data.

6.1 Target-specific processing workflow

6.1.1 Profile E1

The processing flow for the explosive data of profile E1 is shown in Table 4.

Table 4 - Pre- and post-stack processing for explosive profile E1.

Pre-stack processing:
1. Assign CDP geometry. CDP spacing 6.25 m. Perpendicular CDP bin size 100 m.
2. First break picking. Maximum offset 800 m.
3. Refraction static corrections through inversion of first break picks. Two-layer model with varying velocity. Floating datum level of 220 m above sea level with replacement velocity 5500 m/s.
4. Geometrical spreading correction. Power value 1.3. Time-velocity pairs: 0 ms -5300 m/s, 6000 ms-6500 m/s
5. Airwave attenuation. Velocity 330 m/s.
6. S-wave attenuation. Velocity 2700 m/s.
7. Muting of noisy traces.
8. Trace amplitude balancing.
9. Band-pass filtering. Corner frequencies 30-40-200-240 Hz.
10. Predicative deconvolution. Filter length 100 ms, gap length 5 ms, white noise percentage 0.1, Hanning window applied.
11. Band-pass filtering. Corner frequencies 30-40-200-240 Hz.
12. Trace amplitude balancing.
13. Sort to CDP domain.
14. Surface-consistent residual static corrections.
15. Velocity analysis, constant velocity panels.
16. NMO corrections. Stretch mute percentage 50.
17. Stacking. Stack mode = Median.
Post-stack processing:
18. Final datum correction to seismic reference datum (SRD)
19. Kirchhoff Migration. Constant velocity 6000 m/s.
20. FX-domain complex Wiener deconvolution. Filter length 19 traces. Number of traces to filter at a time, 19 traces with 6 trace overlap. Time window size 100 ms with 25 ms overlap.
21. Horizontal trace amplitude balancing with constant time windows of 150 ms with a 50 ms overlap. Alternatively, for imaging purposes only an AGC window of 200 ms is applied.
22. Band-pass filtering. Corner frequencies 30-40-200-240 Hz
23. Semblance coherency filtering.
24. Trace amplitude balancing.
25. Time to depth conversion using NMO velocity function

6.1.1.1 CMP geometry and static corrections

Choosing of the 2D CMP profile geometry is a critical step as amplitude focusing and change due to geometry will be a factor that affects how the subsurface reflection points will be represented in the seismic section. If the survey profile is completely straight and the reflectors horizontal then this does not matter as the source-receiver midpoints coincide with the survey line, and the CMP profile can be chosen unequivocally. However, in the case of a 'crooked-line survey' the source-receiver midpoints create a cloud of source-receiver midpoints, and the CMP profile geometry is always a compromise that projects these points onto a profile. For profile E1, different versions with different CMP geometries were tested to investigate the dependency of the observed reflectivity patterns on the geometry. These tests will be shown together with the final 'best' section. Figure 13 shows the final CMP profile (red line) projected on the top of the survey profile (blue line), along with the midpoint cloud (yellow area) which shows all midpoints of the source/receiver pairs. The max fold for the CMP profile is 84.

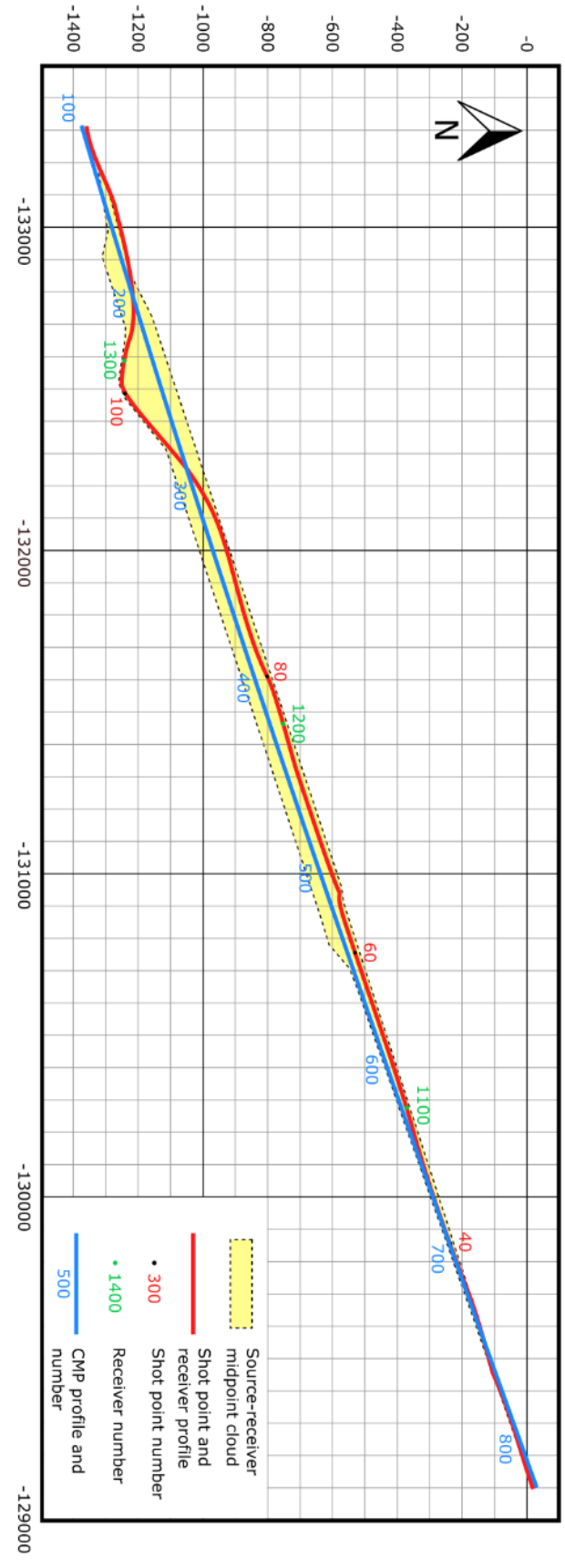

Figure 13 - CMP geometry selected for profile E1 (blue line) shown with the source/receiver profile (red line), and source-receiver midpoint cloud (yellow area).

Static corrections in seismic reflection processing are done to correct for the variable topography, and variable thickness and velocity of the overburden layer. This process will result in seeing how the reflection arrival times would be if they had been recorded on an ideal plane with no topographic variation or low-velocity overburden layer (Figure 14).

Refraction statics (sometimes termed first-break statics) are the most common form of static corrections and involve the picking of the onset arrivals of refracted signals on the seismic trace. The differences in first arrival travel-times between adjacent records are used to calculate the depth and velocity of near-surface overburden layers (Lawton, 1989). In the processing sequence used in this study, the overburden layer is first replaced with bedrock and the data is corrected to their true elevation level; then the floating datum statics are used to move the data to a datum smoothly following the topography (Figure 14). Finally, in the stacking stage, the data are moved to the final, flat datum level.

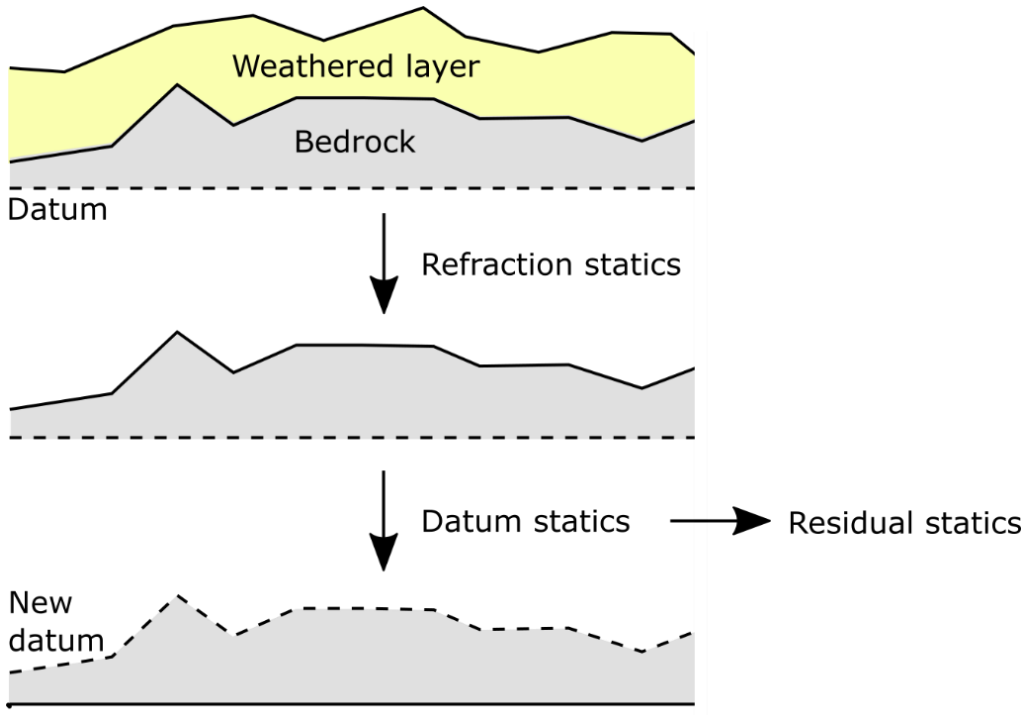

Figure 14 - Procedure for static corrections, first removing the effect of the weathered layer and then reducing the data do a fixed datum. Residual statics is dealt with in the stacking phase.

The onsets of the first arrivals were picked within an offset range of 0-800 m for the calculation of the surface consistent refraction statics. Refraction static were vital as in the area of the profile E1 there is considerable overburden thickness which varies in the tens of metres across the profile. A two-layer model of varying velocity was calculated and gave a root mean square

(RMS) error value of 3.14 (Figure 15). The resulting model has an overburden velocity of ~1150 m/s throughout the model. The bedrock velocities range between ~4500 m/s and ~5400 m/s throughout the model with the same decrease in velocity seen in the north of the profile. The resulting refraction statics varied from 0 to 25 ms. A replacement velocity of 5500 m/s was used for both the refraction statics and the floating and final datum statics. Later in the processing flow the residual static corrections were applied to account for any remaining effects of the overburden layer. The residual statics processing step calculates CDP-derived, surface-consistent via cross-correlation of pre-stack traces with a pilot CDP stack formed as a trace mixed sum of a programme-created initial model. The model sections have a frequency domain deconvolution applied to them to improve signal-to-noise ratio. The final statics were calculated using NMO corrected data over a time window of 200 ms to 1500 ms and using the tenth iteration.

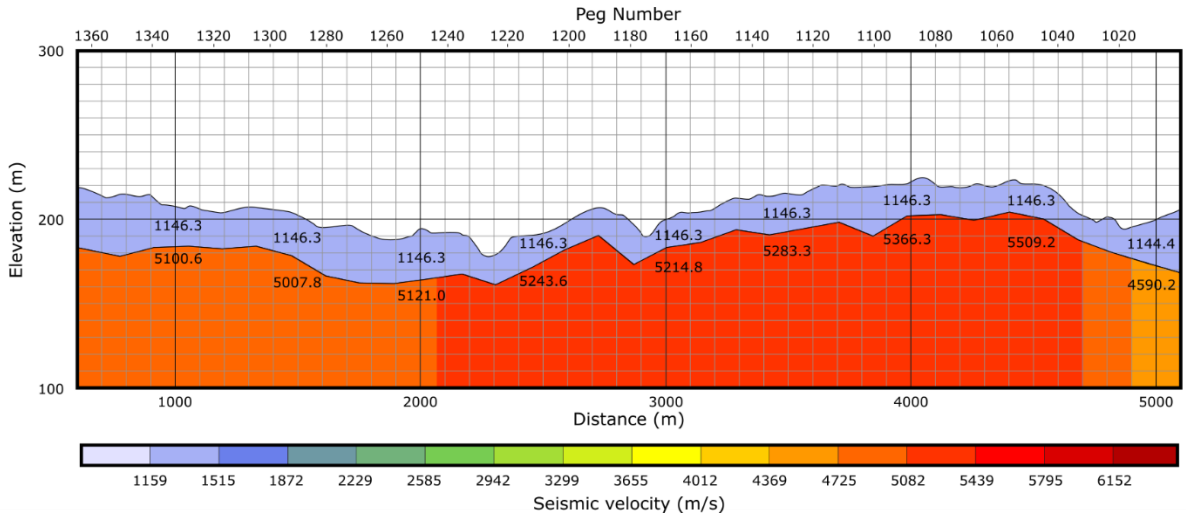

Figure 15 - Calculated two-layer velocity model used for the refraction statics corrections of profile E1.

6.1.1.2 Amplitude corrections, muting, frequency filtering and deconvolution

Next, corrections for the geometrical spreading of the seismic signal in the subsurface and for attenuation due to energy dissipation are made. A scalar function *G(t)* is defined to solve this:

$$G(t) = (V(t) * Vpower) * T^{Tpower} * \exp^{V(t)*t*A} * X^{Xpower} \quad (28)$$

where *V(t)* is the velocity, *Vpower* is the power value of the average velocity at *T* (two-way time), *Tpower* is the power value of the two-way time used in calculating the spherical

divergence, *Xpower* is the power value of offset used in calculating the trace-by-trace scalar and *A* is the power of exponential term. For a varying velocity *V(t)*, the geometrical spreading is proportional to the time multiplied by the RMS velocity at that time. A *Tpower* value of 1.2 is used as it was found to suit the hard rock environment better than the 1.0 default value. Time velocity pairs as listed in Table 2 were also defined to typify the subsurface properties.

Trace balancing is applied to the data with scaling by absolute amplitude using a single fixed time window. A scalar is derived from the average amplitude of the trace within the chosen window, and all trace values are then divided by this scalar so that the average value of the amplitudes becomes 1.0. Another more robust way to balance the horizontal amplitudes is by the use of the surface-consistent trace balancing. The root mean square power of the input traces is calculated, solving the average shot and receiver amplitudes. These amplitudes are stored in a text file that can then be applied to the data to balance the traces. It was noted there wasn't much difference between these trace balancing methods on the final processed seismic section, and the first trace balancing method was applied. Trace balancing is applied at each processing step seen in Figure 16.

Noise in the data is generated in the recording phase by wind, instrument effects, cultural effects and surface waves. This noise can typically be at least partially removed by band-pass filtering in the frequency domain. Band-pass filtering is designed to remove unwanted frequencies and to leave the desired seismic band frequencies where the information desired to be displayed is located. However, when filtering out noise you may also lose some of the wanted seismic signal, this is why the parameters of the frequency filter must be heavily tested. This is especially important in this study for attribute analysis which depends on the true frequency content of the data. After testing the frequency filter was designed to have corner frequencies of 30-40-200-240 Hz. These were decided to best represent the frequencies that represented the true signal of the data, filtering out the low and high frequency noise while keeping enough of the high frequency content of the data. When designing the band-pass filter, a taper must be defined so as to avoid unwanted edge effects that can occur with filters with 'sharp' edges. The effect of band pass filtering can be easily seen in the frequency spectrum of the data is seen in Figure 16B. Band-pass filtering can be applied multiple times, using the same filter, as some processing steps may introduce a level of low or high frequency noise.

The air waves and S-waves were attenuated. A noticeable airwave in the data with a velocity of 320 m/s can be seen in Figure 16B. The region of the wave to be attenuated is defined by a length of zero samples and taper length in ms. For attenuating two AGCs were used, a long one and a short one in such a way that the amplitudes around the airwave will be reduced to the same amplitudes as the surrounding traces, leaving the rest of the trace unaltered. This process was also used to attenuate the S-waves travelling at approximately 2700 m/)s (Figure 16B. The use of muting in the place of attenuation was tested, but in the final stacks a 'shadow' could be seen imprinted in the background of the seismic section, so attenuation was chosen as the better option.

Surgical muting is applied to mute amplitudes in a certain range, in this study it is used to mute very high amplitudes resulting from noisy traces. This involves setting the low and high pass value for the amplitudes you wish to mute (0-100000) and a time window to apply them on (25 ms - 50 ms). The final muting removed mainly near source traces, but also other noisy traces in the record (Figure 16C). This could be similarly accomplished by killing traces when the process of first break picking is being completed. Using surgical muting allows a more consistent removal of noisy traces based on a real attribute rather than the tedious manner of removing them by how noisy they appear in each gather.

Deconvolution is performed on the amplitude-corrected data using a surface-consistent deconvolution filter which is designed on the average auto-correlation function for each shot. From the shot data it is seen that the velocity is consistent throughout the gather, a filter is designed for the whole length of each shot just specifying a start and finish, if there were some noticeable velocity differences along the gather you would specify more values to accommodate these. Testing was done using spiking deconvolution and predictive deconvolution with best results seen using predictive deconvolution with an operator length of 100 ms, gap length of 5 ms and a 0.1% white noise addition. After deconvolution the same band-pass filter as previous was applied to filter out noise created in the deconvolution process. In Figure 16D, the frequency spectrum for the deconvolution step shows that this process boosts the high frequency content of the data.

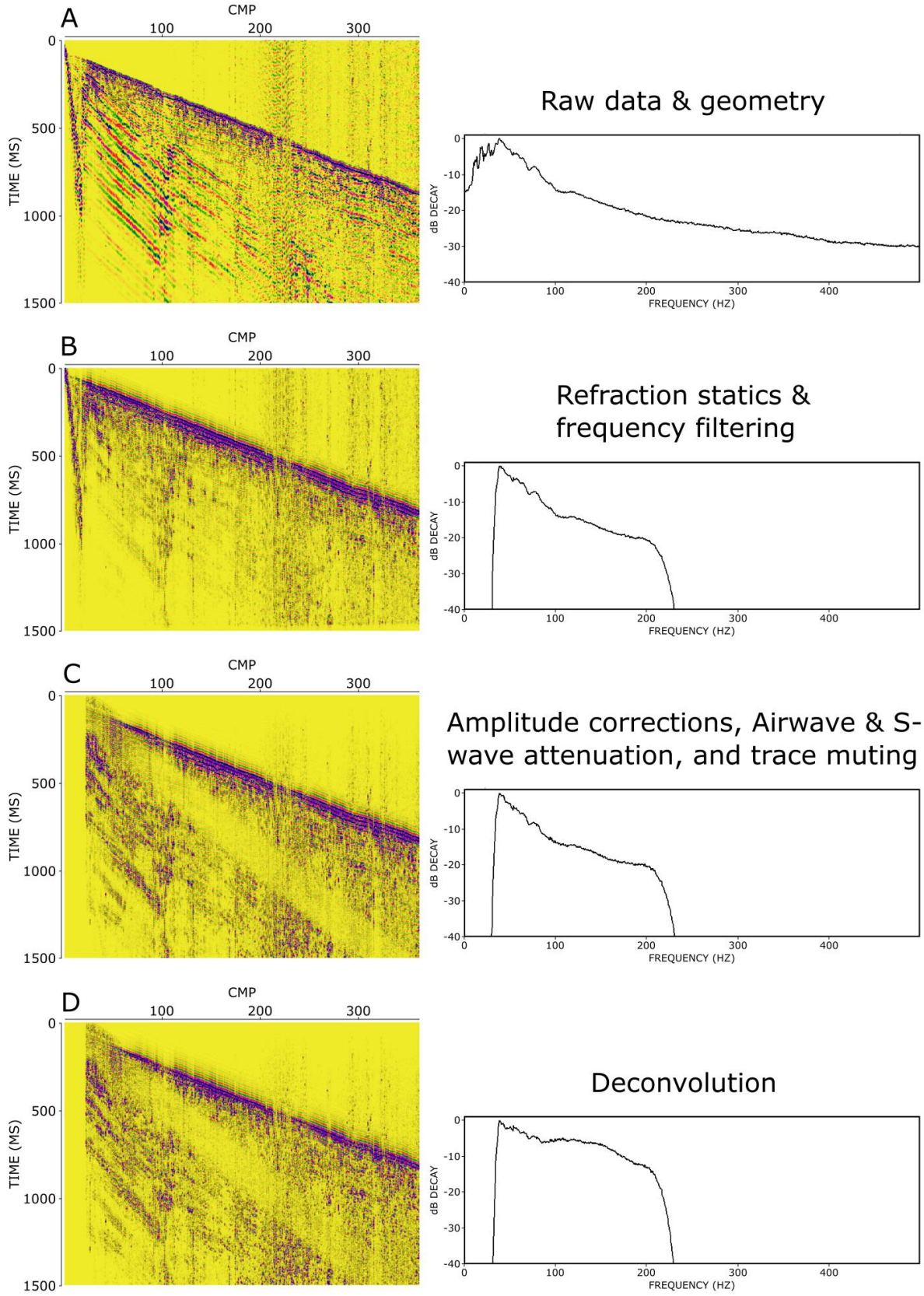

Figure 16 - Effect of the workflow progression on the shot gather and frequency spectrum of 1500 ms of the data from SHOT 70. A - Raw data with geometry applied. B - Refraction statics and frequency filtering applied. C - Amplitude corrections, airwave removed, S-wave suppressed, and trace muting applied. D - Deconvolution applied.

6.1.1.3 NMO corrections, stacking and migration

The normal moveout (NMO) filter is designed by analysing constant velocity stacks of the data and selecting the velocity which brings out the reflection signals in the data best. The velocities for profile E1 vary between 5500 and 6400 m/s. The NMO stretch was well tested in accordance with Swan (1991) who found it to be the main source of error in processing when it comes to AVO analysis, a stretch of 50% was deemed best. Stacking of the data sums the NMO-corrected seismic traces from CMP ensembles and outputs a single trace for each ensemble. In testing various stack modes, a horizontal median stack was found to give the best resulting image. Migrating the data involves the geometrical relocation of seismic events to the position where they actually occur in the subsurface. In an unmigrated section, the events appear vertically right beneath the CMP that contained them, when the dipping reflections actually have the shortest path to the receiver up dip from the vertical travel path. This processing step will create a more accurate representation of the subsurface. Diffracted signals will be collapsed, resulting in increased spatial resolution of the seismic reflection data. The most common form of migration is post-stack Kirchhoff migration. This was used with a constant velocity of 6000 m/s to migrate the data. When testing different migration velocities, the appearance of smile artefacts will note if the velocity is too high and inverse smiles if too low. Alternatively, FK-domain Stolt migration or finite-difference migration could be used. Pre-stack migration is also an option, but these require a highly detailed velocity model, and as a result was not used. Figure 17 shows the stacked data from profile E1, some structures are apparent, but these can be greatly enhanced by the application of post-stack processing.

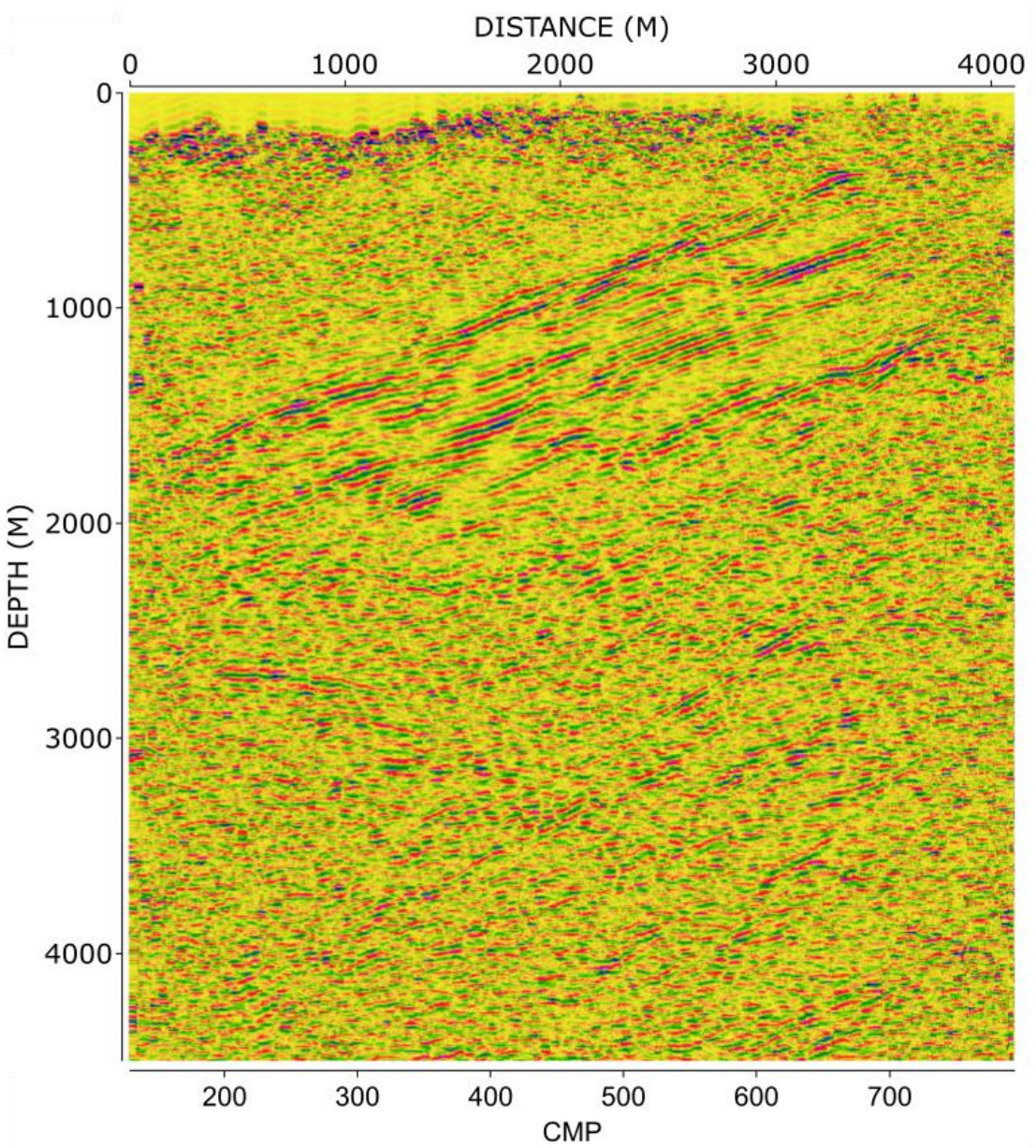

Figure 17 - E1 seismic section with no post-stack processing steps applied.

After stacking, many other processing tools can be used to improve the appearance of the stacked traces, for Hannukainen profile E1 these further post-stack processing steps consisted of:

1. Frequency domain post-stack deconvolution used to attenuate random noise. Each trace is transformed into frequency domain, so the section is in FX domain. A complex Wiener deconvolution is performed in the X direction for each frequency. The filtered section is then transformed back into the time domain and the noise component discarded.
2. Horizontal trace balancing.

3. Automatic gain control applied for display purposes (time window 300 ms). AGC is a non-linear operator, it destroys relative amplitude information and alters the frequency content, so for the following AVO and attribute analyses a trace balancing filter was designed to avoid this.
4. Band-pass filtering with corner frequencies of 30-40-200-240 Hz.
5. Coherency filtering used to identify and isolate coherent events in the noisy background of the seismic data and enhance the visibility of these events. The fundamental approach used by this process is to compute semblances over a lateral window of traces, then compute coherency from these semblances. Smoothing of the data in the direction of maximum semblance is performed and finally the smoothed data is filtered using the coherency.

After the application of the post-stack processing steps, a time-to-depth conversion is applied to transform the data from the time domain into the space domain. This is done using velocities used for NMO correction to give v(t) function information. By running the stacking, migration, post-stacking processes and time-to-depth conversion, the migrated section is generated for Hannukainen profile E1 (Figure 18).

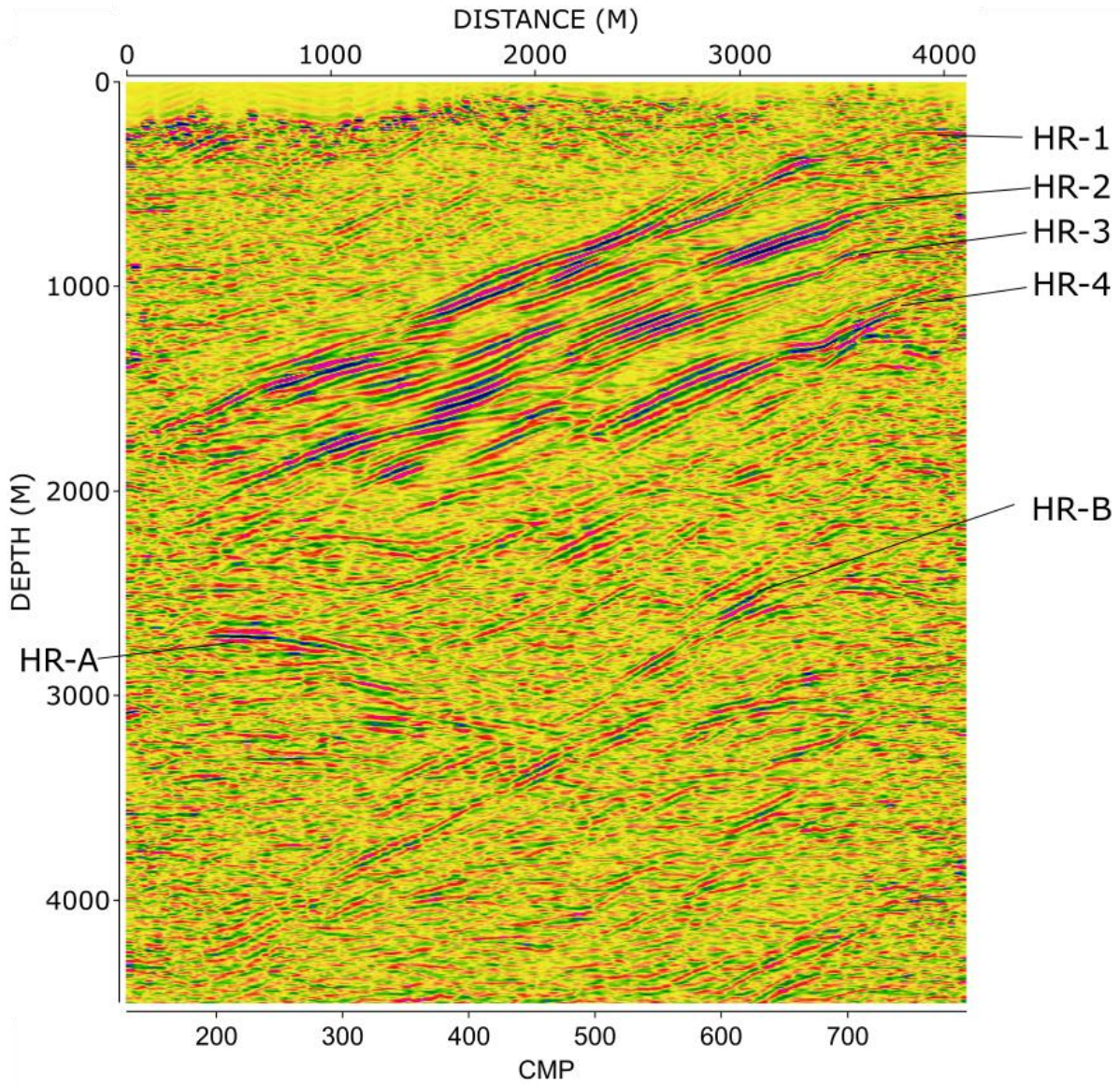

Figure 18 - Final migrated section for Hannukainen profile E1, with labelled reflectors. .

For the proceeding AVO and attribute analyses, alternate seismic sections were computed. For these analyses the AGC was not applied as this interferes with the relative amplitude content of the data, as does the post stack semblance filtering and trace mixing, and for this reason they were also not applied. A trace balancing filter was applied where constant time windows of 150 ms with a 50 ms overlap was designed to horizontally balance the trace amplitudes without the use of AGC.

6.1.1.4 Interpretation

Many strong reflectors are seen with similar orientation, dipping to the south of the line. The upper three-layer reflector package interpreted by Kukkonen et al. (2009) is seen to appear as

more of a four-layer package (labelled HR-1 to HR-4 in Figure 18). These layers will be examined further with the use of seismic attributes in this study. Noticeably different than the final section presented by Kukkonen et al. (2009) is the strength of the deeper reflectors (HR-A and HR-B in Figure 15), they appear to have much stronger amplitudes in the stack presented in Figure 18. Two distinct dips in these reflections are seen, with HR-B dipping in a similar direction to the above four-layer reflector package, and HR-A dipping in much the opposite direction. HR-A shows a strong amplitude at a depth of 2700m that was included in the interpretation of Kukkonen et al. (2009) for reflector Re-3. But due to its dip direction it would be more accurate to describe it as a separate distinct reflector. Some smaller reflections are seen throughout dipping in similar direction as the upper four-layer package

As previously mentioned, the geometry of the CMP profile for E1 was tested with three separate CMP profiles. Geometry A (Figure 19) is what has been presented in the above sections, a straight profile that runs through the shot/receiver profile deviation. Geometry B (Figure 20) runs straight from end to end of the shot-receiver profile, and Geometry C (Figure 21) is slightly curved to compensate for the shot-receiver profile deviation.

The resulting seismic sections are presented beside their geometries, these sections were processed using the same flow as seen in Table 4. The horizontal reflectors are better shown by the more linear Geometries A and B. Geometry C, a more curved profile, doesn't represent these reflectors as well. Geometry C seems to show the very deep reflectors (below 4000 m) a bit better perhaps, but these are not as important in this study as the shallower reflectors that are shown better in Geometries A and B. There isn't much of a difference between geometries A and B, but it could be said geometry A is slightly better at projecting the reflective structures seen along the profile.

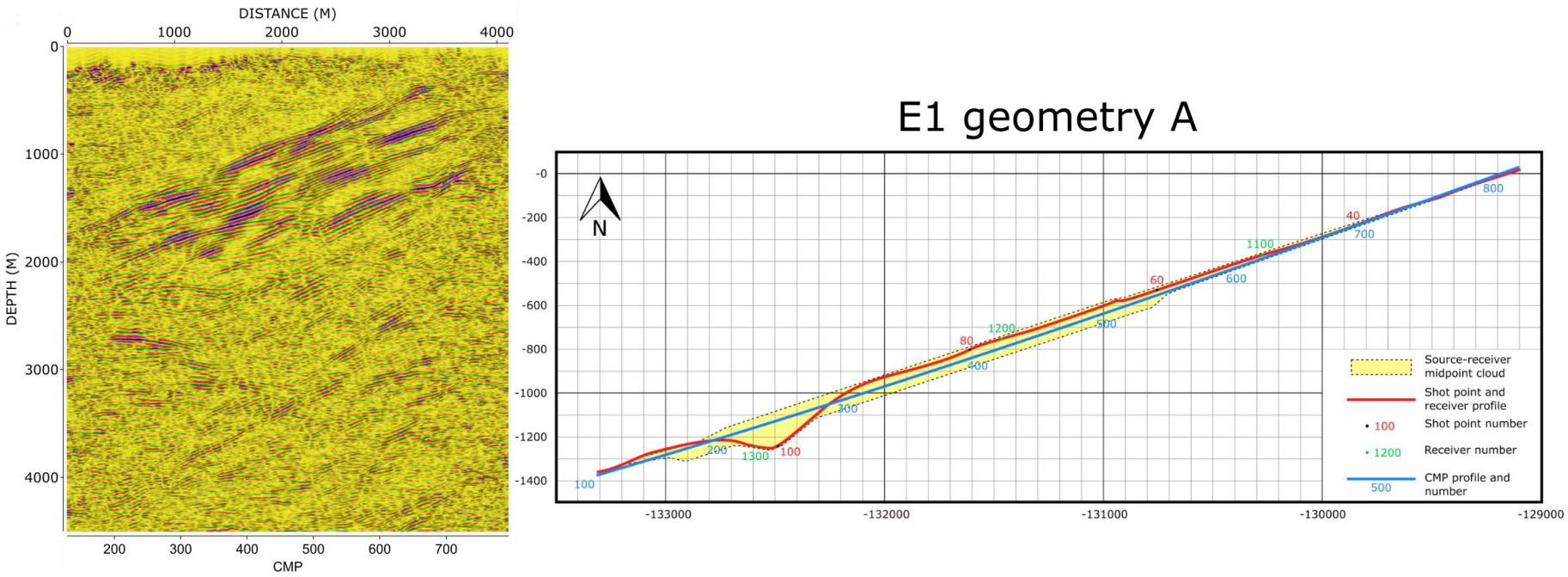

Figure 19 - Seismic section (left) and survey profile (right) for Geometry A for profile E1.

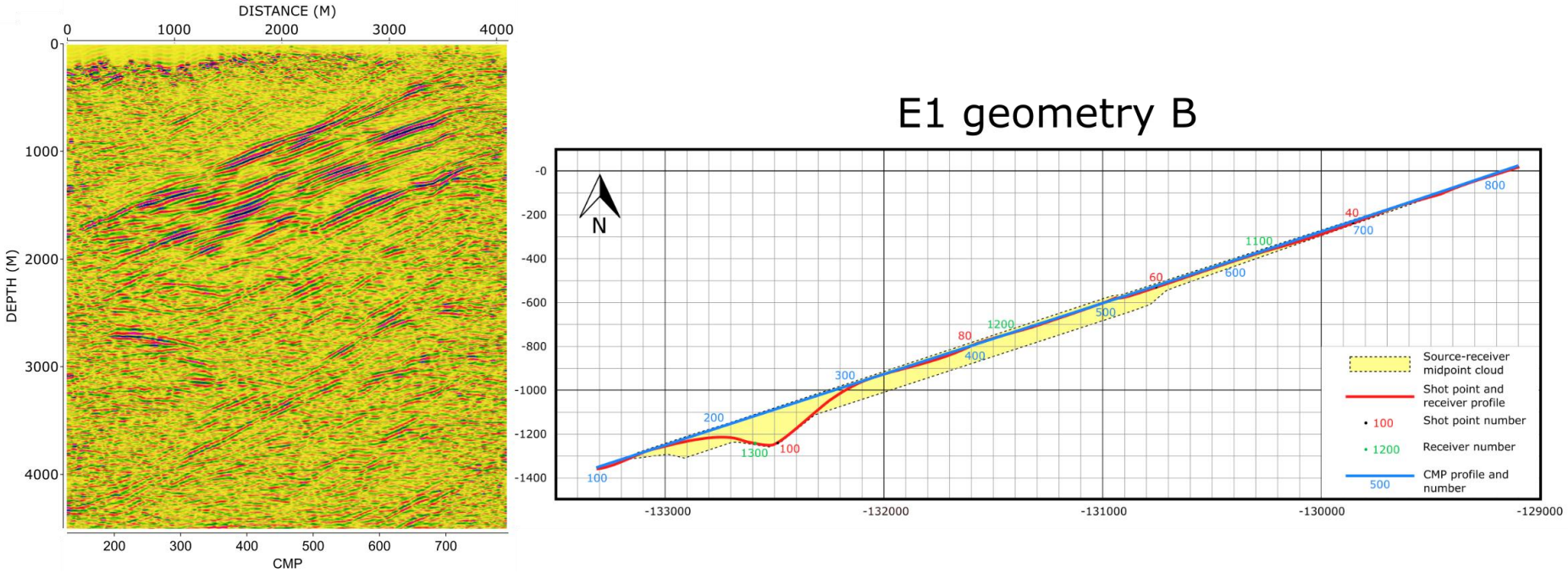

Figure 20 - Seismic section (left) and survey profile (right) for Geometry B for profile E1.

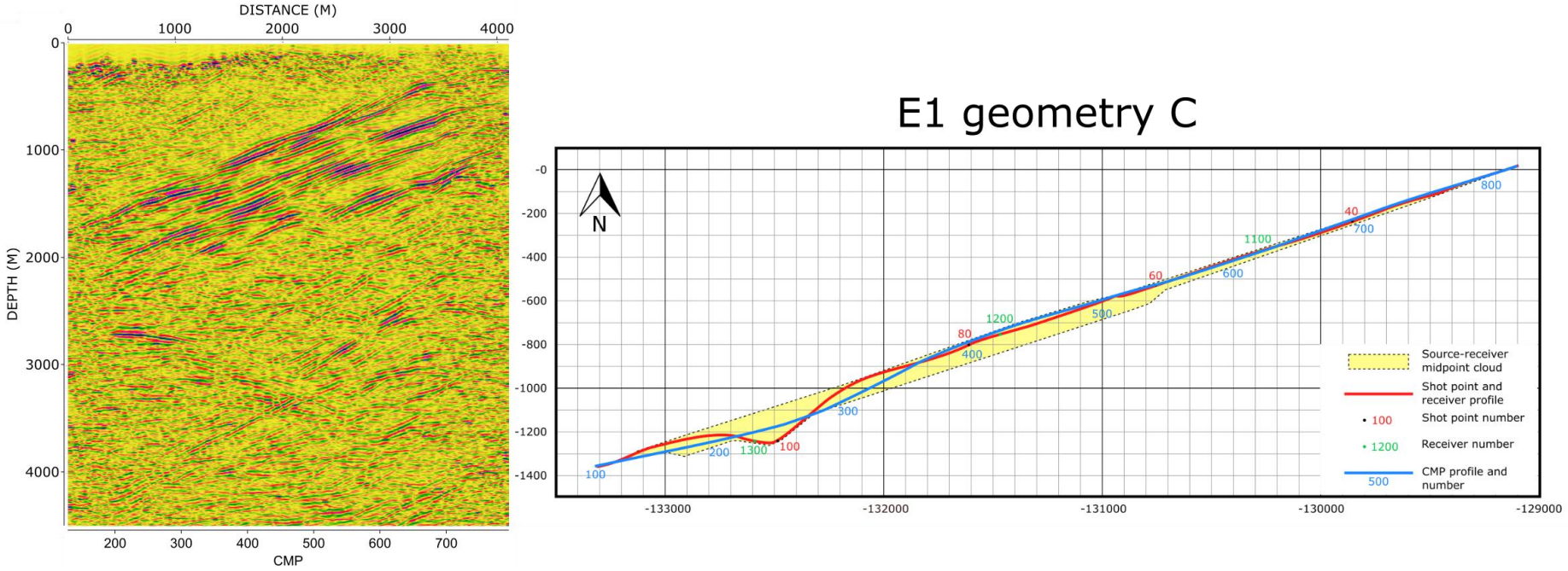

Figure 21 - Seismic section (left) and survey profile (right) for Geometry C for profile E1.

Limiting offsets in certain ranges may reveal features in the seismic section that are otherwise masked when the full offset range is presented. For profile E1 the full offset range is -4500 m to 4500 m. Figure 22 & 23 shows limited offset stacks with their various absolute offset ranges labelled in 1000 m increments, with the top end including from 4000 m to 4500 m offsets as there is very little data in this range as can be seen in the final offset range section.

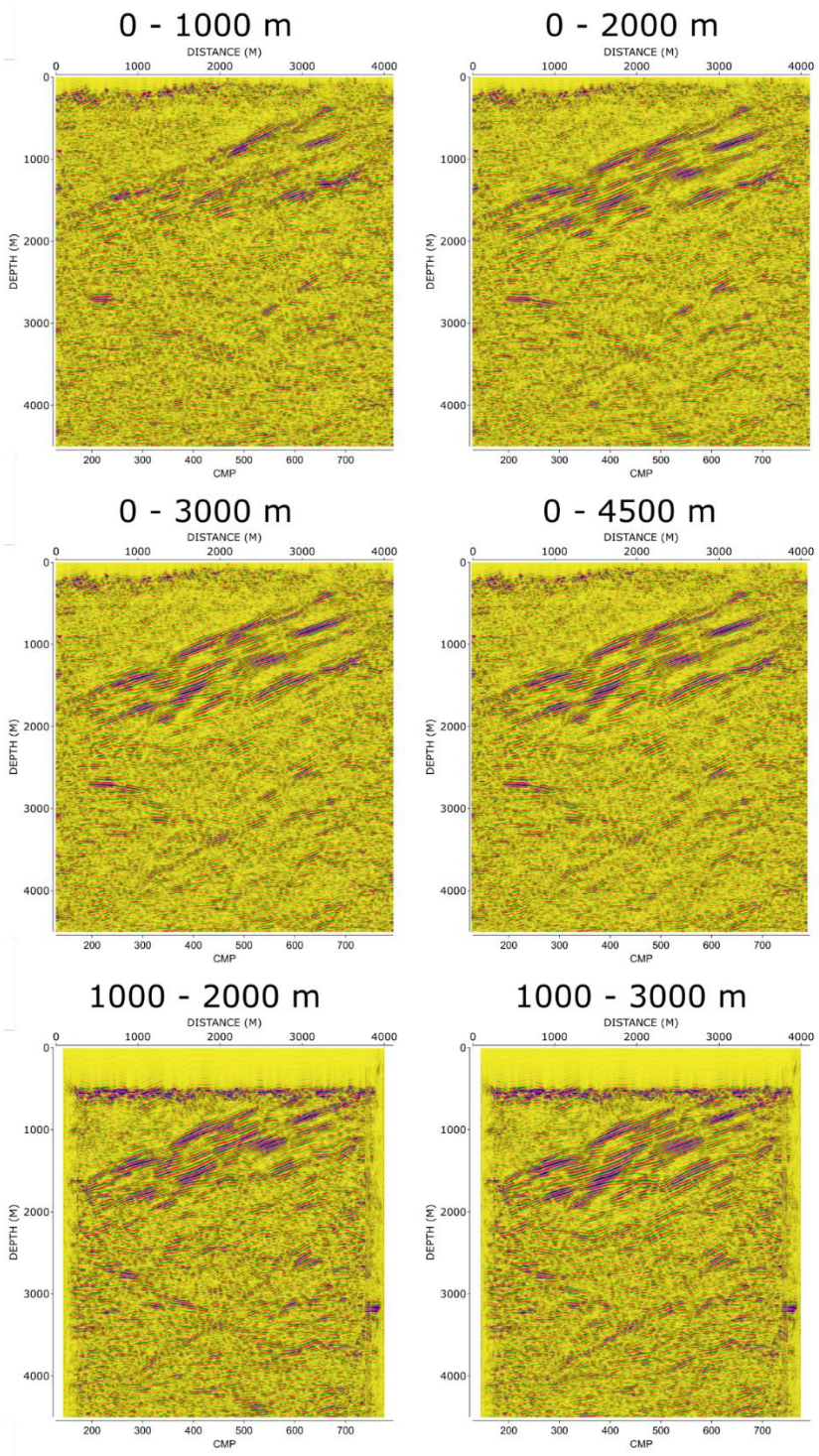

Figure 22 - Offset range stacks of profile E1

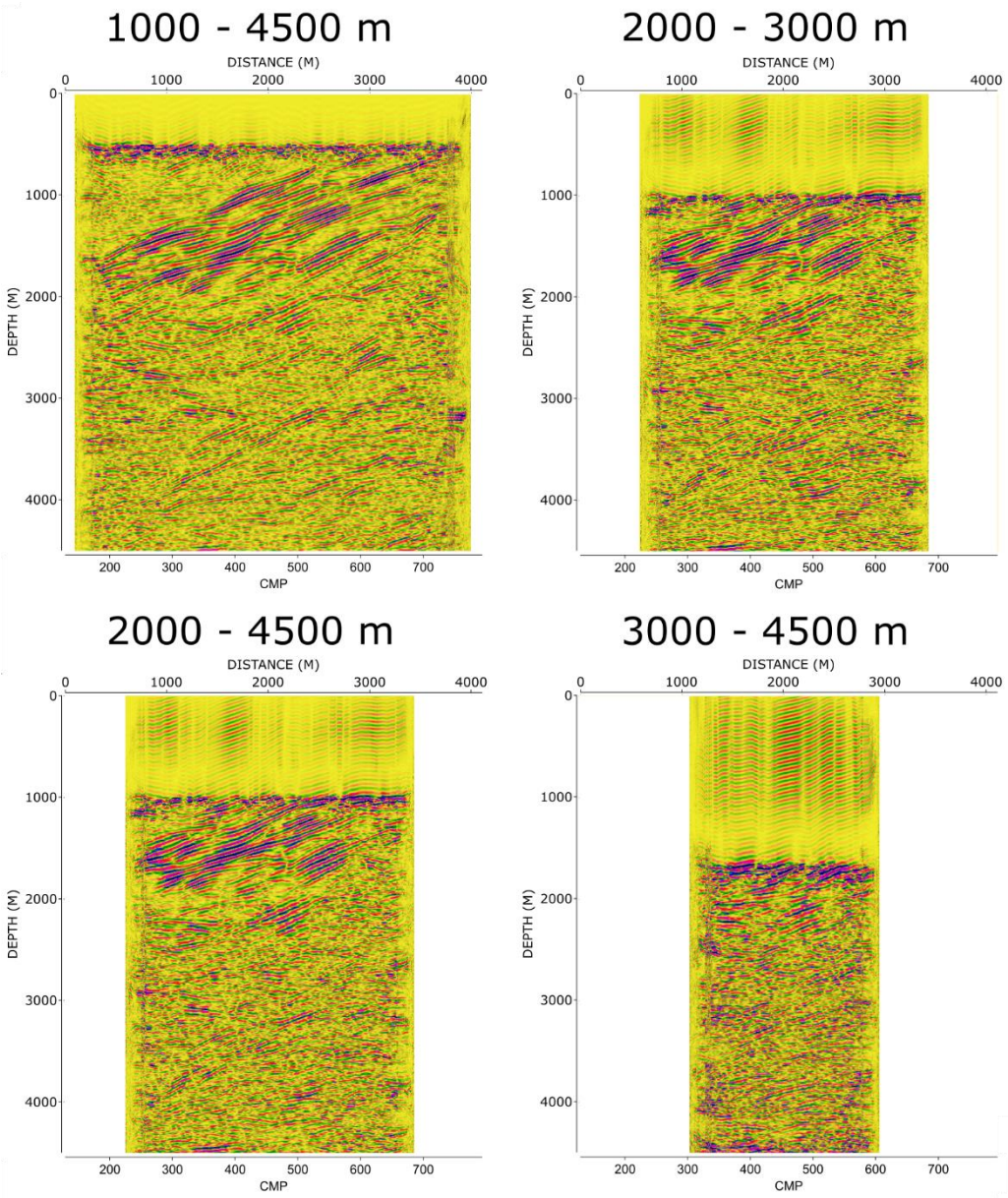

Figure 23 - Offset range sections for profile E1 (cont.).

In the limited offset sections the upper reflector package is mainly contained within the firs 3000 m of offset data. From 3000 - 4500 m there isn't much data seen, with some feint reflectors from below the upper four-layer reflector package. The reflector seen just beneath the upper four-layer reflector package at ~2000 m depth experiences an increase in reflectivity respective to the above package with increasing offset. This is seen clearly in the between the 1000 - 4500 m and 2000 - 4500 m offset sections.

6.1.2 Profile V5

The processing flow for the Vibroseis data of profile V5 is shown in Table 5.

Table 5 - Pre- and post-stack processing for the Vibroseis profile V5.

Pre-stack processing:
1. Assign CDP Geometry addition. CDP spacing 6.25 m. Perpendicular CDP bin size 100 m.
2. First break picking. Maximum offset 800 m.
3. Refraction static corrections through inversion of first break picks. Three-layer model with varying velocity. Floating datum level of 250 m above sea level with 5500 m/s replacement velocity.
4. Geometrical spreading correction.
5. Airwave attenuation. Velocity 330 m/s.
6. S-wave attenuation. Velocity 2700 m/s.
7. Muting of high amplitude traces.
8. Trace amplitude balancing.
9. Band-pass filtering. Corner frequencies 30-40-200-240 Hz.
10. Predicative deconvolution. Filter length 100 ms, gap length 5 ms, white noise percentage 0.1, Hanning window applied.
11. Band-pass filtering. Corner frequencies 30-40-140-165 Hz.
12. Trace amplitude balancing.
13. Sort to CDP domain.
14. Surface consistent residual static corrections.
15. Velocity analysis, constant velocity panels.
16. NMO corrections. Stretch mute percentage 50.
17. Stacking. Stack mode = Median.
Post-stack processing:
18. Final datum correction to seismic reference datum (SRD).
19. Kirchhoff Migration. Constant velocity 6000 m/s.
20. FX-domain complex Wiener deconvolution. Filter length 19 traces. Number of traces to filter at a time, 19 traces with 6 trace overlap. Time window size 100 ms with 25 ms overlap.
21. Trace amplitude balancing
22. AGC. Window length 200 ms. For imaging purposes.
23. Band-pass filtering. Corner frequencies 30-40-140-165 Hz
24. Semblance coherency filtering.
25. Trace amplitude balancing.
26. Time to depth conversion using NMO velocity function.

Profile V5 was put through much the same processing flow as profile E1. A three-layer statics model was chosen to handle the overburden layer for profile V5, this was found to work better and give a lower RMS error value that a two-layer model as used for profile E1. The high-pass frequency gate of the band-pass filter for V5 was lowered due to the Vibroseis having a lower

dominant frequency in comparison to the explosive source of profile E1. Bringing the high pass gate down made the final section appear more coherent.

Profile V5 is a crooked-line profile, with much more deviation from the ideal straight line than profile E1. The CMP profile was drawn as a straight line running as well as possible through the shot/receiver profile (Figure 24). However, with such major changes in shot/receiver geometry, there will likely be unavoidable issues with how the reflectors will project on the CMP profile. This can be said especially for the portion of the CMP profile between CMPs 300 and 500 where the orientation of the shot/receiver profile changes multiple times. It was decided to only use the data up to shot point 300, cutting off the end portion of the profile which takes a sharp turn to the west, as the reflectors that would be projected off this portion would not be reliable for interpretation. The final sections show data for 1038 CMPs, which corresponds to ~6.5 km.

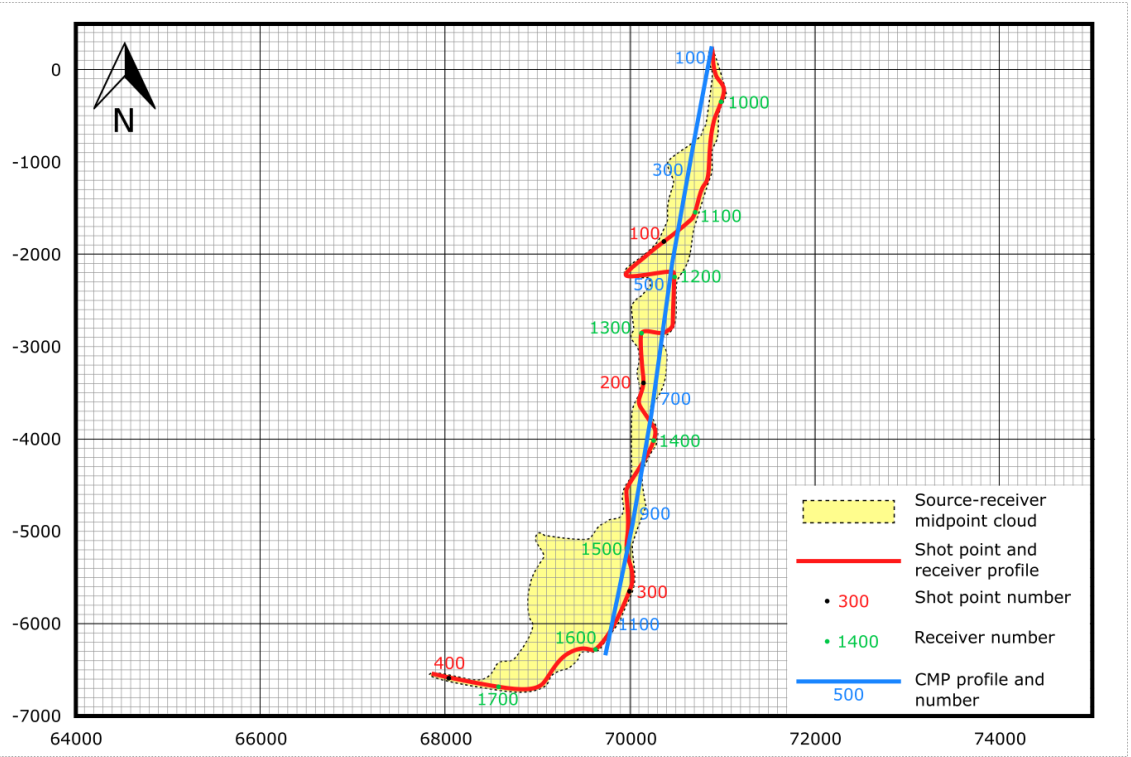

Figure 24 - CMP geometry selected for profile V5 (blue line) overlaid on the shot/receiver profile (red line).

The static corrections for profile V5 proved challenging due to the Vibroseis source. First breaks were much less clear than for profile E1. Instead of picking the clear first onsets, the first phase was picked. Above the first phase was a ringing effect generated by the Vibroseis, which in many places masked where the real first phase was located. This was a laborious

process but in the end a statics model was computed with an RMS error value of 2.94. A three-layer model (Figure 25) was found to fit the picks better than a two-layer model as used for profile E1. The top layer represents the overburden with a constant value of ~500 m/s, the second layer is a weathered bedrock layer with a constant velocity of ~4000 m/s. The third layer is the bedrock layer with a varying velocity of between ~4500 m/s and ~6000 m/s. The resulting refraction statics varied from 0 to 35 ms. The datum statics correction was calculated using an elevation of 250 m and a replacement velocity of 5500 m/s.

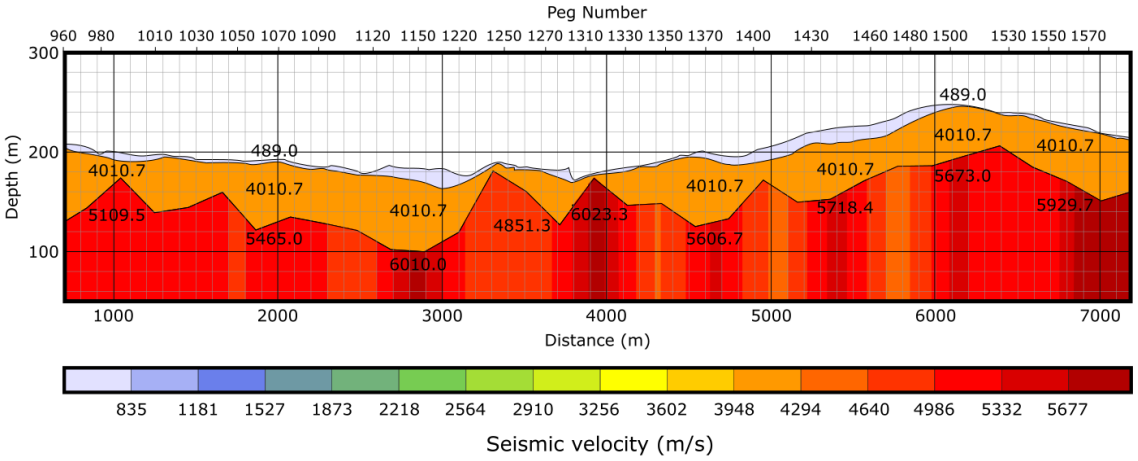

Figure 25 - Calculated three-layer velocity model used for the refraction statics corrections of profile V5.

The rest of the processing flow was applied much the same as for profile E1, with the previously stated difference in band-pass filtering. The final seismic sections, before and after post-stack processing are seen in Figures 26 and 27 respectively.

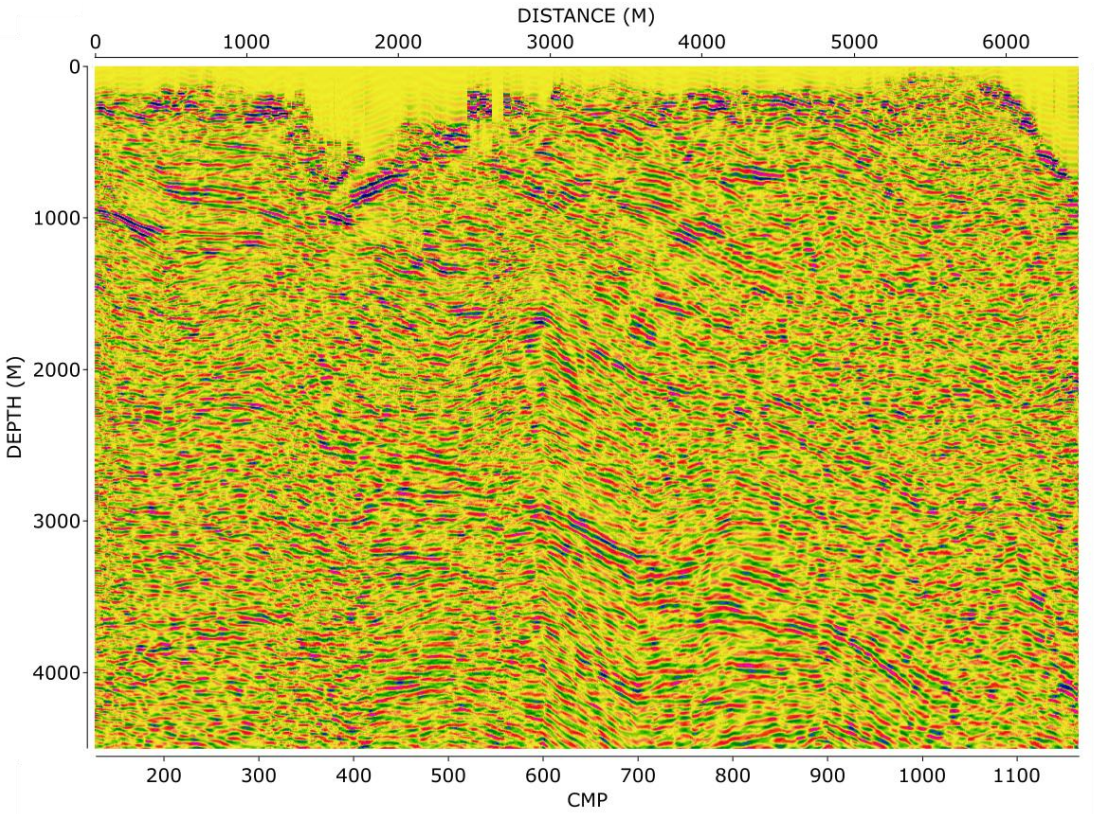

Figure 26 - Migrated seismic section of profile V5 with no post-stack processing applied.

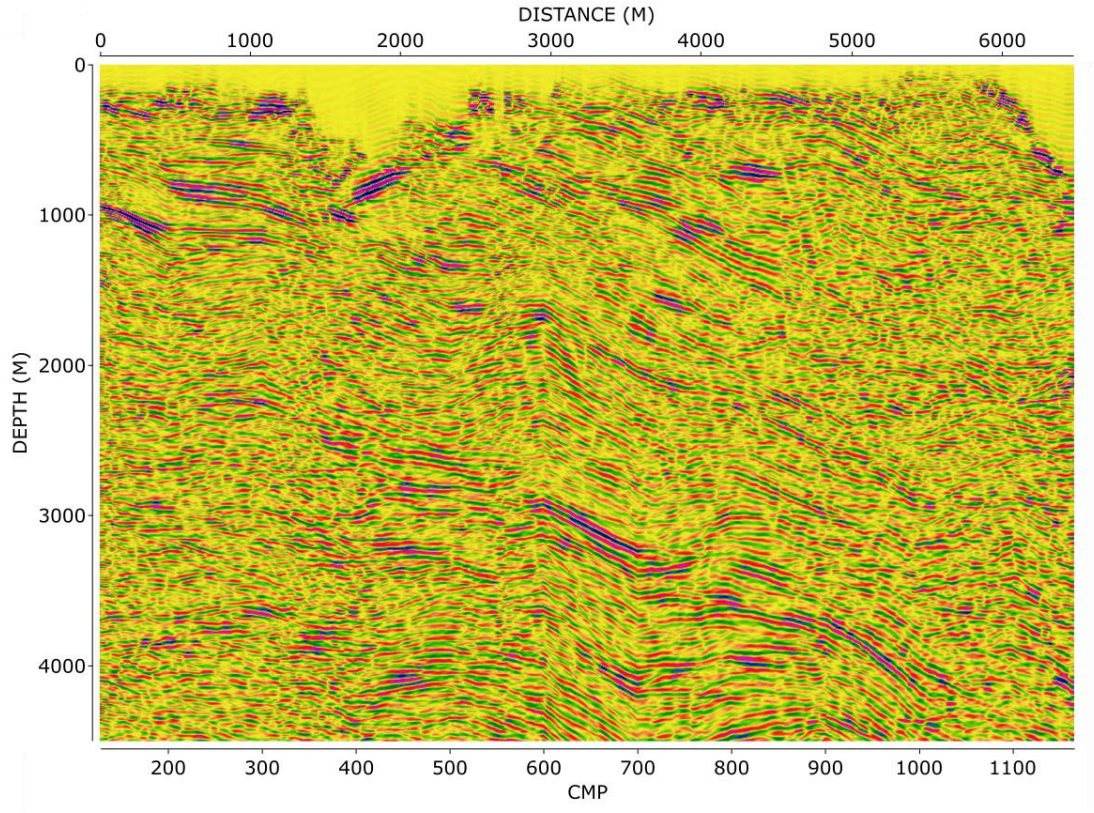

Figure 27 - Migrated seismic section of profile V5 with post-stack processing applied.

6.1.2.1 Interpretation

The correlation of the reflectors in profile V5 to the interpretation of Kukkonen et al. (2012) (Figure 11) throughout the section is a little less obvious as compared to profile E1. Problems arise in the red shaded area of Figure 28 between CMPs 300 and 500 where a large kink in the profile is located (Figure 24), meaning that the reliability of the projection of these reflectors is uncertain. At the start of the profile the upper four-layer package seen in profile E1 (Figure 18) can be seen, though the HR-4 reflector is much less pronounced. Deeper dipping reflectors are seen much clearer than before on the new section, with strong signals seen at ~3 km depth and deeper between CMPs 500 and 1100 (HR-C in Figure 28). This series of reflectors has a varying dip with a major change seen at CMP 700 where it becomes near horizontal before starting to dip again. This series of reflectors could be related to the HR-B reflector seen in profile E1 (Figure 15).

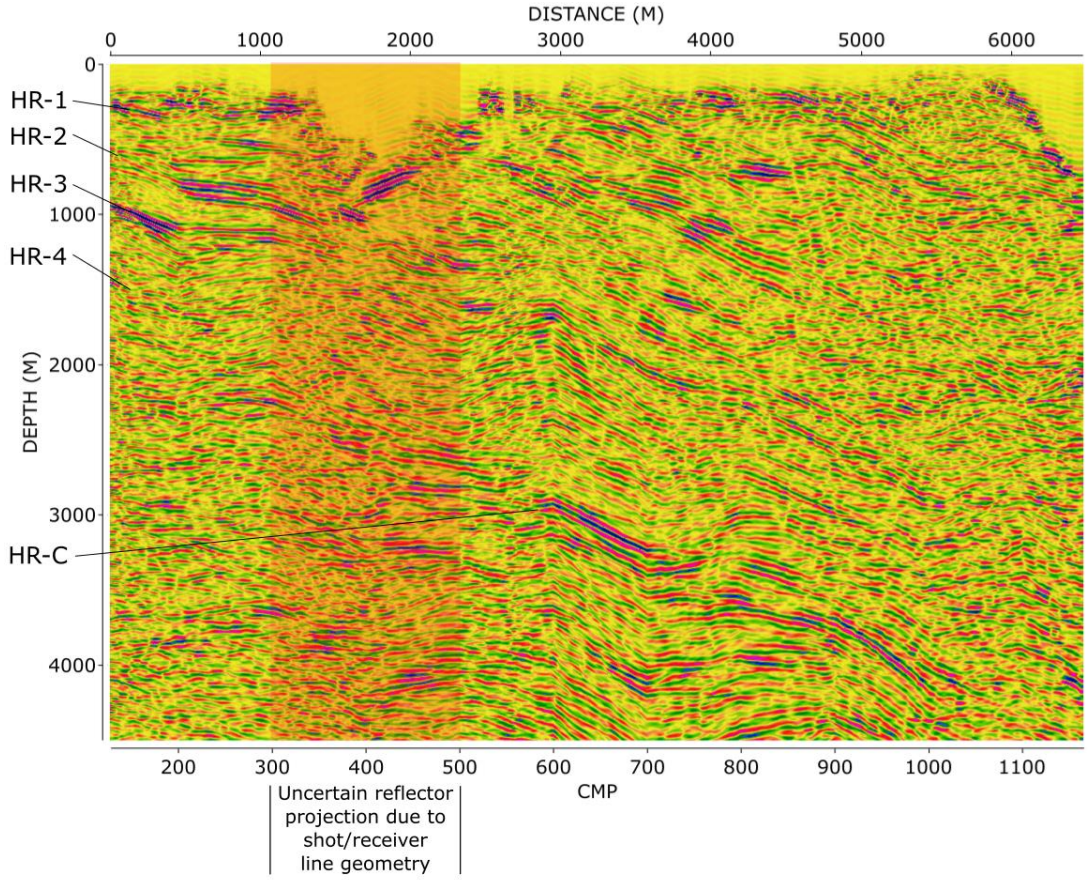

Figure 28 - Profile V5 seismic section with the interpreted layered structure of Kukkonen et al. (2009) overlain. The red shaded region between CMPs 300 and 500 represents an area of uncertainty when it comes to the projection of reflectors due to the kink in the shot/receiver profile

The very deep structures seen in Figure 28 (HR-C and directly below) show much higher amplitudes in this study than in Kukkonen et al. (2009). These reflectors appear to run more coherently in a similar way to the upper 4-layer layer package of reflectors (HR-1 to HR-4).

6.2 AVO analysis

AVO analysis of Hannukainen profile E1 was carried out using GLOBE Claritas software, generating cross plots of amplitude and offset for CMP gathers. The data has been processed using the same flow listed in Table 4, but without the post-stack processing steps 20-23. Following the instruction of the programme, a 3-trace mix was applied to the gathers. Two horizons were identified for AVO analyses, they are labelled AVO1 and AVO2 in Figure 29. Both horizons are located within the upper 4-layer reflector package interpreted in Figure 18. AVO1 is located in reflector HR-1 and AVO2 Is located in HR-2. Both AVO1 and AVO2 run from CMP 595 to 670 (total length ~470 m). Looking at the offset stack images of Figures 22 and 23, it can be seen that AVO1 and AVO2 are mainly resolved from offsets 0 - 2000 m. The maximum offset value available for AVO analysis of AVO1 and AVO2 is 2700 m at CMP 595, and the minimum offset value is 1700 m at CMP 670. The data was analysed using the maximum constant offset of 1700m. By keeping the offset value constant, this should give a better statistical result.

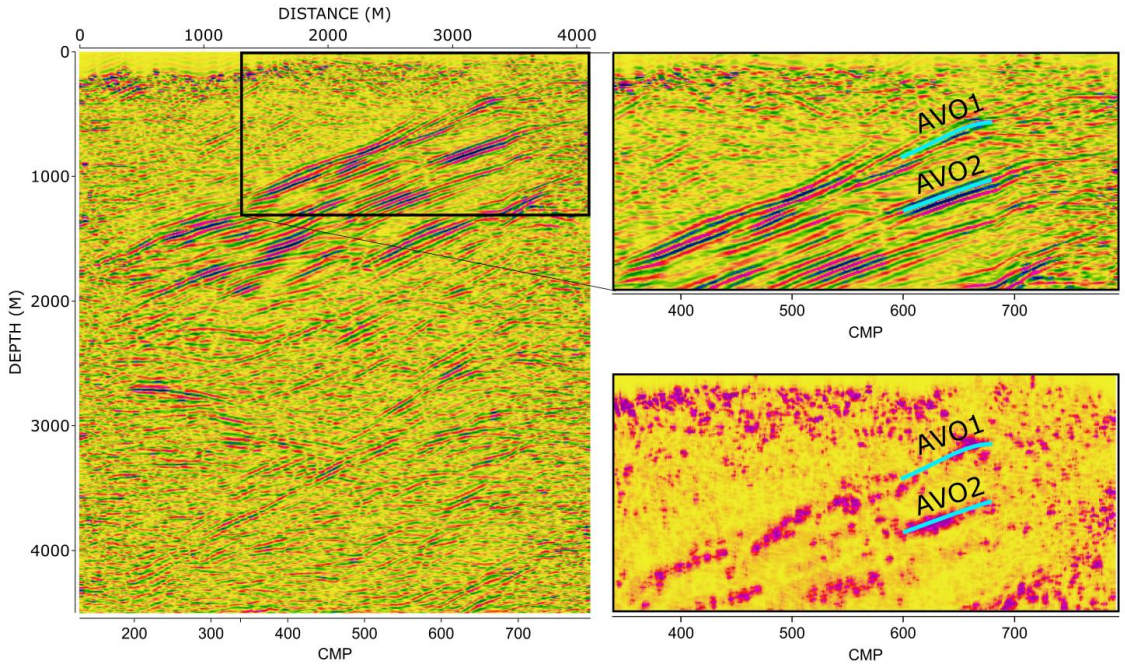

Figure 29 - Locations of the AVO1 and AVO2 horizons on the profile E1 seismic section (top right) and envelope seismic attribute section (bottom right).

Horizons AVO1 and AVO2 are located at depths of approximately 500m and 1000m respectively. Both horizons are within reach of drilling. Amplitude strength across AVO one varies quite a bit as seen in Figure 29. The analysis of AVO1 will determine if a difference in AVO response with varying amplitude strength can be detected. AVO2 is a larger reflector with a stronger amplitude response and a lesser amplitude strength variation across it. Along with the AVO data, some seismic attributes vs. offset data are calculated, namely Instantaneous Amplitude (IAVO), Instantaneous Frequency (IFVO) and Instantaneous Phase (IPVO), this data is plotted along with AVO in Figures 30. Two different least-squares straight line fits are used to determine the offset response, a basic least-squares best fit and a robust least-squares fit. These do not always give the same response, and as such after analysing each response the basic least-squares fit seemed to give the more logical best line fits. The AVO gradient attribute is plotted in Figure 28 to show the degree of amplitude increase or decrease with offset

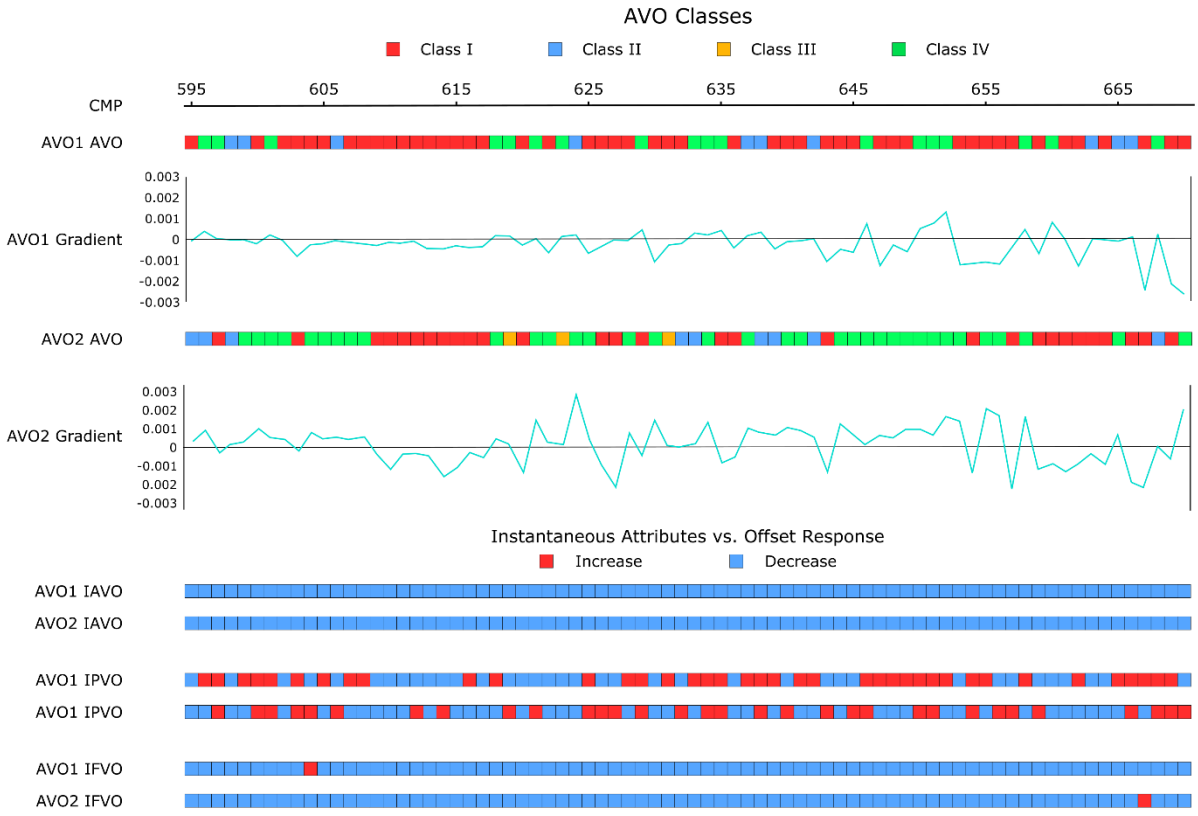

Figure 30 - Results for AVO1 and AVO2, showing apmlitude vs. offset (AVO) effect with gradient, and also seismic attributes vs. offst response. IAVO - Instantaneous Amplitude vs. offset, IPVO - Instantanooue Phase vs. offset, IFVO - Instantaneous Frequency vs. offset.

Classification of the AVO response with the standard hydrocarbon AVO classes as defined in Figure 8 was done for AVO1 and AVO2. The results of this can be seen in Figure 30. The breakdown of the classes in each horizon is seen in Table 6.

Table 6 - Breakdown of number and percentages of AVO classes across horizons AVO1 and AVO2

	AVO Class I	AVO Class II	AVO Class III	AVO Class IV
AVO1				
Number	48	10	0	18
Percentage (%)	63.15	13.15	0	23.7
AVO2				
Number	35	9	3	35
Percentage (%)	38	12	4	46

From Table 6 it is seen that the AVO response differs quite a bit between AVO1 and AVO2. AVO1 is largely dominated by Class I responses with nearly two thirds (63.15%) of the responses seen. Class IV makes up 23.7% of responses and the remaining 13.15 % of responses being Class II. No Class III response is seen in the AVO1 horizon. For AVO2, just under half the AVO responses are Class IV (46%), slightly more than the 38% of Class I responses. Class II responses are at about the same level as seen in AVO 1 at 12% and the remaining 4% are Class II responses.

For the seismic attribute vs. offset response (Figure 30), the IAVO response is seen to be uniform across both AVO1 and AVO2 with a decreasing trend seen at all CMPs. The IPVO response is quite varied in both AVO1 and AVO2, with no obvious pattern noted. For AVO1 there is 39 CMPs with an increasing trend (51.3%) and 37 CMPs showing a decreasing trend (48.7%). AVO2 has slightly more decreasing IPVO trends with 32 CMPs showing an increasing trend (42.1%) and 44 CMPs showing a decreasing trend (57.9%). The IFVO responses are the same with each horizon having one CMP that garners an increasing trend. Mazzotti (1991) stated that hydrocarbon bearing sand could possibly be identified by an increasing IAVO trend along with a relatively constant IPVO trend. No increasing trend in IAVO is seen in this data so this type of indicator is not present in this study.

Cross-plotting of the slope and intercept was done for both AVO 1 and AVO2 (Figure 31). The cross-plotting reveals no anomalous clusters of gradient/intercept response which would be located above or below the background response.

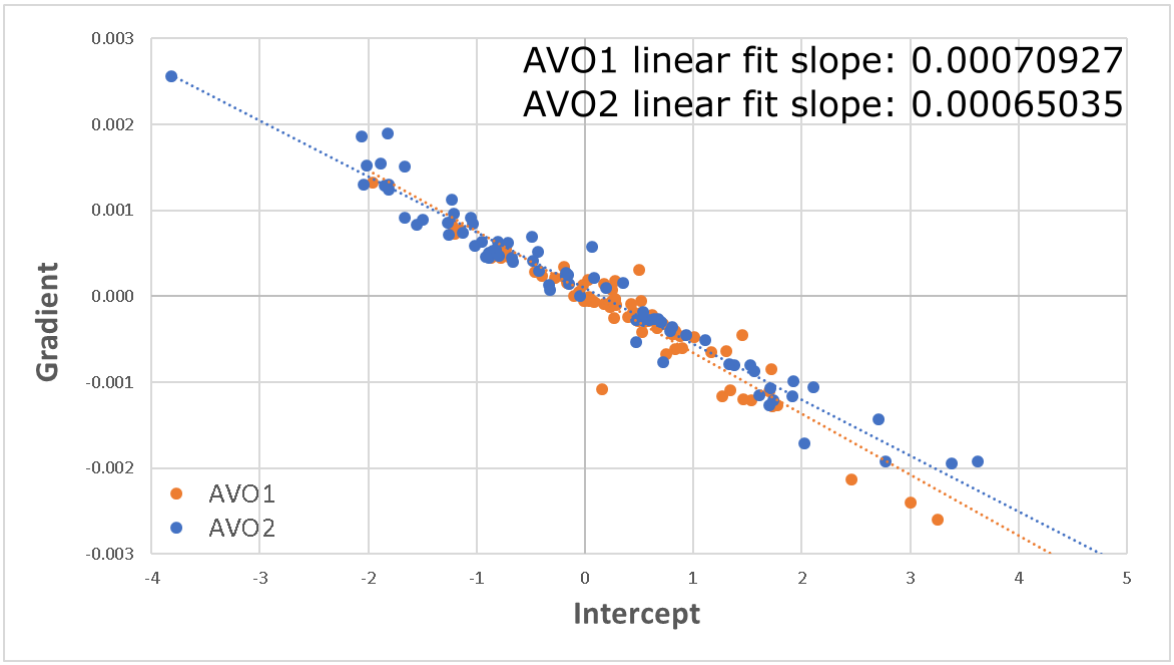

Figure 31 - AVO cross-plot for AVO horizons AVO1 and AVO2.

From the AVO linear fit slopes, a value for Poisson's ratio is calculated across both horizons using Equation 20. The resulting values show a slightly higher Poisson's ratio value for AVO1 of 0.3548, in comparison to 0.3537 for AVO2. A higher slope in AVO1 suggest a larger average change in Poisson's ratio. The Poisson's ratio change can also be calculated at each CMP using Equation 20, the results of this calculation for both AVO1 and AVO2 are seen in Figure 32.

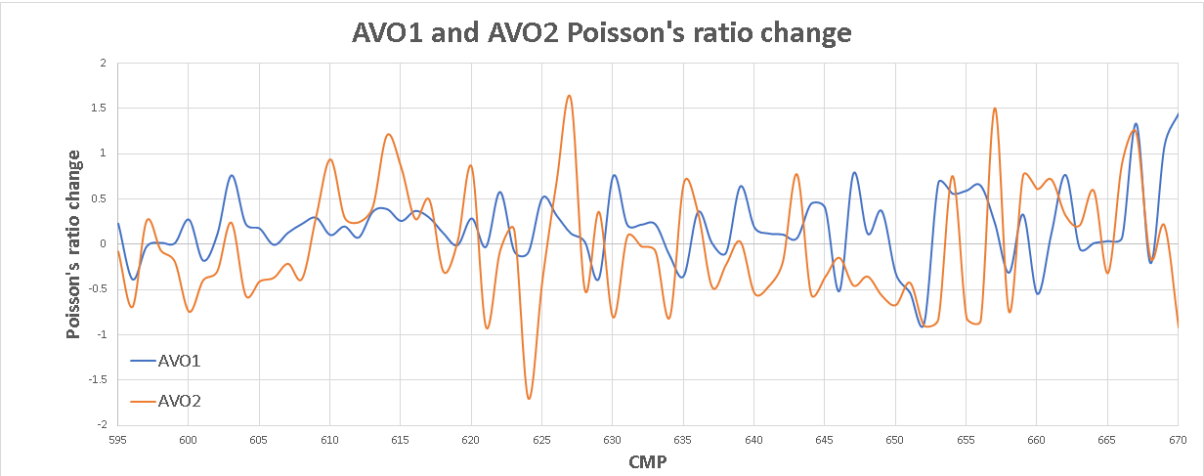

Figure 32 - Poisson's ratio change across AVO1 and AVO2.

In Figure 32 it is seen that the change in Poisson's ratio across each horizon greatly varies spatially. AVO1 seems to have a more net positive change value which would match with the what was indicated by the slope of the AVO cross plot (Figure 32). AVO2 experiences more extreme change across the board. Increasing Poisson's ratio change is seen in both horizons best between CMP 608 and 617.

Another AVO characteristic that can be calculated for AVO1 and AVO2 is the AVO product, how this value varies across each horizon is presented in Figure 33.

Figure 33 - AVO product for horizons AVO1 and AVO2.

AVO product will always be positive for Class III AVO responses as the gradient and intercept always have the same sign (positive or negative). Class I responses will always have a negative AVO product as the gradient and intercept will always have different signs (one positive, one negative). Class II and Class IV AVO responses can have either positive of negative AVO products. In this data, strong positive AVO products are not seen, but strong negative AVO products are abundant. Between CMPs 647 and 661 an area of consistent and strong negative AVO product is seen, this area shows Class I and Class IV responses in Figure 30. Correlating with Figure 32 it is seen that this area of CMPs encounters some strong positive anomalies in Poisson's ratio change also.

6.3 Attribute analysis

Attribute analysis was done using GoCAD software, the attributes that will be presented and presented here are envelope (instantaneous amplitude), first derivative envelope, Hilbert Transform, relative impedance, instantaneous weighted frequency, instantaneous phase and dip. These attributes are used to enhance interpretation of the seismic reflection data. Using these attributes, areas of increased reflectivity and continuity can be identified that are not seen in the standard seismic data display. Also, correlations across various different attributes can be made to further bolster interpretation, especially when combined with drilling data from the area. For attribute analysis the data used for profiles E1 and V5 have no AGC applied, instead a stack balancing filter is applied to balance horizontal trace amplitudes throughout the section. This filter was designed with 150 ms window moving down the traces with an overlap of 50 ms. Also, no semblance filtering or trace mixing has been applied, in an effort to retain as much of the relative amplitude data as possible. The application of AGC and the mentioned post-stack processing steps would greatly affect the data, which could lead to inaccurate interpretations.

6.3.1 Profile E1

The attributes presented in Figure 34 are the instantaneous attributes related to amplitude, namely Envelope, First Derivative Envelope, Hilbert Transform and Relative Impedance.

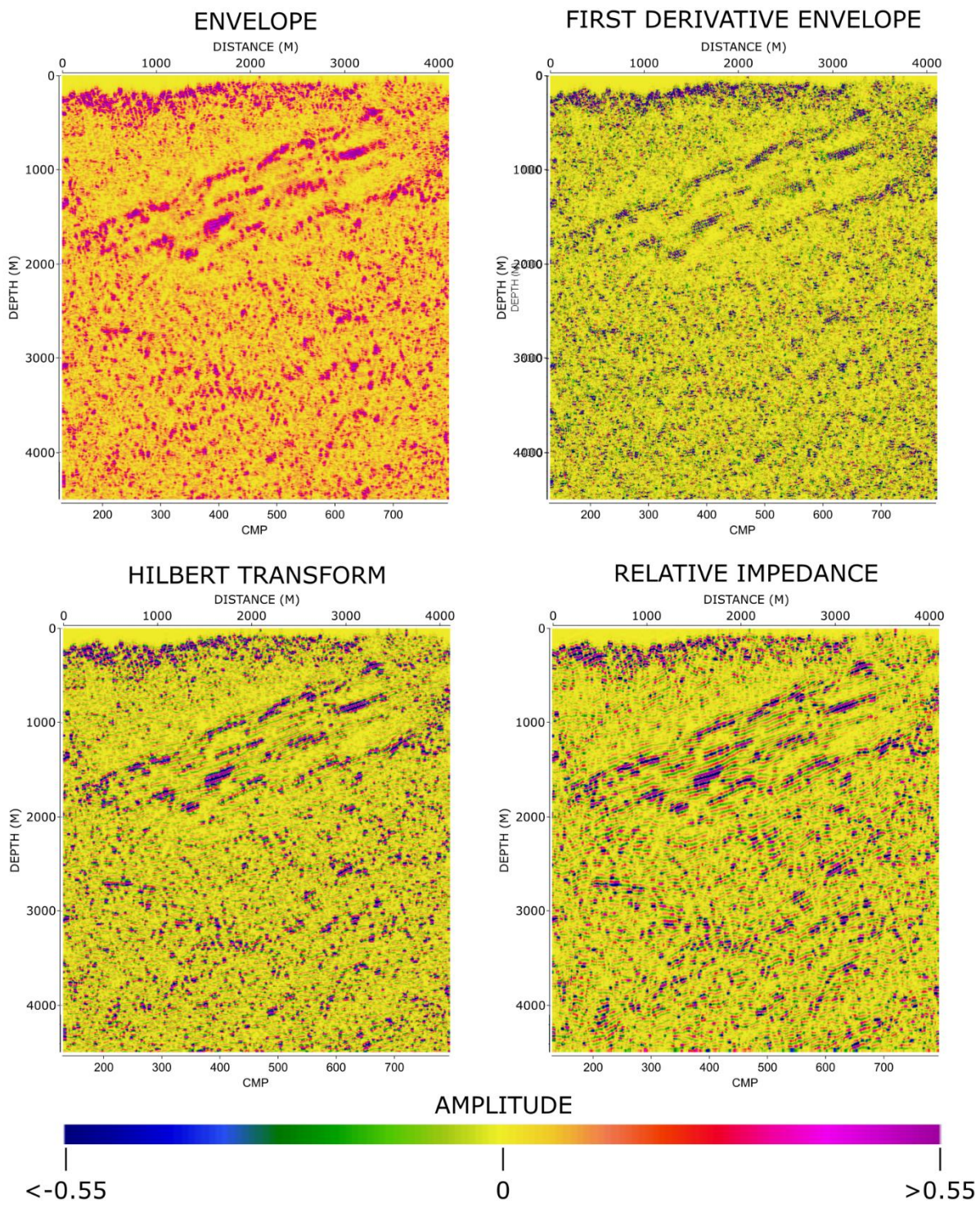

Figure 34 - Seismic attribute sections for profile E1, attributes presented are Envelope (top left), First Derivative Envelope (top right), Hilbert Transform (bottom left) and Relative Impedance (bottom right).

These attributes show a very similar picture of the data throughout the four different attributes. The upper four-layer reflector package is well represented in all attribute sections in Figure 34. The selected reflectors for AVO1 and AVO2 (Figure 29) are represented in all of these amplitude attribute sections. This indicates the strong relative impedance contrast seen between these selected reflectors and the surrounding medium both the normal sense in the Envelope

section and the apparent band-limited sense in the Relative Impedance section. The First Derivative Envelope section indicates that a sharp interface is seen at these reflectors. The Hilbert Transform attribute shows that there is little to no effect resulting from the rotational transformation on the seismic data. Next, the instantaneous phase and instantaneous weighted frequency attributes are examined, which should enhance the continuity of the upper four-layer reflector package. These attributes show four distinct and separate layers (corresponding to HR-1 to HR-4 in Figure 18) apparent in both attribute sections. The phase attribute section (Figure 35) enhances the continuity of the upper four-layer reflector package. In the east side of the profile where the reflector package is located near the surface there is a clear four-layer system seen in the phases. These distinct layers get less pronounces if you follow the same phase throughout the package as it dips deeper in the section. The top of the layer package is seen at 450 m and the bottom at 1500 m approximately. These four distinct layers at shallow depths are also shown in the weighted instantaneous frequency attribute section (Figure 36).

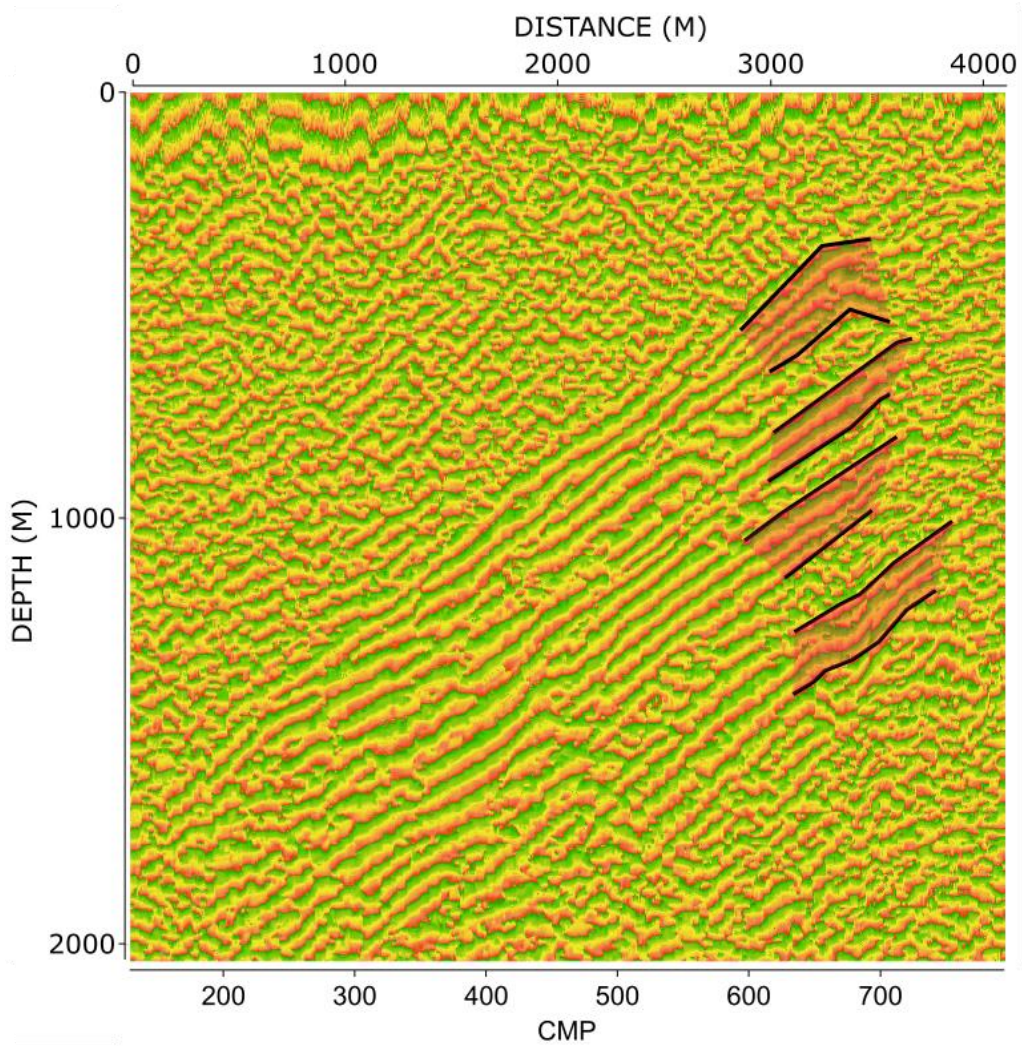

Figure 35 - Profile E1 Instantaneous phase attribute stack with 2x vertical exaggeration.

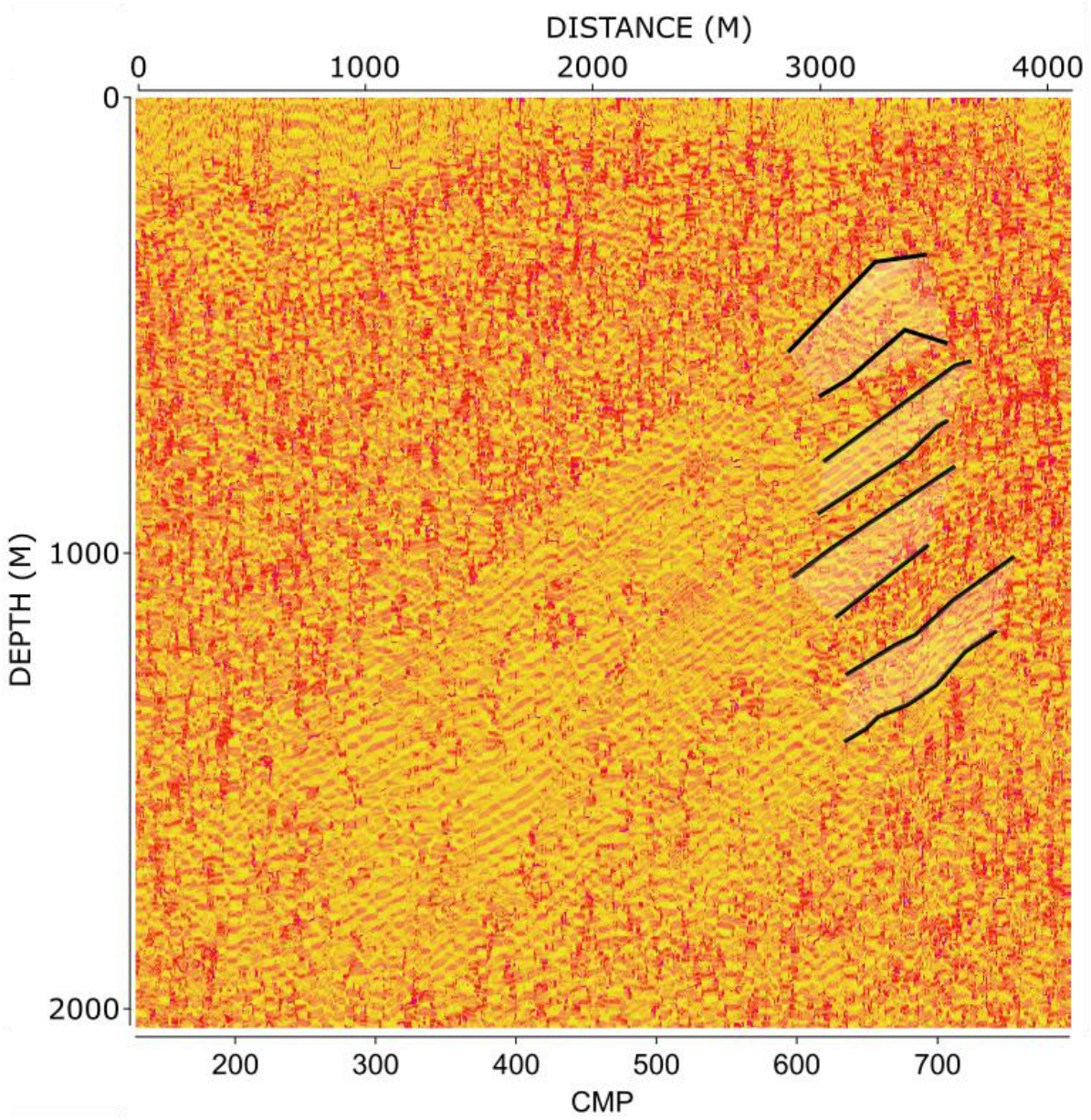

Figure 36 - Profile E1 weighted instantaneous frequency attribute section with 2x vertical exaggeration.

In the weighted frequency attribute section, it can be seen that there are four distinct layers in the reflector package at its shallowest point. Much like the phase attribute section the separation of the layers is lost as the package dips deeper into the subsurface. Interpreting the same layers from one side of the profile to the other would involve too much crossing of phases as seen in in the phase attribute section. The geometric dip attribute resulted in some interesting, and perhaps questionable results (Figure 37).

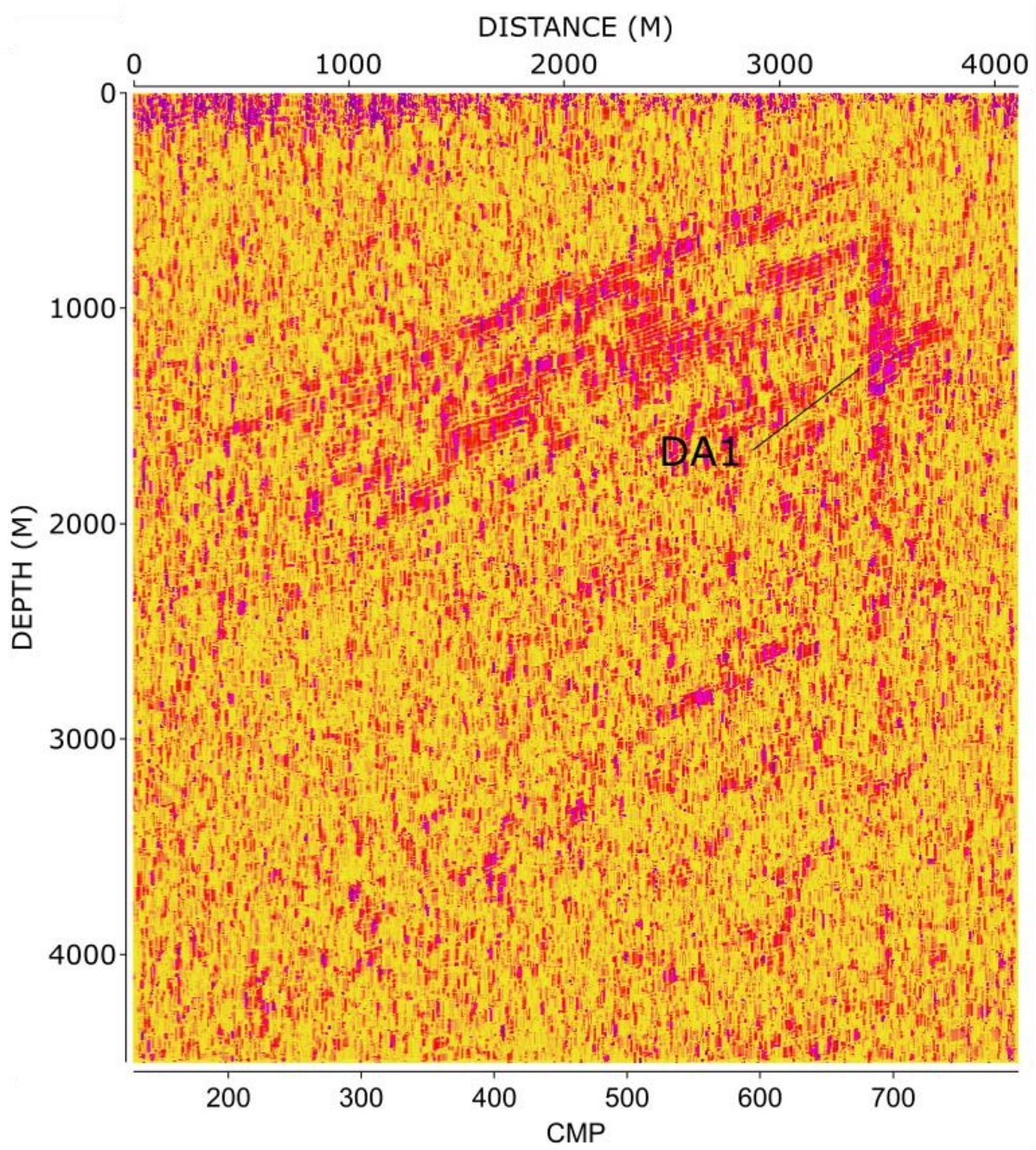

Figure 37- Profile E1 dip attribute section with dip anomaly DA1 labelled.

The dip attribute section, while again well representing the upper four-layer reflector package also shows a peculiar vertical response, DA1, at CMP 700. The response is seen strongest between 80m and 200 m depth. This anomaly does correlate with a thrust fault which is seen in Figure 38 that in encroaching on this area of profile E1, though it is shown to run short of the CMP profile. It is unsure if this is something real, but it is also hard to ignore the correlation with local faulting. As such the interpretation of this particular attribute remains questionable but is worth presenting, nevertheless.

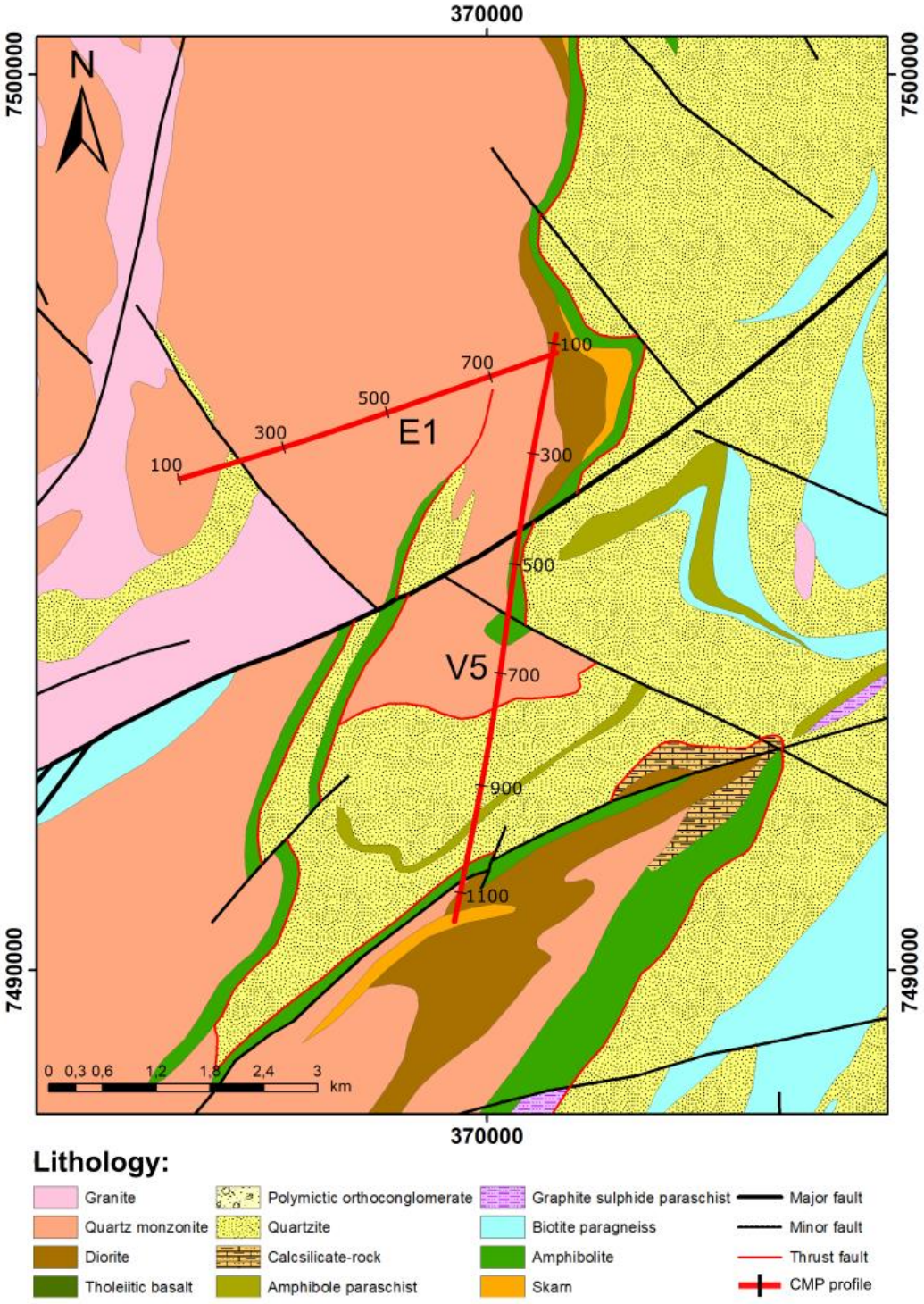

Figure 38 - Geological setting of CMP profiles for E1 and V5. Coordinates are in the EUREF-FIN ETRS-TM35FIN system. Lithology data: Bedrock of Finland 1:200 000 © Geological Survey of Finland 2016.

6.3.2 Profile V5

The same four amplitude attributes, as shown for profile E1, are shown for profile V5 in Figure 39, namely, Envelope, First-Derivative Envelope, Hilbert Transform, and Relative Impedance.

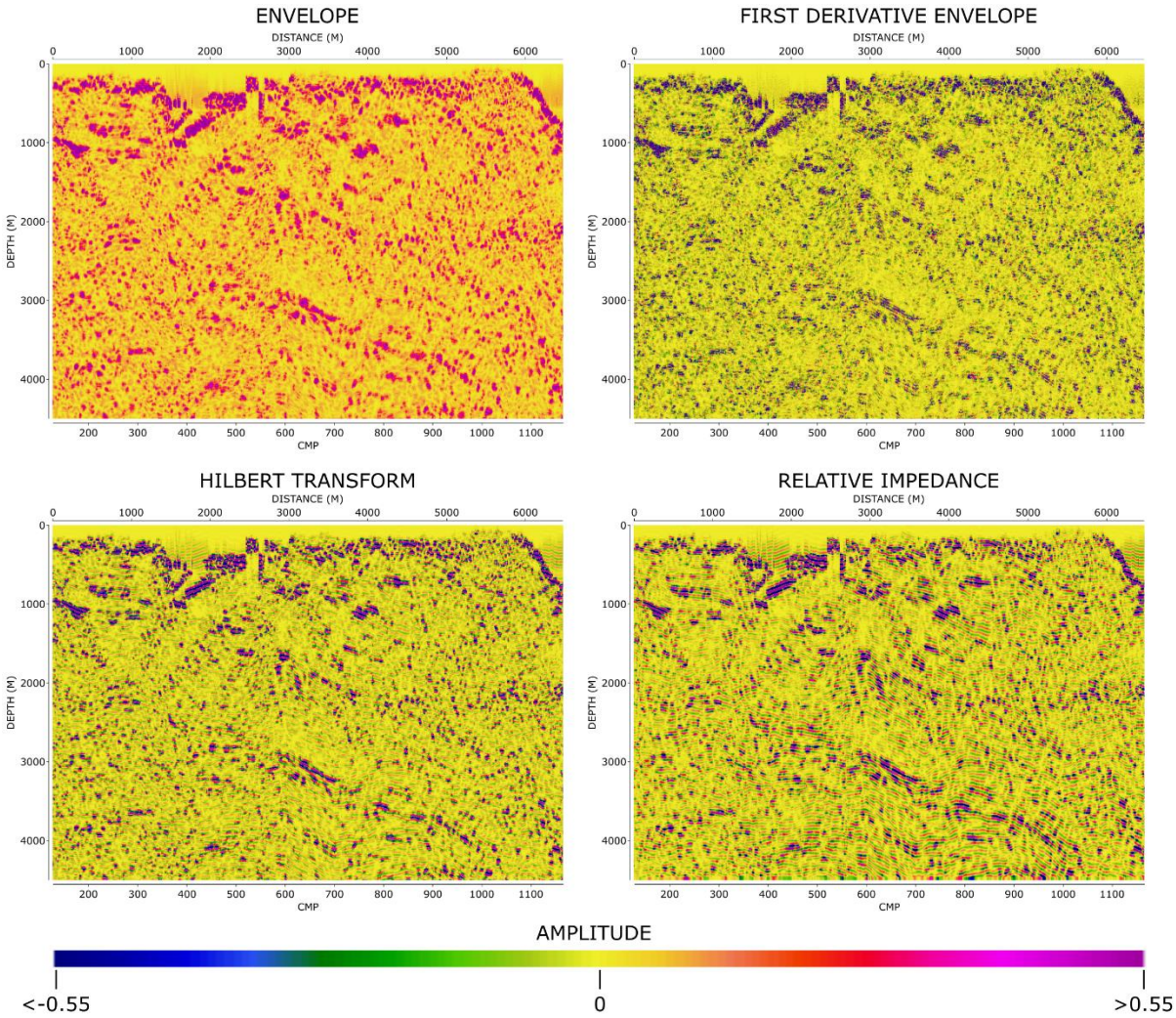

Figure 39 - Seismic attribute sections for profile V5, attributes presented are Envelope (top left), First Derivative Envelope (top right), Hilbert Transform (bottom left) and Relative Impedance (bottom right).

In comparison to profile E1, the amplitude attribute sections don't show as obvious a trend throughout. One thing that has to be considered with profile V5 is the uncertainty in reflector projection between CMP 300 and CMP 500 (Figure 28). However, the attribute response seen at 1000 m depth at the start of the profile (CMP 170) shows a very strong response in all sections, this corresponds with HR-3 as interpreted in Figure 28. This implies that this reflector has a strong relative impedance contrast with the surrounding medium form the Envelope section, and a strong apparent band-limited impedance contrast from the Relative Impedance section. The Hilbert Transform shows that there is little to no effect resulting from the rotational transformation of the seismic data, similar to profile E1. From the First Derivative attribute it can be said there is a sharp interface at this reflector. The deep dipping reflector also shows up nicely in these sections with two strong continuous reflectors starting at CMP 500 at depths of 1500 m and 2800 m respectively and running to CMP 1000 at depths of 3000 m and 4300,

respectively. These show a weaker response in comparison to the shallow reflector. The phase attribute for profile V5 is used to enhance the continuity of the reflectors (Figure 40).

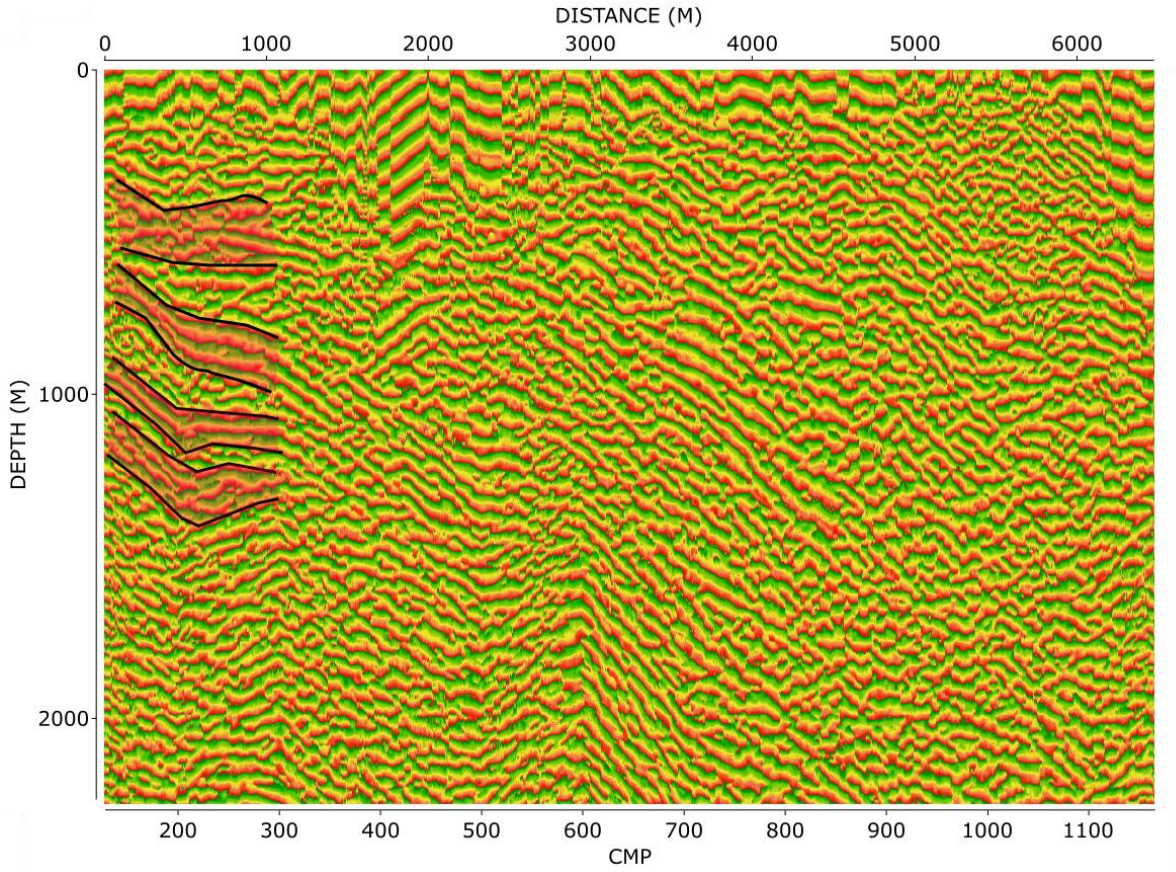

Figure 40 - Profile V5 Instantaneous phase attribute section with 2x vertical exaggeration.

The upper four-layer reflector package as was interpreted for profile V5 (Figure 28) can also be seen in the phase attribute section. Though the interpretation is somewhat less certain than that of profile E1 (Figure 35). The thickness and location of the four-layer reflector package seen in the phase attribute sections of profile E1 is the same as would be expected. The phases are interrupted at CMP 330 by the uncertain reflector projection problem that was encountered in the data processing stage. Unlike profile E1 there is no clear correlation with the weighted instantaneous frequency attribute. Next, we look at the dip attribute section for profile V5 (Figure 41).

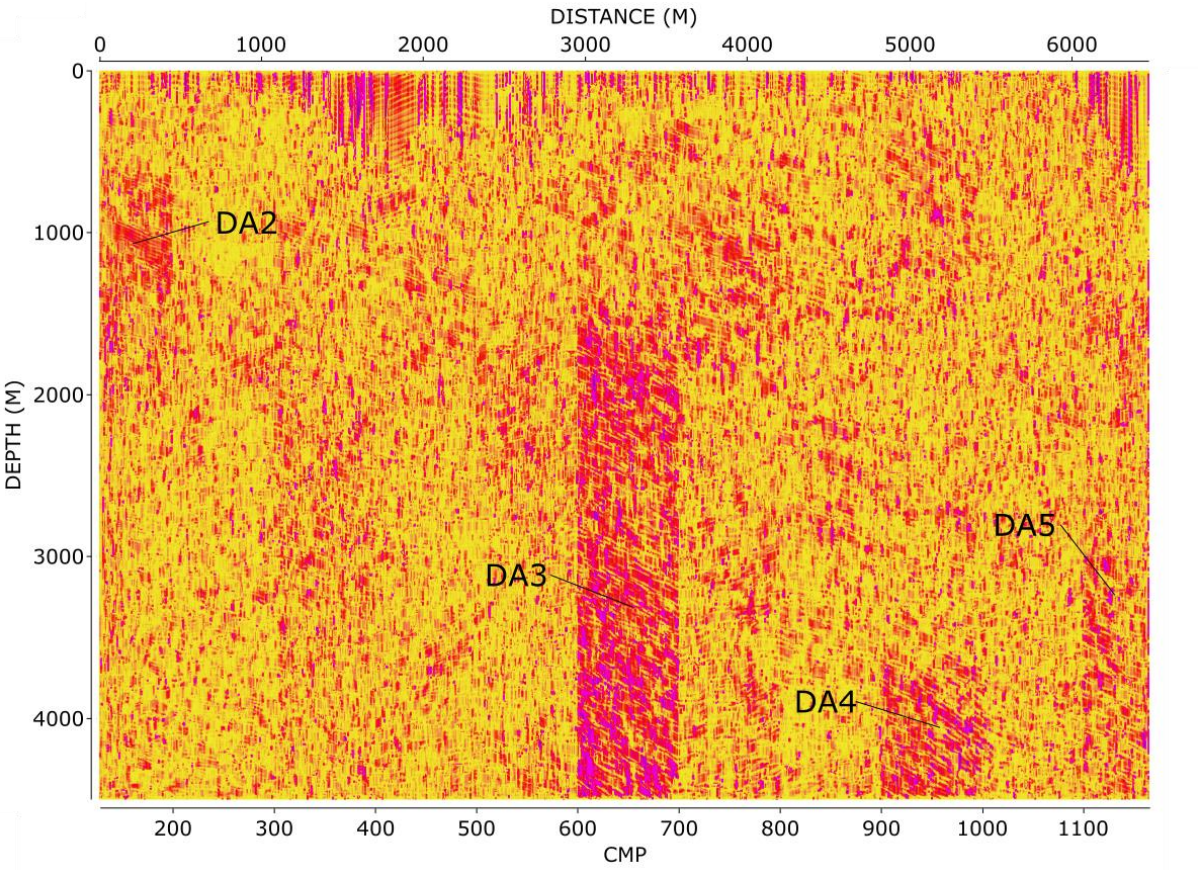

Figure 41- Profile V5 dip attribute section with dip anomalies labelled DA2 to DA5.

As with the dip attribute section of profile E1 (Figure 37), it is hard to say how reliable these results are. Some correlation can be seen with faulting yet again. In the dip attribute section, there is a number of anomalous dip attribute responses (labelled DA2 - DA5 in Figure 41). DA2 is seen at about CMP 150 at a depth of 1000 m, this could be resulting from fracturing of the shallow portion of the four-layer reflector package. DA3 is the major anomaly seen in the section and looking at the geological map in Figure 38 it is seems coincide with one of the off shooting faults of the Äkäsjoki Shear Zone, crossing the V5 survey profile at about CMP 600. The major Äkäsjoki fault crosses the V5 survey profile at about CMP 400, but interestingly no dip attribute response can be seen on the section. Also seen in the section is a smaller response, DA4, starting deep in the section at ~3600 m depth. This doesn't coincide with any faulting that is part of GTK's database (Figure 38), though this could be due to it being very deep in the section. At the end of the profile there is less pronounced response, DA5, that coincides with faulting seen on Figure 38 at CMP 1100.

7 Discussion

The use of legacy data for applying new and developing analysis techniques should be considered by companies. This study gives an example of the value that can be added to these datasets. Re-processing of the seismic reflection data from the Hannukainen area resulted in a seismic section with better definition, revealing reflectors deeper in the section that were not present in the previous interpretation.

The quality of the data collected is the main control on the quality of result attainable, and as such it can be said that the HIRE project was executed very well. The difference between the explosive data of profile E1 and the Vibroseis data of V5 is clearly seen, with the explosive data providing much cleaner results due to the source type and more linear survey geometry. Some problems were encountered in the Vibroseis data due to the more erratic survey geometry due to surface conditions that had to be worked around resulting in uncertain projection of the reflectors to the CMP line. These surface conditions contribute to the lower signal-to-noise ratio encountered in the data which in turn affects the processing procedure. Another major difference between explosive and Vibroseis data is the first-break picking, with the Vibroseis data proving much more time consuming and difficult. The correct phase is much more difficult to identify in the Vibroseis data resulting from the pounding action of the Vibroseis machine and the Vibroseis correlation operation. Picking the right phase that represents the first break is tedious and requires a lot of trial and error. Due to this, the resulting number of first break picks was reduced from that of the explosive data and the resulting static correction model is less reliable for the Vibroseis data. Another important step for producing the best seismic section possible was the identification and elimination of S-wave arrivals in the data. For both profiles the relative amplitude data was preserved as much as possible so that the resulting section could be confidently used for AVO and attribute analyses. This should be the case for all such studies as it is the only way to be confident in interpreting such analysis results, with the use of AGC being the main culprit in destroying the relative amplitude information. To combat this, a horizontal trace balancing filter was designed that suitably replaced the AGC.

The AVO analysis carried out with GLOBE Claritas is considered to be more of a ‘reconnaissance’ analysis method. For a full interpretation of the AVO analysis results, downhole measurements of geophysical properties would be needed. However, some interesting results were gained from the AVO analysis, with four AVO classes assigned to the

AVO1 and AVO2 horizons and AVO attributes such as AVO product and Poisson's ratio change calculated across these horizons. The AVO classes originated from the classification of AVO responses in marine gas sands and their encasing shale surroundings and are easily adapted to hard rock environments as they are based on signal behaviour. However, these signal behaviours have a significance in a hydrocarbon setting that cannot be adapted to hard rock environments. AVO quantities such as AVO product and Poisson's ratio change can be calculated from the resulting analysis and from these we can try to identify correlating patterns in the data that might suggest some anomalous physical properties. From this correlation, a range of CMPs was identified that seems to give a good correlation of different AVO anomaly types. This kind of study done with two horizons of ~100 CMPs was quite time consuming, so the choice of horizon is a critical step in the analysis. Identifying target horizons at drillable depths and with some amplitude strength variation across them was thought to be the most important choice for the analysis.

In the attribute analysis, in profile E1 especially, the seismic amplitude based attributes (Envelope, first derivative envelope, seismic impedance and Hilbert Transfer) imaged the layers of the reflector package well. The phase attribute was successful in showing the continuity of the reflectors. In combination with the seismic section and the amplitude-based seismic attributes, the data was interpreted as showing a four-layer reflector package as opposed to the three-layer reflector package interpreted by Kukkonen et al. (2009). The dip attribute showed anomalous areas where faulting or fracturing occurred, correlating with GTK's fault database, though it must be stated that this type of response to the dip attribute does not seem to be typical. However, the relation to mapped faulting is interesting.

The main product of this thesis is a quantitative analysis of seismic data. Looking how this analysis relates to the geological borehole data is crucial for understanding the significance of the results for mineral exploration in the area. The borehole coverage is not sufficient to do detailed interpretation, nor is there enough information on the local petrophysics available; and as such further studies are recommended to take place. Figures 42 and 43 shows a 3D view of the seismic section of profiles E1 and V5 using GoCAD software. The seismic sections projected in Figures 42 and 43 are the same as seen in Figure 18 for profile E1, and Figure 27 for profile V5. Projected with these is data from the 15 boreholes shown and labelled in Figure 12.

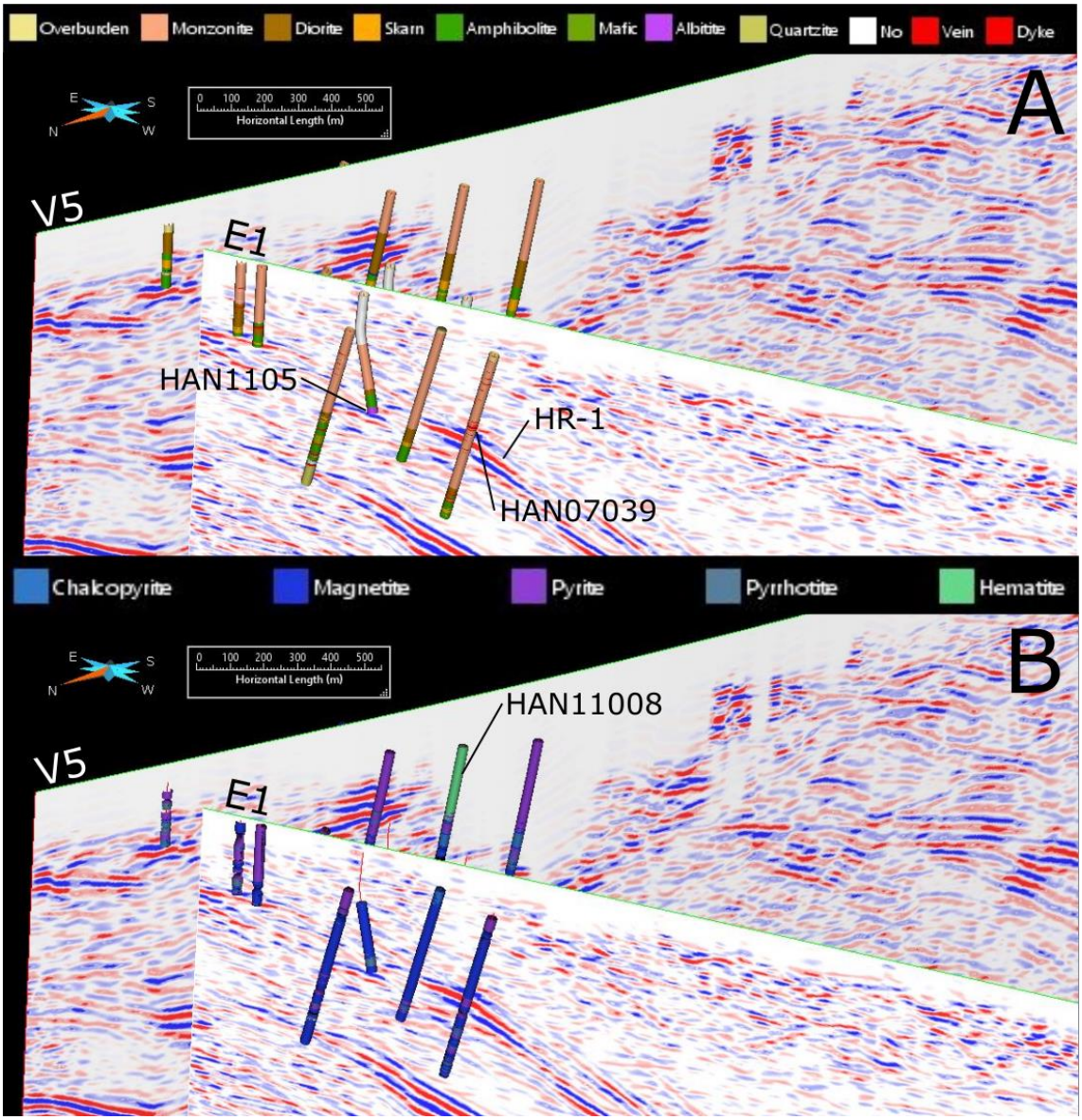

Figure 42 - 3D view of seismic profiles E1 and V5 with borehole data of A - main lithological unit and B - main mineral type.

Figure 42A shows the major lithological unit, here we see that in the unreflective portion of the section above the first reflector (HR-1 in Figures 18 and 27) the major lithology is monzonite and diorite, though diorite is seen within areas of reflection also. The perspective is a bit misleading here, but the possibility that some reflections are from between monzonite and diorite can't be excluded. Petrophysical data for monzonite is not available so this would be particularly important to see with the collection of more petrophysical data from the area. Reflections correlate with the appearance of amphibolite, skarn and mafic volcanics. Albitite (purple in Figure 42A) is seen at the bottom of borehole HAN11005 correlating with the top of the uppermost reflector of HR-1. Various instances of dykes and veins (red in Figure 42A) are seen throughout the boreholes, especially in borehole HAN07039, no real correlation can

be made to the seismic section for these. Figure 42B shows the main mineral type, here we see a long instance of hematite in borehole HAN11008 near profile V5, this is located in the uncertain reflector projection zone seen in Figure 27 so interpretation is impossible. Throughout the rest of the boreholes, magnetite is the abundant mineral with appearances of pyrite possibly corresponding to the reflective layers in profile E1 as it has such a higher density and seismic velocity in comparison to the host rocks (Figure 4).

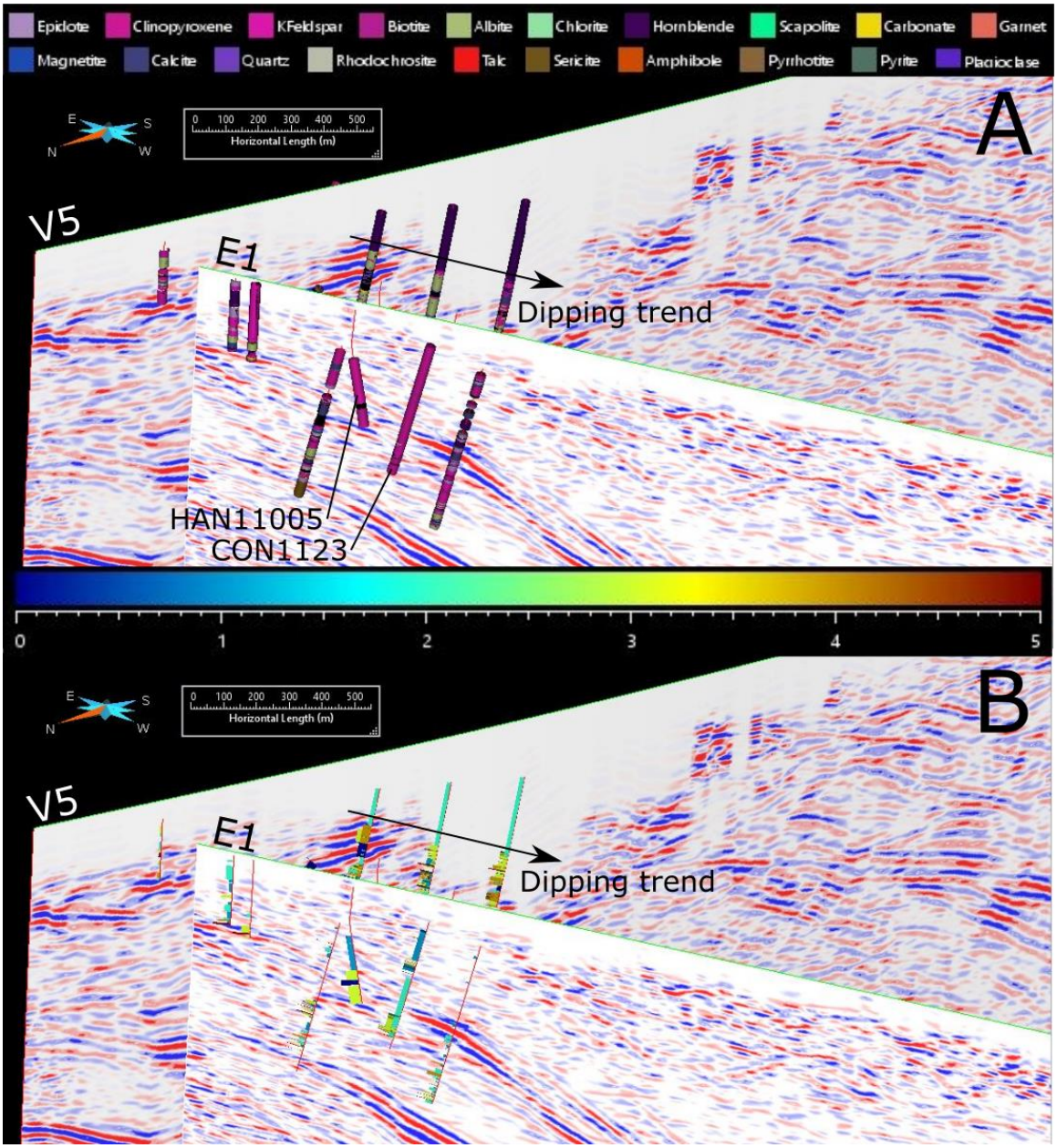

Figure 43 - 3D view of seismic profiles E1 and V5 with borehole data of A - alteration mineral type and B - alteration intensity.

Figure 43A shows the main alteration minerals, for profile V5, albite, K-feldspar and biotite are the main alteration minerals and show a dipping trend that that might be related to the

dipping reflector if it was not obscured by the reflector projection issue that was encountered due to the crooked geometry of profile V5. For profile E1 the dipping trend of alteration mineralisation is not as clear as it is in profile V5. Biotite is seen as the main alteration mineral for nearly the entire length of boreholes CON1123 and HAN11005, while albite is seen in the deeper parts of the other boreholes associated with profile E1. For the petrophysical values that are listed for the main rock types (Table 2), there is no way of knowing how altered or unaltered the rocks these values might represent are. However, the aim of including these figures is to talk about broad trends, and it appear that alteration would lower the acoustic impedance of the altered rock and could thus potentially be a cause of reflections. Conversely, mineralization generally increases that acoustic impedances, and if the deposits are massive enough, it could result in large enough acoustic impedance contrasts for reflections to be observed. Figure 43B shows the alteration intensity, rated on a scale of 0 (no alteration) to 5 (heavy alteration). A general trend of increased alteration intensity can be identified to possibly correlate with the upper reflective layer of profile V5, but this trend lies in the zone of uncertain reflector projection. A weaker trend can be seen for the boreholes associated with profile E1. This would support the theory of Junno et al. (2020) that a higher level of alteration can result in higher amplitudes in the seismic section. RQD borehole data, which shows the degree of fracturing within the rock, was also available but no correlation to the seismic data could be seen. An expanded RQD would be interesting to possibly compare with the dip attribute to investigate the unusual signature that were seen in Figures 37 and 41.

Further analysis of the cause of reflectivity in the area would yield valuable information. For this more borehole data is needed in the area, with targeted drilling and possible additional analysis of the core that has already been extracted. To achieve the same level of detail Junno et al. (2020) achieved with the forward modelling of mineralisation and alteration assemblages, the seismic P-wave velocity and density parameters are needed for each of the composite rock types and mineral types encountered at Hannukainen. This strengthening of petrophysical data could then be used for a large scale data mining analysis such as that of the SOM analysis also carried out by Junno et al. (2020).

To yield more detailed seismic data for the area a 3D seismic reflection survey could be undertaken. 3D seismic surveying has previously been used successfully for mine planning in Finland at the Kevitsa NI-Cu-PGE deposit (Malehmir et al., 2012). More drilling would help further AVO research, as synthetic gathers could be compiled and analysed for AVO

anomalies. In the AVO analysis an area of interest was found between CMPs 647 and 661 where consistent and strong negative AVO product is seen (Figure 33). This area shows Class I and Class IV AVO responses in Figure 30. Correlating with Figure 32 it is seen that this area also encounters some strong positive values for Poisson's ratio change. Targeted drilling of this area would be of interest to tie in geological and petrophysical data to these geophysical results. Drilling to a depth of ~1000 m is needed so as to penetrate both the AVO1 and AVO2 horizons.

8 Conclusions

The distinct southwest dipping reflector package at the Hannukainen mine site was imaged well by the re-processing of the HIRE project dataset. The use of seismic attribute analysis has resulted in increased knowledge of the amplitude content and continuity of the reflector package as a whole. The reflector package is interpreted to be a four-layer package as a result of the phase and weighted instantaneous frequency attributes. The dip attribute shows some unexpected vertical anomalies that in some cases correspond to mapped faulting. Furthermore, this work has shown that seismic AVO analysis can be adapted to a hard rock environment, and with further work could be developed into an industry standard procedure like it is in the hydrocarbon industry. The AVO analysis identified an area for suggested targeted drilling by correlating the results of AVO response classification with AVO product and Poisson's ratio change calculation. The processing workflow used in this study was designed as such to preserve the relative amplitude information of the seismic data. This workflow could be used as a template for further work in AVO and attribute analysis for the HIRE project data.

For future work in the area, a 3D seismic reflection survey would greatly increase the level of knowledge for the reflector package seen at Hannukainen and would greatly help in knowing the spatial location of the reflectors which is important for mine planning. With a 3D survey correctly positioned true relative amplitude data can be analysed. A complete set of petrophysical data for the rock and mineral types encountered in the area would also help to define the cause of reflectivity in the seismic data. Further utilization of the HIRE project dataset would also be of use for the wider area, adapting the analyses used in this study to the rest of the dataset could add considerable value to the data.

9 Acknowledgments

First and foremost, I would like to thank my supervisor Emilia Koivisto for the time and effort she invested in me throughout the course of completing this thesis. Thanks also to Ilmo Kukkonen, who had extensive previous experience with the dataset for giving his input. Jouko Pakarinen, Teemu Isometsä and all at Hannukainen Mining Oy for the willingness to work together and provide the seismic reflection and borehole data for this study. Software used in this study included GLOBE Claritas, GoCAD, ArcGIS and Reflexw. And finally, special thanks to my friends Christos, Letizia and Izzy for providing welcome distractions during times when they were needed.

10 References

AKI, K., & RICHARDS, P. G. (2002). Quantitative seismology.

ANSTEY, N. (1973). The significance of color displays in the direct detection of hydrocarbons: 43rd Annual International Meeting.

BALCH, A. H. (1971). Color sonagrams: A new dimension in seismic data interpretation. *Geophysics*, **36**(6), 1074-1098.

BARNES, A. E. (1991). Instantaneous frequency and amplitude at the envelope peak of a constant-phase wavelet. *Geophysics*, **56**(7), 1058-1060.

BARNES, A. E. (1992). The calculation of instantaneous frequency and instantaneous bandwidth. *Geophysics*, **57**(11), 1520-1524.

BELLEFLEUR, G., SCHETSELAAR, E., WHITE, D., MIAH, K., & DUECK, P. (2015). 3D seismic imaging of the Lalor volcanogenic massive sulphide deposit, Manitoba, Canada. *Geophysical Prospecting*, **63**(Hard Rock Seismic imaging), 813-832.

BODINE, J. H. (1984). Waveform analysis with seismic attributes. In *SEG Technical Program Expanded Abstracts 1984* (pp. 505-509). Society of Exploration Geophysicists.

BODINE, J. H. (1986). U.S. Patent No. 4,633,447. Washington, DC: U.S. Patent and Trademark Office.

BOHLEN, T., MÜLLER, C., MILKEREIT, B., EATON, D. W., & SALISBURY, M. H. (2003). Elastic seismic wave scattering from massive sulfide orebodies: on the role of composition and shape. *Hardrock seismic exploration: SEG 70*, 89.

CASTAGNA, J. P., & SWAN, H. W. (1997). Principles of AVO crossplotting. The Leading Edge, **16**(4), 337-344.

CASTAGNA, J. P., SWAN, H. W., & FOSTER, D. J. (1998). Framework for AVO gradient and intercept interpretation. *Geophysics*, **63**(3), 948-956.

CHOPRA, S., ALEXEEV, V., & XU, Y. (2003). 3D AVO crossplotting—An effective visualization technique. *The Leading Edge*, **22**(11), 1078-1089.

CHOPRA, S., & MARFURT, K. J. (2005). Seismic attributes—A historical perspective. *Geophysics*, **70**(5), 3SO-28SO.

CHOPRA, S., & MARFURT, K. J. (2007). Volumetric curvature attributes for fault/fracture characterization. *First Break*, **25**(7), 35-46.

COCKER, J., UROSEVIC, M., & EVANS, B. (1997). A high resolution seismic survey to assist in mine planning. In *Proceedings of Exploration* (Vol. 97, pp. 473-476).

CONTICINI, F. (1984) Seismic facies quantitative analysis: New tool in stratigraphic interpretation: 54th Annual International Meeting, SEG, session S18.3.

DOMENICO, S. N. (1976). Effect of brine-gas mixture on velocity in an unconsolidated sand reservoir. *Geophysics*, **41**(5), 882-894.

DRUMMOND, B. J., GOLEBY, B. R., OWEN, A. J., YEATES, A. N., SWAGER, C., ZHANG, Y., & JACKSON, J. K. (2000). Seismic reflection imaging of mineral systems: Three case histories. *Geophysics*, **65**(6), 1852-1861.

EATON, D. W., & WU, J. (1996). Relative-amplitude preserving processing for crustal seismic reflection data: an example from western Canada. *Tectonophysics*, **264**(1-4), 357-370.

ECKER, C., DVORKIN, J., & NUR, A. (1998). Sediments with gas hydrates: Internal structure from seismic AVO. *Geophysics*, **63**(5), 1659-1669.

EDFELT, Å., ARMSTRONG, R. N., SMITH, M., & MARTINSSON, O. (2005). Alteration paragenesis and mineral chemistry of the Tjårrojåkka apatite–iron and Cu (-Au) occurrences, Kiruna area, northern Sweden. *Mineralium Deposita*, **40**(4), 409-434.

ELBRA, T., KARLQVIST, R., LASSILA, I., HÆGGSTRÖM, E., & PESONEN, L. J. (2011). Laboratory measurements of the seismic velocities and other petrophysical properties of the Outokumpu deep drill core samples, eastern Finland. *Geophysical Journal International*, **184**(1), 405-415.

FATTI, J. L., SMITH, G. C., VAIL, P. J., STRAUSS, P. J., & LEVITT, P. R. (1994). Detection of gas in sandstone reservoirs using AVO analysis: A 3D seismic case history using the Geostack technique. *Geophysics*, **59**(9), 1362-1376.

FOSTER, D. J., SMITH, S. W., DEY-SARKAR, S., & SWAN, H. W. (1993). A closer look at hydrocarbon indicators. In *SEG Technical Program Expanded Abstracts 1993* (pp. 731-733). Society of Exploration Geophysicists.

FOSTER, D. J., KEYS, R. G., & LANE, F. D. (2010). Interpretation of AVO anomalies. *Geophysics*, **75**(5), 75A3-75A13.

GEERTSMA, J., & SMIT, D. C. (1961). Some aspects of elastic wave propagation in fluid-saturated porous solids. *Geophysics*, **26**(2), 169-181.

GERSZTENKORN, A., & MARFURT, K. J. (1999). Eigenstructure-based coherence computations as an aid to 3D structural and stratigraphic mapping. *Geophysics*, **64**(5), 1468-1479.

GIBSON, M. A., JOLLEY, S. J., & BARNICOAT, A. C. (2000). Interpretation of the Western Ultra Deep Levels 3-D seismic survey. *The Leading Edge*, **19**(7), 730-735.

GOLEBY, B. R., BLEWETT, R. S., KORSCH, R. J., CHAMPION, D. C., CASSIDY, K. F., JONES, L. E. A., GROENEWALD, P. B., & HENSON, P. (2004). Deep seismic reflection profiling in the Archaean northeastern Yilgarn Craton, Western Australia: implications for crustal architecture and mineral potential. *Tectonophysics*, **388**(1-4), 119-133.

GREGORY, A. R. (1976). Fluid saturation effects on dynamic elastic properties of sedimentary rocks. *Geophysics*, **41**(5), 895-921.

GYURKÓ, P., SZABADVÁRY, L., KARDEVÁN, P. AND ANTAL, A. (1983). Report on the geophysical test measurements carried out in the Rautuvaara area, over the Hannukainen ore deposits between June 27th and July 1st, 1983. Eötvös Loránd Geophysical Institute of Hungary, Report Aug 16, 1983, 15 p. (unpublished).

HAMMOND, A. L. (1974). Bright spot: better seismological indicators of gas and oil. *Science*, **185**(4150), 515-517.

HANSKI, E., HUHMA, H., & VAASJOKI, M. (2001). Geochronology of northern Finland: a summary and discussion. *Special Paper-Geological Survey of Finland*, 255-279.

HARRISON, C. B., & UROSEVIC, M. (2012). Seismic processing, inversion, and AVO for gold exploration—Case study from Western Australia. *Geophysics*, **77**(5), WC235-WC243.

HART, B. S., PEARSON, R., & RAWLING, G. C. (2002). 3D seismic horizon-based approaches to fracture-swarm sweet spot definition in tight-gas reservoirs. *The Leading Edge*, **21**(1), 28-35.

HATHERLY, P., POOLE, G., MASON, I., ZHOU, B., & BASSINGTHWAIGHTE, H. (1998). 3D seismic surveying for coal mine applications at Appin Colliery, NSW. *Exploration Geophysics*, **29**(4), 407-409.

HILTUNEN, A. (1980). Geological drill core report, hole R198, Hannukainen, Kivivuopio. Unpublished material of Rautaruukki Oy, Dept. of Exploration, 3 p. (obtained from archives of GTK).

HILTUNEN, A. (1982). The Precambrian geology and skarn iron ores of the Rautuvaara area, northern Finland.

HITZMAN, M. W., ORESKES, N., & EINAUDI, M. T. (1992). Geological characteristics and tectonic setting of proterozoic iron oxide (Cu-U-Au-REE) deposits. *Precambrian research*, **58**(1-4), 241-287.

HLOUŠEK, F., HELLWIG, O., & BUSKE, S. (2015). Three-dimensional focused seismic imaging for geothermal exploration in crystalline rock near Schneeberg, Germany. *Geophysical Prospecting*, **63**(Hard Rock Seismic imaging), 999-1014.

HOSSAIN, M. S., UROSEVIC, M., & WIJNS, C. (2015). Seismic volumetric interpretation of a disseminated copper system in Kevitsa, northern Finland. *ASEG Extended Abstracts*, **2015**(1), 1-4.

JINGBIN, C., ZHONGHONG, W., PING, C., QUANHU, L., & CHEN, X. (2016). The application of seismic attribute analysis technique in coal field exploration. *Interpretation*, **4**(1), SB13-SB21.

JUHLIN, C., ELMING, S. Å., MELLQVIST, C., ÖHLANDER, B., WEIHED, P., & WIKSTRÖM, A. (2002). Crustal reflectivity near the Archaean-Proterozoic boundary in northern Sweden and implications for the tectonic evolution of the area. *Geophysical Journal International*, **150**(1), 180-197.

JUNNO, N., KOIVISTO, E., KUKKONEN, I., MALEHMIR, A., WIJNS, C., & MONTONEN, M. (2020). Data mining of petrophysical and lithogeochemical borehole data to elucidate the origin of seismic reflectivity within the Kevitsa Ni–Cu–PGE bearing intrusion, northern Finland. *Geophysical Prospecting*, **68**(1), 82-102.

KATSUBE, T. J., & KAMINENI, D. C. (1983). Effect of alteration on pore structure of crystalline rocks; core samples from Atikokan, Ontario. *The Canadian Mineralogist*, **21**(4), 637-646.

KINNUNEN, A. (1980) Geologinen kairausseloste, Laurinoja, Reikä no.170. Rautaruukki Oy internal report, 5 pp. (in Finnish).

KOEFOED, O. (1955). On the effect of Poisson's ratios of rock strata on the reflection coefficients of plane waves. *Geophysical Prospecting*, **3**(4), 381-387.

KOIVISTO, E., MALEHMIR, A., HELLQVIST, N., VOIPIO, T., & WIJNS, C. (2015). Building a 3D model of lithological contacts and near-mine structures in the Kevitsa mining and exploration site, Northern Finland: constraints from 2D and 3D reflection seismic data. *Geophysical Prospecting*, **63**(Hard Rock Seismic imaging), 754-773.

KORJA, A., & HEIKKINEN, P. (2005). The accretionary Svecofennian orogen—insight from the BABEL profiles. *Precambrian Research*, **136**(3-4), 241-268.

KRÖNER, A., PUUSTINEN, K., & HICKMAN, M. (1981). Geochronology of an Archaean tonalitic gneiss dome in northern Finland and its relation with an unusual overlying volcanic conglomerate and komatiitic greenstone. *Contributions to Mineralogy and Petrology*, **76**(1), 33-41.

KUKKONEN, I., HEIKKINEN, P., HEINONEN, S. E., LAITINEN, J., & HIRE WORKING GROUP OF THE GEOLOGICAL SURVEY OF FINLAND (2009). HIRE Seismic Reflection Survey in the Hannukainen- Rautuvaara Fe-Cu-Au exploration area, Northern Finland. Report Q; Vol. 2009/23, No. 50.

LAWTON, D. C. (1989). Computation of refraction static corrections using first-break traveltime differences. *Geophysics*, **54**(10), 1289-1296.

LEHTONEN, M.I., AIRO, M. L., EILU, P., HANSKI, E., KORTELAINEN, V., LANNE, E., MANNINEN, T., RASTAS, P., RÄSÄNEN, J., VIRRANSALO, P. (1998) The stratigraphy, petrology and geochemistry of the Kittila¨ greenstone area, northern Finland. A Report of the Lapland Volcanite Project, Geological Survey of Finland, Report of Investigation, **140**, 144 pp. (in Finnish with summary in English).

LI, Y., DOWNTOWN, J., & GOODAWAY, B. (2003). Recent applications of AVO to carbonate reservoirs in the Western Canadian Sedimentary Basin. *The Leading Edge*, **22**(7), 670-674.

LOVE, P. L., & SIMAAN, M. (1984). Seismic signal character recognition using texture analysis techniques. In Proceedings of the IEEE International Conference on Acoustics, Speech and Signal Processing (pp. 48-12).

MALEHMIR, A., & BELLEFLEUR, G. (2009). 3D seismic reflection imaging of volcanic-hosted massive sulfide deposits: Insights from reprocessing Halfmile Lake data, New Brunswick, Canada. *Geophysics*, **74**(6), B209-B219.

MALEHMIR, A., SCHMELZBACH, C., BONGAJUM, E., BELLEFLEUR, G., JUHLIN, C., & TRYGGVASON, A. (2009). 3D constraints on a possible deep> 2.5 km massive sulphide mineralization from 2D crooked-line seismic reflection data in the Kristineberg mining area, northern Sweden. *Tectonophysics*, **479**(3-4), 223-240.

MALEHMIR, A., DURRHEIM, R., BELLEFLEUR, G., UROSEVIC, M., JUHLIN, C., WHITE, D. J., MILKEREIT, B., & CAMPBELL, G. (2012a). Seismic methods in mineral exploration and mine planning: A general overview of past and present case histories and a look into the future. *Geophysics*, ***77***(5), WC173-WC190.

MALEHMIR, A., JUHLIN, C., WIJNS, C., UROSEVIC, M., VALASTI, P., & KOIVISTO, E. (2012b). 3D reflection seismic imaging for open-pit mine planning and deep exploration in the Kevitsa Ni-Cu-PGE deposit, northern Finland. *Geophysics*, **77**(5), WC95-WC108.

MANZI, M. S., GIBSON, M. A., HEIN, K. A., KING, N., & DURRHEIM, R. J. (2012a). Application of 3D seismic techniques to evaluate ore resources in the West Wits Line goldfield and portions of the West Rand goldfield, South Africa. *Geophysics*, **77**(5), WC163-WC171.

MANZI, M. S., DURRHEIM, R. J., HEIN, K. A., & KING, N. (2012b). 3D edge detection seismic attributes used to map potential conduits for water and methane in deep gold mines in the Witwatersrand basin, South Africa. *Geophysics*, **77**(5), WC133-WC147.

MANZI, M. S. D., HEIN, K. A. A., DURRHEIM, R., & KING, N. (2013). Seismic attribute analysis to enhance detection of thin gold-bearing reefs: South Deep gold mine, Witwatersrand basin, South Africa. *Journal of Applied Geophysics*, **98**, 212-228.

MANZI, M. S., COOPER, G. R., MALEHMIR, A., & DURRHEIM, R. J. (2020). Improved structural interpretation of legacy 3D seismic data from Karee platinum mine (South Africa) through the application of novel seismic attributes. *Geophysical Prospecting*, **68**(1-Cost-Effective and Innovative Mineral Exploration Solutions), 145-163.

MARFURT, K. J., KIRLIN, R. L., FARMER, S. L., & BAHORICH, M. S. (1998). 3D seismic attributes using a semblance-based coherency algorithm. *Geophysics*, **63**(4), 1150-1165.

MARFURT, K. J., SUDHAKER, V., GERSZTENKORN, A., CRAWFORD, K. D., & NISSEN, S. E. (1999). Coherency calculations in the presence of structural dip. *Geophysics*, **64**(1), 104-111.

MAZZOTTI, A. (1991). AMPLITUDE, PHASE AND FREQUENCY VERSUS OFFSET APPLICATIONS 1. *Geophysical Prospecting*, **39**(7), 863-886.

MEJÍA-HERRERA, P., ROYER, J. J., CAUMON, G., & CHEILLETZ, A. (2015). Curvature attribute from surface-restoration as predictor variable in Kupferschiefer copper potentials. *Natural Resources Research*, **24**(3), 275-290.

MELLQVIST, C., ÖHLANDER, B., WEIHED, P., & SCHÖBERG, H. (2003). Some aspects on the subdivision of the Haparanda and Jörn intrusive suites in northern Sweden. *GFF*, **125**(2), 77-85.

MERILAINEN, K. (1976). The granulite complex and adjacent rocks in Lapland, northern Finland.

MICHUM JR, R. M. (1977). The Depositional Sequence as a Basic Unit for Stratigraphic Analysis, Seismic Stratigraphy applications to hydrocarbon exploration. *AAPG, Mem.*, **26**, 53-62.

MILKEREIT, B., BERRER, E. K., WATTS, A., ROBERTS, B., & GUBINS, A. G. (1997). Development of 3D seismic exploration technology for Ni-Cu deposits, Sudbury Basin. In *Proceedings of Exploration*, **97**, 439-448.

NEWMAN, P. (1973). Divergence effects in a layered earth. *Geophysics*, **38**(3), 481-488.

NIIRANEN, T. (2005). Iron Oxide-Copper-Gold Deposits in Finland: case studies from the Peräpohja schist belt and the Central Lapland greenstone belt. Academic dissertation. University of Helsinki.

NIIRANEN, T., POUTIAINEN, M., & MÄNTTÄRI, I. (2007). Geology, geochemistry, fluid inclusion characteristics, and U–Pb age studies on iron oxide–Cu–Au deposits in the Kolari region, northern Finland. *Ore Geology Reviews*, **30**(2), 75-105.

NIIRANEN, T., LAHTI, I., NYKÄNEN, V., & KARINEN, T. (2014). Central Lapland Greenstone Belt 3D modeling project final report. *Geological Survey of Finland, Report of Investigation*, **209**, 78.

PARTYKA, G., GRIDLEY, J., & LOPEZ, J. (1999). Interpretational applications of spectral decomposition in reservoir characterization. *The Leading Edge*, **18**(3), 353-360.

PEYTON, L., BOTTJER, R., & PARTYKA, G. (1998). Interpretation of incised valleys using new 3D seismic techniques: A case history using spectral decomposition and coherency. *The Leading Edge*, **17**(9), 1294-1298.

PICOU, C., & UTZMANN, R. (1962). LA "COUPE SISMIQUE VECTORIELLE"*: UN POINTÉ SEMI-AUTOMATIQUE. *Geophysical Prospecting*, **10**(4), 497-516.

PIETILÄ, R. AND HATTULA, A. (1982) An application of audio-frequency magnetotellurics and charge-potential method in skarn iron ore prospecting in the Rautuvaara area, northern Finland. Paper presented at the 44th Meeting of European Association of Exploration Geophysicists, Cannes, France, June 8-11, 1982, preprint, 9 p.

PUUSTINEN, K. (2003). Finnish mining industry and production of mineral raw materials in 1530-2001, historical review especially in light of production figures. Report M 10.1/2003/3. (In Finnish).

ROBERTS, A. (2001). Curvature attributes and their application to 3D interpreted horizons. *First Break*, **19**(2), 85-100.

ROBERTSON, J. D., & FISHER, D. A. (1988). Complex seismic trace attributes. *The Leading Edge*, **7**(6), 22-26.

ROSS, C. P., & KINMAN, D. L. (1995). Nonbright-spot AVO: Two examples. *Geophysics*, **60**(5), 1398-1408.

ROSS, C. P. (2000). Effective AVO crossplot modeling: A tutorial. *Geophysics*, **65**(3), 700-711.

RUMMERFIELD, B. F. (1954). Reflection quality, a fourth dimension. *Geophysics*, **19**(4), 684-694.

RUTHERFORD, S. R., & WILLIAMS, R. H. (1989). Amplitude-versus-offset variations in gas sands. *Geophysics*, **54**(6), 680-688.

SALISBURY, M. H., MILKEREIT, B., & BLEEKER, W. (1996). Seismic imaging of massive sulfide deposits; Part I, Rock properties. *Economic Geology*, **91**(5), 821-828.

SCHÖN, J. H. (2015). Physical properties of rocks: Fundamentals and principles of petrophysics. Elsevier.

SHEARER, P. M. (2019). Introduction to seismology. Cambridge university press.

SHERIFF, R. E. (1975). Factors affecting seismic amplitudes. *Geophysical prospecting*, **23**(1), 125-138.

SHERIFF, R. E. (1991). Encyclopaedic dictionary of exploration geophysics: SEG Geophysical References Series 1. Tulsa, USA, 384.

SHERIFF, R. E., & GELDART, L. P. (1995). Exploration seismology. Cambridge University Press.

SHIPLEY, T. H., HOUSTON, M. H., BUFFLER, R. T., SHAUB, F. J., MCMILLEN, K. J., LAOD, J. W., & WORZEL, J. L. (1979). Seismic evidence for widespread possible gas hydrate horizons on continental slopes and rises. *AAPG bulletin*, **63**(12), 2204-2213.

SHUEY, R. T. (1985). A simplification of the Zoeppritz equations. *Geophysics*, **50**(4), 609-614.

SMITH, G. C., & GIDLOW, P. M. (1987). Weighted stacking for rock property estimation and detection of gas. *Geophysical prospecting*, **35**(9), 993-1014.

SPRATT, S. (1987). Effect of normal moveout errors on amplitude versus offset-derived shear reflectivity. In *SEG Technical Program Expanded Abstracts 1987* (pp. 634-637). Society of Exploration Geophysicists.

STUART, G. W., JOLLEY, S. J., POLOME, L. G., & TUCKER, R. F. (2000). Application of 3D seismic attributes analysis to mine planning: Target gold deposit, South Africa. *The Leading Edge*, **19**(7), 736-742.

SWAN, H. W. (1991). Amplitude-versus-offset measurement errors in a finely layered medium. *Geophysics*, **56**(1), 41-49.

TANER, M. T., & SHERIFF, R. E. (1977). Application of amplitude, frequency, and other attributes to stratigraphic and hydrocarbon determination: Section 2. Application of seismic reflection configuration to stratigraphic interpretation. *AAPG Mem*. **26,** 301–327.

TANER, M. T., KOEHLER, F., & SHERIFF, R. E. (1979). Complex seismic trace analysis. *Geophysics*, **44**(6), 1041-1063.

TRICKETT, J. C. (2005). Three-dimensional reflection seismics: worth its weight in platinum. *Journal of the Southern African Institute of Mining and Metallurgy*, **105**(5), 357-363.

TUCHOLKE, B. E., BRYAN, G. M., & EWING, J. I. (1977). Gas-hydrate horizons detected in seismic-profiler data from the western North Atlantic. *AAPG bulletin*, **61**(5), 698-707.

UROSEVIC, M., BHAT, G., & GROCHAU, M. H. (2012). Targeting nickel sulfide deposits from 3D seismicreflection data at Kambalda, Australia. *Geophysics*, **77**(5), WC123-WC132.

VÄISÄNEN, M. (2002) Structural features in the Central Lapland greenstone belt, northern Finland. *Geological Survey of Finland Report* M21.42/2002/3, (pp, 20).

VERM, R., & HILTERMAN, F. (1995). Lithology color-coded seismic sections: The calibration of AVO crossplotting to rock properties. *The Leading Edge*, **14**(8), 847-853.

VÖLGYESI, L., & MOSER, M. (1982). The inner structure of the Earth. Period. *Polytech. Chem. Eng*, **26**, 155-204.

VOSSLER, D. A. (1988) Automatic whole section seismic reflection mapping: 58th Annual International Meeting, SEG, session S2.2.

WHITE, R. E. (1991). Properties of instantaneous seismic attributes. *The Leading Edge*, **10**(7), 26-32.

WHITE, D., BOERNER, D., WU, J., LUCAS, S., BERRER, E., HANNILA, J., & SOMERVILLE, R. (2000). Mineral exploration in the Thompson nickel belt, Manitoba, Canada, using seismic and controlled-source EM methods. *Geophysics*, **65**(6), 1871-1881.

WHITE, R. S. (1977). Seismic bright spots in the Gulf of Oman. *Earth and Planetary Science Letters*, **37**(1), 29-37.

WOOD, L. C., & TREITEL, S. (1975). Seismic signal processing. *Proceedings of the IEEE*, **63**(4), 649-661.

ZOEPPRITZ, K. (1919). On the reflection and propagation of seismic waves. *Gottinger Nachrichten*, **1**(5), 66-84.